

REPORT NO. XX/XXX

Investigation of YBCO bolometers  
for THz wave detection

ARVID HAMMAR

Department of Microtechnology and Nanoscience  
CHALMERS UNIVERSITY OF TECHNOLOGY  
Göteborg, Sweden 2011



## Abstract

The work presented in this master thesis is about the fabrication and characterization of bolometers based on thin films of  $\text{YBa}_2\text{Cu}_3\text{O}_{7-\delta}$  dedicated for detection of radiation in the THz-regime. A cleanroom process was developed to fabricate antenna-integrated bolometers on  $\text{Al}_2\text{O}_3$  substrates. This process is described in detail to enable reproduction of the results. The same devices were tested at room temperature and 77 K as both direct and heterodyne detectors for a broad frequency range, 100 GHz to 1.63 THz. As direct detectors, the bolometers combine a responsivity of 450 V/W and a noise level of 20  $\text{pW}/\text{Hz}^{1/2}$  at 77 K. At room temperature the corresponding numbers were 15 V/W and 450  $\text{W}/\text{Hz}^{1/2}$ , making the bolometers competitive to established room temperature detector technologies. These properties were combined with a relatively fast response time of 300 ps and 2 ns at 77 K and room temperature, respectively. As heterodyne detectors, the bolometers exhibited a conversion gain of -24 dB and -28 dB at 77 K and room temperature, respectively. As the title of the thesis indicates, focus has been on investigation rather than optimization of the devices. Hence, there is still much to be done to obtain the best possible performance.



# Contents

Abstract . . . . .	i
<b>1 Introduction</b>	<b>1</b>
1.1 THz detectors . . . . .	1
1.2 Scope and thesis outline . . . . .	3
<b>2 Theoretical background</b>	<b>5</b>
2.1 Bolometers . . . . .	5
2.1.1 Basic principle of operation . . . . .	5
2.1.2 Detection modes . . . . .	7
2.1.3 Noise . . . . .	12
2.2 Superconductivity . . . . .	13
2.2.1 Characteristics and theories for superconductors . . . . .	13
2.2.2 $\text{YBa}_2\text{Cu}_3\text{O}_{7-\delta}$ . . . . .	16
2.3 Quasi-optical coupling . . . . .	17
2.3.1 Planar antennas . . . . .	18
2.3.2 THz lenses . . . . .	20
<b>3 Design and processing</b>	<b>23</b>
3.1 Design . . . . .	23
3.2 Fabrication procedure and material choices . . . . .	24
3.2.1 YBCO film deposition . . . . .	24
3.2.2 Bolometer and antenna patterning . . . . .	26
3.2.3 Submicron bolometers using electron beam lithography . . . . .	29
<b>4 Measurements, results and analysis</b>	<b>31</b>
4.1 DC characteristics . . . . .	31
4.1.1 DC measurements . . . . .	31
4.1.2 Calculation of temperature profiles under DC bias . . . . .	35
4.2 Direct detection . . . . .	37
4.2.1 Responsivity . . . . .	38
4.3 Mixing . . . . .	43
4.3.1 Superconducting state . . . . .	44
4.3.2 Room temperature . . . . .	47
4.4 Noise . . . . .	48
4.4.1 Room temperature . . . . .	49
4.4.2 Superconducting state . . . . .	50
<b>5 Conclusions and future outlook</b>	<b>51</b>

<b>Acknowledgements</b>	<b>53</b>
<b>References</b>	<b>55</b>
<b>A Processing steps</b>	<b>59</b>
<b>B Processing recipes</b>	<b>63</b>
B.1 Recipes and tool settings . . . . .	63
B.1.1 Substrate cleaning prior to PLD . . . . .	63
B.1.2 CeO <sub>2</sub> sputtering . . . . .	63
B.1.3 YBCO deposition using PLD . . . . .	64
B.1.4 Image reversal photolithography, resist: AZ 5214E . . . . .	66
B.1.5 Positive photolithography, resist: AZ 1512HS . . . . .	66
B.1.6 Carbon mask deposition using PLD . . . . .	66
B.1.7 Ar ion milling . . . . .	67
B.1.8 Au evaporation . . . . .	67
<b>C Equipment lists</b>	<b>69</b>
<b>D Publications</b>	<b>71</b>



# Chapter 1

## Introduction

THz radiation is associated with a region in the electromagnetic spectrum, which is usually taken to be between 100 GHz and 10 THz, or, equivalently, 3 mm and 30  $\mu\text{m}$ . It is situated between the microwave and the optical regions, where commercial applications have existed for quite some time. In contrast to these, the THz region has been one of the least exploited frequency ranges [1] due to many technical difficulties, such as making powerful sources and sensitive receivers. The radiation itself is non-ionizing and can penetrate materials such as paper, cloth, wood etc., while its ability to propagate through water and metal is negligible. Gases like  $\text{CO}_2$  and water vapour, have absorption/emission lines in the THz range. Altogether, these properties make THz radiation suitable for a vast range of applications. For instance, THz imaging can be used for medical applications to detect cancer [2] or in security systems to discover weapons hidden under clothes [3]. However, most of the THz applications have so far been related to the field of radio astronomy where low power signals are detected. Large scientific radio astronomy projects such as the Herschel Space Observatory [4], the ALMA interferometer [5] and the SOFIA telescope [6] are all dedicated to observation of radiation in the THz regime. Systems like these have high demands on sensitive detectors with very low noise. Although the best instruments of today have a noise level in the order of a few quantum limits up to frequencies of 1 THz [1], they are still too bulky and expensive for most applications outside the field of radio astronomy. It is therefore important to have a strong technological development on new types of detectors that make a trade off between sensitivity, size and cost. A comparison between some existing technologies is made below.

### 1.1 THz detectors

There are several types of detectors, based on different technologies, working in the THz regime today. Some of the most prominent examples are superconducting hot electron bolometers (HEB), Schottky diodes, Golay cells, superconductor-insulator-superconductor (SIS) tunnel junctions, field effect transistors and semiconductor bolometers. A comparison between different technologies is made in section.

HEB and SIS detectors are almost always cooled using liquid helium. Using cryogenically cooled devices has the advantage of very small noise levels, even at high frequencies [7]. However, cooling to temperatures well below 50 K has practical drawbacks since the detector is normally placed inside a bulky cryocooler with high energy consumption. There is also an endless need for refilling of cooling liquid which continuously boils off inside a cryostat. This limits the life time of space born missions such as the Herschel Scape Observatory. Detectors with room temperature operation offer here an alternative to HEB and SIS detectors. Figure 1.1 illustrates the double sideband noise temperature (DSB)<sup>1</sup> for Schottky, HEB and SIS detectors in the THz regime. The noise equivalent powers (NEP)<sup>2</sup> for the same technologies, when used as direct detectors, are presented in table 1.1.

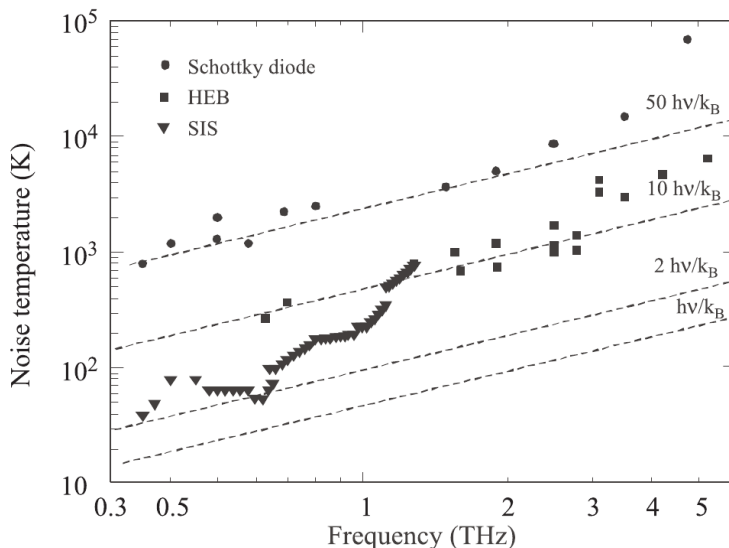


**Figure 1.1:** DSB noise temperature for Schottky, HEB and SIS detectors. Picture taken from [8].

The noise level in a detector is the most important figure of merit since it sets a lower limit for the detectable power. Some applications also have other requirements. For instance, a real time imaging system needs a detector that is fast enough to account for changes in the object being sampled. There are also practical aspects that have to be considered when making a THz detector. For instance, heterodyne mixing (described in section 2.1.2), which is widely used for THz frequencies, requires a local oscillator (LO) source and it is desirable to lower the need of LO power as much as possible. Schottky diode mixers require much LO power and have in this respect a disadvantage compared to HEB mixers.

HEB detectors have been made using different materials. Nb [10], NbN [7],

<sup>1</sup>The noise temperature is a figure of merit for heterodyne detectors which determines a low limit for the intensity of signals that can be detected.

<sup>2</sup>NEP is a measure of the smallest detectable power, defined in section 2.1.2

Detector type	Modulation frequency [Hz]	Operation frequency [THz]	NEP [W/Hz <sup>1/2</sup> ]	cooling needed
Golay cell	$\leq 20$	$\leq 30$	$10^{-9}$ - $10^{-10}$	no
Piezoelectric	$\leq 10^2$ (I)	$\leq 30$	$\approx (1 - 3) \cdot 10^{-9}$ (II)	no
Microbolometers	$\leq 10^2$	$\leq 30$	$10^{-10}$ (II)	no
Bi microbolometer	$\leq 10^6$	$\leq 3$	$1.6 \cdot 10^{-10}$ (II)	no
Nb microbolometer	-	$\leq 30$	$5 \cdot 10^{-11}$	no
Schottky diodes	$\leq 10^{10}$	$\leq 10$	$(5 - 20) \cdot 10^{-12}$ [9]	no
GaAs HEMT	$\leq 2 \cdot 10^{10}$	$\leq 30$	$10^{-10}$ (III)D	no
Si MOSFET	$3 \cdot 10^4$	0.645	$3 \cdot 10^{-10}$	no
Semiconductor HEB	$10^8$	$\approx 0.03 - 2$	$4 \cdot 10^{-10}$ (IV)	no
HEB	-	-	$< 10^{-15}$	yes
SIS	-	-	$\sim 10^{-15}$	yes

**Table 1.1:** Noise equivalent power (NEP) for different direct detection technologies. Data for uncooled detectors are taken from [8], unless otherwise stated.  
(I) Decreases with frequency and depends on dimensions  
(II) Decreases with frequency  
(III) Depends on gate length and gate voltage  
(IV) Depends on frequency

MgB<sub>2</sub> [11] are some examples which all require liquid helium for cooling. In this thesis, bolometers<sup>3</sup> based on the high temperature superconductor YB<sub>2</sub>Cu<sub>3</sub>O<sub>7- $\delta$</sub>  (YBCO) are investigated. This material only requires cooling to 80 - 90 K, which enables alternative cooling methods, such as liquid nitrogen or maybe Stirling cryocoolers [12]. Room temperature is also possible, although with degraded performance. LO power requirements can be smaller than for Schottky diode mixers. The noise levels will inevitably be higher than for liquid helium cooled detectors. Detection at room temperature is also possible, even though the performance is better at liquid nitrogen temperatures.

## 1.2 Scope and thesis outline

This thesis summarizes one year's work of developing bolometers based on YBCO. The goal was to develop a simple and reproducible cleanroom process and then to characterize the devices. Focus was on investigation rather than optimization. Hence, the same devices were tested for a large range of frequencies at both cryogenic and room temperatures.

Basic bolometer theory along with a brief discussion of superconductors is presented in chapter 2. The author's hope is that it should give a good overview

<sup>3</sup>The use of the word bolometer, instead of HEB, is consciously chosen here. To be classified as an HEB, the detector has to have a speed that is limited by the electron-phonon interaction time. Chapter 2 contain descriptions of device speed and the relation to interaction times.

of the subject without being too detailed. A discussion to the optical quasi-optical coupling technique is also found in chapter 2. Chapter 3 describes the cleanroom processing in such a way that the results should be possible to reproduce. Therefore, a quite detailed description is given. The experimental results are presented in chapter 4. It also provides details about how the measurements were performed and some predictions of possible future performance are also presented. Chapter 5 contains a summary of the work and a future outlook. The appendices contain information about used equipment, processing procedures/recipes and papers submitted to scientific journals.

## Chapter 2

# Theoretical background

### 2.1 Bolometers

The purpose of this section is to give some insight in the workings of a bolometer and what parameters are important for its performance. Basic thermal balance equations are considered and important characteristics of the bolometer are briefly derived and linked to the main parameters in these equations. The most important contributors of noise in a bolometer are also discussed. All contents of this section aim to describe bolometers based on high temperature superconducting YBCO films, but it should be general enough to be valid for other types of bolometers as well.

#### 2.1.1 Basic principle of operation

A bolometer is a thermic device that is used for measuring both frequency and amplitude of electromagnetic radiation. It consists of some material whose electric resistance is a function of temperature. The material can for instance be made of a thin superconducting film or some semiconducting material. Heat is produced in the bolometer when radiation is absorbed and due to this increase in temperature there will be a corresponding change of resistance. For a superconducting material this temperature dependence is strongest around the critical temperature where the material has its transition from normal to superconducting state (see section 2.2). The bolometer, which can be biased - both in constant current or constant voltage mode, depending on the circumstances - will exhibit voltage or current oscillations that can be exploited to obtain information about the incoming radiation.

What is special about an HEB is that the electrons in the bolometer are not in thermal equilibrium with the lattice, thereof the name *hot* electron bolometer. Ideally, only the electrons are heated. The heat of the electrons can be removed from the bolometer by different physical processes. One is interaction with phonons that escape to a substrate, on which the bolometer can be situated, that serves as a heat sink. Another cooling mechanism is diffusion where electrons are transported to the contact pads connecting the bolometer to external circuitry. The former kind of bolometer is said to be phonon-cooled

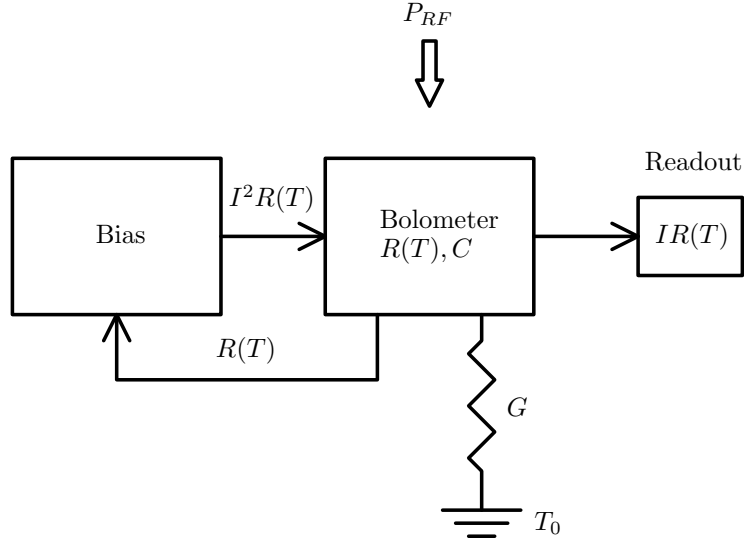


**Figure 2.1:** Bolometer thermally connected to a heat sink.  $P_{RF}$  denotes the incoming radiation,  $G$  the thermal conductance between the bolometer and the sink,  $C$  the bolometer's thermal capacitance,  $T$  the temperature of the bolometer and  $T_0$  the (constant) temperature of the heat sink. An electrical power of  $I^2 R(T)$  is coupled into the bolometer by a bias source. The readout on the right is the voltage swing given by  $IR(T)$ .

whereas the latter is called diffusion-cooled.

Schematically, a bolometer can be understood by considering figure 2.1. Using this simple picture one can directly write down a heat balance equation for the bolometer temperature  $T$ :

$$C \frac{dT}{dt} + G(T - T_0) = P(t), \quad (2.1)$$

where  $C$  is the thermal capacitance,  $t$  time,  $G$  the thermal conductance,  $T_0$  the substrate (heat-sink) temperature and  $P(t) = P_{RF} + I^2 R(T)$  the total power absorbed in the material. It is here assumed that heating in the bolometer is uniform and that  $T - T_0 \ll T$  and  $T - T_0 \ll T_0$ . The heat will have some non-uniform distribution in real bolometers, but this picture is still sufficient to give a basic idea of the bolometer's characteristics. Having the incoming power varying sinusoidally and assuming that the bolometer is fast enough to respond to this signal one can immediately write the solution to equation 2.1

$$T(\omega) = \text{Re} \left[ \frac{\frac{P(\omega)}{G} + T}{1 + j\frac{\omega C}{G}} \right] = \frac{\frac{P(\omega)}{G} + T}{1 + \left(\frac{C}{G}\right)^2 \omega^2} = \frac{\frac{P(\omega)}{G} + T}{1 + (\tau\omega)^2} \quad (2.2)$$

From this equation it is clear that the temperature in the bolometer scales linearly with both power (e.g. optical or electrical) and substrate temperature. The quantity  $\tau \equiv \frac{C}{G}$  is called the response time (discussed in section 2.1.2) and it determines how fast the bolometer can cool after being heated.

An important physical quantity used to characterize a bolometer is the temperature coefficient of resistance,  $\alpha$  defined by

$$\alpha \equiv \frac{1}{R} \left. \frac{dR}{dT} \right|_{T=T_0}. \quad (2.3)$$

It directly determines important figures of merit such as responsivity (described in section 2.1.2).

### 2.1.2 Detection modes

A bolometer has two different way of detecting radiation: direct (incoherent) detection and heterodyne (coherent) detection. In the former, RF radiation is the only input signal. Spectral resolution is determined by the input circuitry. The bolometer mainly responds to the power of the radiation. The input signal is usually amplitude modulated and the output voltage measured using a lock-in amplifier.

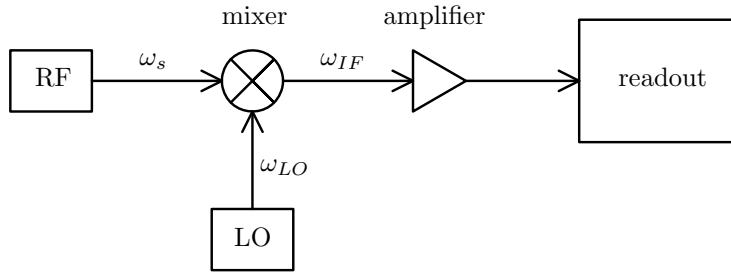


**Figure 2.2:** Figure showing the heterodyne detection mode with the signal frequency  $\omega_s$ , the LO frequency  $\omega_{LO}$  and the intermediate frequency  $\omega_{IF}$ . The direct detection mode is similar to this setup, but only the signal source is used. The readout is usually done with a spectrum analyzer (heterodyne detection) or a lock-in amplifier (direct detection).

When operating in the heterodyne detection mode the RF signal is mixed with a much stronger second source of known frequency, called local oscillator (LO). This is the origin of the name mixer. Usage of this detection mode brings about information of both frequency and power of the radiation.

#### Direct detection

There are different figures of merits to describe a bolometer's performance operating in the direct detection mode. The most important are the responsivity ( $S_V$ ), the noise equivalent power (NEP) and the response time ( $\tau$ ). Responsivity and response time will be treated in this section and noise equivalent power will be discussed in section 2.1.3.

The responsivity of a bolometer is here defined as the voltage response due to the absorbed power in the device and it has the dimension of voltage

per units of power. It is vital in many instances to have a high responsivity, e.g. when used as a direct detector the responsivity of the bolometer will have influence on the sensitivity, i.e. the ability to detect low power signals.

In order to understand what parameters will have influence on the bolometer responsivity a more thorough analysis of equation 2.1 is necessary. First, the power incident on the bolometer can be written as [13]

$$P = P(t) = P_0 + P_1 e^{i\omega t} \quad (2.4)$$

and the corresponding temperature will then be

$$T = T(t) = T_0 + T_1 e^{i\omega t}. \quad (2.5)$$

During operation the bolometer is biased with a constant current which together with the time-varying incident power creates ohmic heating,

$$I^2 R(T) = I^2 \left[ R(T_0) + \left. \frac{dR}{dT} \right|_{T=T_0} T_1 e^{j\omega t} \right] = I^2 R(T_0) [1 + T_1 \alpha e^{j\omega t}]. \quad (2.6)$$

Power is transferred to the bolometer via the heat sink at a rate determined by the thermal conductance  $G$  giving the term

$$P_{\text{heat sink}} = G(T - T_0) + \left. \frac{dP}{dT} \right|_{T=T_0} T_1 e^{i\omega t} = G(T - T_0) + G_{\text{dyn}} T_1 e^{i\omega t}, \quad (2.7)$$

where  $G_{\text{dyn}} \equiv \left. \frac{dP}{dT} \right|_{T=T_0}$  is the dynamic thermal conductance. The terms in 2.7 are based on Fourier's law, which states that the local heat flux is proportional to the local temperature gradient. It is assumed here that  $T - T_0 \ll T, T_0$  and therefore the first order expansion is valid. It should also be noted that  $G$  in general is a function of the temperature [13] but it is here assumed to be constant for small changes in temperature. Combining equations 2.1, 2.4, 2.5, 2.6, 2.7, demanding that power (i.e. energy) is conserved and equating time dependent and time independent terms separately yields

$$P_0 + I^2 R(T_0) = G(T - T_0). \quad (2.8)$$

$$P_1 + I^2 R(T_0) T_1 \alpha = i\omega C T_1 + G_{\text{dyn}} T_1. \quad (2.9)$$

As stated above, the responsivity is defined to be the change in voltage due to incoming radiation and it can therefore be written as

$$S_V = V_1 / P_1 = IR(T_0) \alpha T_1 / P_1. \quad (2.10)$$

Together with equation 2.9 this can be written as

$$S_V = \frac{IR(T_0) \alpha}{G_{\text{dyn}} - I^2 R(T_0) \alpha + i\omega C}. \quad (2.11)$$

Introducing an effective thermal conductance

$$G_e = G_{\text{dyn}} - I^2 R(T_0) \alpha, \quad (2.12)$$

a corresponding time constant  $\tau = C/G_e$ , described in section 2.1.2, and taking the real part of equation 2.11 gives

$$S_V = \frac{IR(T_0)\alpha}{G_e(1 + \omega^2\tau^2)} = \frac{IR\alpha}{G_e(1 + \omega^2\tau^2)}, \quad (2.13)$$

where  $R(T_0)$  is written as  $R$  for convenience. Analyzing equation 2.13 can give the impression that an arbitrary large responsivity can be reached by applying a very large bias current  $I$ . One argument to why this is not true is that  $\alpha$  can be strongly dependent of temperature and hence decrease at some current level. This is the actual case for a superconducting bolometer operating at temperatures around the critical temperature where the material has a very sharp resistance versus temperature behavior at the critical temperature  $T_c$  (see section 2.2). Another way to understand the limitation in responsivity is to first consider the case when  $G_{\text{dyn}} \gg I^2R$  which implies that  $G_e \simeq G_{\text{dyn}}$ . If, however,  $I^2R$  becomes comparable, or even equal to  $G_{\text{dyn}}$ , the responsivity will actually grow rapidly, see equations 2.12 and 2.13, but so will also the temperature. Hence, the bolometer will become overheated and the device will inevitably deteriorate and be destroyed.

### Response time

The response time  $\tau$  determines the speed of the detector, i.e. the ability to respond to sudden changes in the incoming RF power. As mentioned earlier, the input signal is usually amplitude modulated. The reason for doing this is that the system becomes less sensitive to noise and small signal variations can therefore be read out. The power can be modulated in different ways. The most common are: an electronically modulated (pulsed) source; a mechanical chopper; or to create "beats" in the RF signal by mixing two signals (discussed below). It is important in many applications to have a device that can provide a large readout bandwidth and it is therefore preferable to have a small  $\tau$ . At the same time it is also desirable to have a high responsivity. The latter can be achieved by reducing  $G_e$ , see equation 2.13. In the case of an HEB, this has been done by forming an air bridge instead of having the bolometer directly on a substrate. However, since  $\tau$  is inversely proportional to  $G_e$  this will make the bolometer slower. Another approach to the problem, which is used in this work, is to reduce the size of the bolometer, which increases  $S_V$  but keeps  $\tau$  constant. To see why this is true one can consider the following expressions for the thermal capacitance and thermal conductance [14]:

$$C = V\rho c_{\text{vol}} = Ad\rho c_{\text{vol}}, \quad (2.14a)$$

and

$$G_e = \frac{A}{R_{\text{bd}}}, \quad (2.14b)$$

where  $V$  is the bolometer volume,  $\rho$  the mass density,  $c_{\text{vol}}$  the volumetric heat capacitance,  $A$  the bolometer area,  $d$  its thickness and  $R_{\text{bd}}$  the thermal boundary resistance. Plugging in equations 2.14a and 2.14b into the expression for the response time yields

$$\tau = \frac{Ad\rho c_{\text{vol}}}{\frac{A}{R_{\text{bd}}}} = d\rho c_{\text{vol}}R_{\text{bd}} \quad (2.15)$$

Since  $C$  is not included in the expression for  $S_V$  and  $S_V \propto G_e^{-1}$  it is clear that a reduction of the bolometer area will indeed increase the responsivity. Hence, bolometers are usually made small.

The cooling of a bolometer is associated with interaction times for different physical processes. As mentioned above, two important cooling mechanisms for a bolometer are phonon cooling and diffusion cooling with interaction times  $\tau_{ph}$  and  $\tau_{diff}$ , respectively. The two interaction times add up inversely to form the total response time of the bolometer:

$$\tau = (\tau_{ph}^{-1} + \tau_{diff}^{-1})^{-1} \quad (2.16)$$

Figure 2.3 illustrates the different interaction times associated with the cooling of a bolometer.

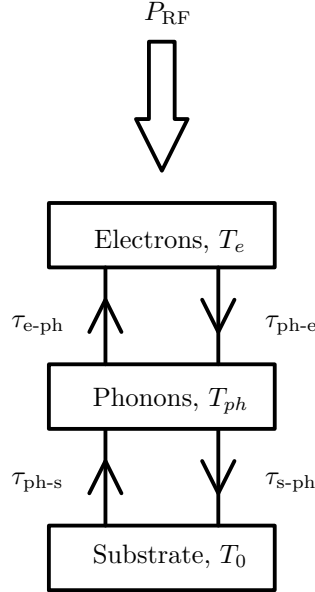


**Figure 2.3:** Illustration of the electron temperature  $T_e$ , phonon temperature  $T_{ph}$ , substrate temperature  $T_0$  and the corresponding interaction times.  $P_{RF}$  denotes the RF power incident on the bolometer.

When radiation is absorbed in a bolometer, phonons first interact with the electrons which have a corresponding temperature  $T_e$ . Energy is then transferred to the phonon subsystem at temperature  $T_{ph}$  at a rate associated with the interaction time  $\tau_{ph-e}$ . Some backscattering into the electron subsystem can also occur with the associated interaction time  $\tau_{e-ph}$ . Energy is then transferred analogously between the phonon subsystem and the substrate via phonons, with interaction times  $\tau_{s-ph}$  and  $\tau_{ph-s}$ . The values of these parameters will determine the total response time. The process where energy is removed from the bolometer via diffusion of electrons to the antenna contact pads is not shown in figure 2.3.

### Heterodyne mixing

When using the heterodyne mixing mode, two input signals produce a signal of an intermediate frequency  $\omega_{IF} = |\omega_{LO} - \omega_{RF}|$ . To see how this is done two sinusoidal signals,  $V_{RF} \propto \cos \omega_{RF}t$  and  $V_{LO} \propto \cos \omega_{LO}t$ , are added. Using that  $P \propto V^2$ , where  $P$  is the total power dissipated in the bolometer whereas  $V$  is the corresponding voltage, one obtains the following expression for a bolometer with linear current versus voltage characteristics:

$$P(t) \propto (\cos \omega_{LO}t + \cos \omega_{RF}t)^2. \quad (2.17)$$

Expanding the right hand side and using elementary trigonometric relations it is easy to show that the expression will consist of terms having frequencies  $2\omega_{LO}$ ,  $2\omega_{RF}$ ,  $\omega_{LO} + \omega_{RF}$  and  $\omega_{LO} - \omega_{RF}$ . The speed of the device is limited and it will only be able to respond to the power variations of frequency  $\omega_{IF}$ . Hence,

$$P(t) \propto \cos \omega_{IF}t. \quad (2.18)$$

When the bolometer is operating in a regime where the current is not a linear function of voltage, there will be higher order harmonics. To see this, one can expand the current in a Taylor series,

$$I = \sum_{n=1}^{\infty} \gamma_n V^n, \quad (2.19)$$

and plug in the two voltages given by  $V_{RF} \cos \omega_{RF}$  and  $V_{LO} \cos \omega_{LO}$ . It can then be showed that the remaining power can be expressed as

$$P(t) \propto \sum_{n=1}^{\infty} (\beta_n \cos n\omega_{RF}t + \beta'_n \cos n\omega_{LO}t)^2. \quad (2.20)$$

When expanding the terms on the right hand side of this equation it is clear that the only frequencies that will exist are  $m\omega_{IF}$  and  $k(\omega_{RF} + \omega_{LO})$ ,  $m$  and  $k$  being integers. However, these high order harmonics will be small compared to the  $\omega_{IF}$  term stemming from the fact that the term having coefficient  $\gamma_1$  will dominate in equation 2.19.

When considering equation 2.18 it is clear that the bolometer is insufficient to distinguish between  $\omega_{LO} + \omega_{IF}$  and  $\omega_{LO} - \omega_{IF}$ . This means that a signal  $\omega_S$  can be produced by two different RF signals:

$$\omega_S = \omega_{LO} \pm \omega_{IF} \quad (2.21)$$

Practically, this means that the IF signal with frequency  $\omega_{LO} + \omega_{IF}$  has a mirror image at frequency  $\omega_{LO} - \omega_{IF}$ . Mixers can be divided into two groups: those sensitive to both sidebands (i.e. both  $\omega_{LO} \pm \omega_{IF}$ ) and those which are not. These are referred to as double sideband (DSB) and single sideband (SSB) mixers, respectively.

A very important figure of merit for a mixer is the conversion gain, sometimes simply called gain. It relates the readout signal  $P_{IF}$  at frequency  $\omega_{IF}$  to the signal power  $P_S$ :

$$g = \frac{P_{IF}}{P_S} \quad (2.22)$$

$P_{\text{IF}}$  is usually straightforward to measure.  $P_{\text{S}}$  usually requires corrections for optical losses etc. One can also choose different power references for  $P_{\text{S}}$ , e.g. power absorbed in the bolometer, power measured prior to optical focusing elements etc. Despite what the name suggests, the gain is actually a loss in most cases. An analytical expression for the conversion gain is given by [15]

$$g = \frac{2I^2 C_0^2 P_{\text{LO}} R_L}{(R_L + R_0)^2} \left( 1 - I^2 C_0 \frac{R_L - R_0}{R_L + R_0} \right)^{-2}, \quad (2.23)$$

where  $C_0 = \frac{1}{G} \frac{\partial R}{\partial T}$ ,  $R_L$  the IF load impedance and  $R_0$  the bolometer DC resistance.

The gain bandwidth is another important figure of merit for a mixer. It is defined as the frequency where the conversion gain has dropped by a factor of 2 ( $\approx 3$  dB). The corresponding frequency is denoted by  $\omega_{3\text{dB}}$ . One can see the gain bandwidth as a measure of the speed of the bolometer, i.e. the ability to cool fast after being heated. Qualitatively, the gain bandwidth can be described by the following equation, which is intimately related to equation 2.13,

$$g(\omega_{\text{IF}}) = \frac{g(0)}{1 + \omega_{\text{IF}}^2 \tau^2}, \quad (2.24)$$

where  $g(0)$  is the conversion gain at  $\omega_{\text{IF}} = 0$ .

### 2.1.3 Noise

Any detector will inevitably be subject to unwanted signal distortions referred to as noise. A useful way to describe noise in a system is noise-equivalent power (NEP), defined as the signal power required to give a signal to noise ratio of 1 with bandwidth 1 Hz. This section will describe the most important sources of noise for a bolometer when operating as a direct detector. Low noise sources, such as photon noise, are omitted here since the low noise limits set by fundamental laws of physics are not among the main contributors of noise for YBCO bolometers. The noise stemming from measurement equipment will be treated in section 4.4.

#### Johnson noise

Ohmic losses will be present in a bolometer since it is resistive. It is here convenient to replace the resistive bolometer with an equivalent circuit (see reference [13]), consisting of a noise generator in series with a noise-free resistor  $R$ , with a RMS for voltage fluctuations of [16]

$$V_N = \sqrt{4k_B T R B}, \quad (2.25)$$

where  $k_B$  is Boltzmann's constant and  $B$  the bandwidth. From equation 2.10 it is clear that the signal voltage  $V_S = S_V P_S$ . Putting  $B = 1$  Hz and combining equation 2.25 and 2.10 gives

$$(\text{NEP})_J^2 = \frac{4k_B T R}{|S_V|^2} \quad (2.26)$$

### Thermal fluctuation noise

Random fluctuations of the temperature in the bolometer or simply thermal instability causes extra noise that is described by [13]

$$(\text{NEP})_T^2 = 4kT^2G. \quad (2.27)$$

This noise comes about due to energy quanta (phonons) that are randomly exchanges between the bolometer and the heat sink.

### Flicker noise

At low frequencies the so called flicker noise may become important. Because of its frequency behavior it is also called  $1/f$  noise. It is seen in many electronic devices and can be caused by several different physical processes such as impurity diffusion [17], but its origin is not well known.

### Overall noise

Due to the statistical independence of the noise sources, the total NEP adds up according to

$$(\text{NEP})_{tot}^2 = (\text{NEP})_J^2 + (\text{NEP})_T^2 + (\text{NEP})_F^2 + (\text{NEP})_A^2, \quad (2.28)$$

where the last term is due to noise in the amplifier circuitry that is always used in a bolometer detection system.

## 2.2 Superconductivity

This section will cover some basics of superconductivity with extra focus on the parts that are relevant to this work. The purpose is to explain which parameters of superconductivity are important when a superconducting bolometer is developed. Extra attention is paid to the high temperature superconductor YBCO.

### 2.2.1 Characteristics and theories for superconductors

As one might guess from the name, superconductivity deals with the conduction of electric current with a superior conductivity. In fact, the resistance of a material in the superconducting state is identically equal to zero. A superconducting state appears in some materials, when cooled below a certain temperature, referred to as the critical temperature  $T_c$ . The critical temperature is one of the most important parameters for a superconducting material. The rightmost plot of figure 2.4 illustrates a typical resistance versus temperature behavior for a superconductor. The sharp transition into the superconducting state is the main motivation to use superconducting materials for bolometers. When operating around  $T_c$ , the bolometer will have a very high  $\alpha$ , and consequently the highest sensitivity to temperature variations.

That the electric resistance decreases when the temperature is reduced is a common property of all metals, e.g. gold and aluminium. However, gold

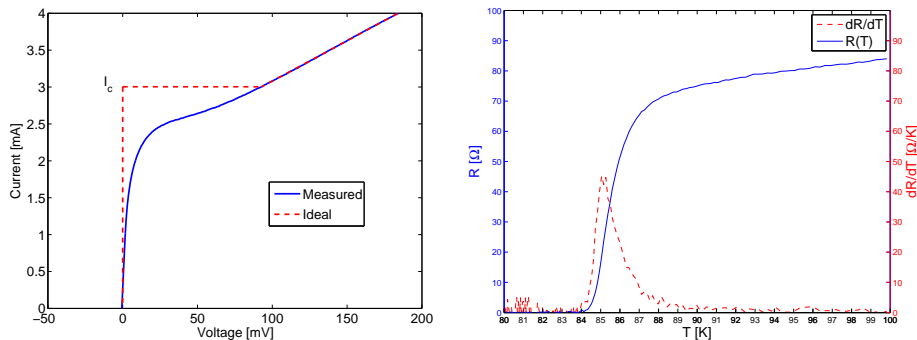


**Figure 2.4:** (left) Plot illustrating the critical current  $I_c$  for a measured superconducting bridge (with cable resistance etc. present) and an ideal curve where all resistance is absent. (right) Plot showing an example of a resistance versus temperature behavior for a superconductor with its derivative plotted as a dashed red curve. The temperature corresponding to the maximum of  $\frac{dR}{dT}$  is  $T_c$ .

has never displayed superconductivity when being cooled whereas aluminium becomes superconducting at 1.2 K [18]. The reason why some metals become superconducting at low temperatures and some do not remains unknown.

Another hallmark of superconductivity is perfect diamagnetism, meaning that sufficiently small external magnetic fields will be expelled from the interior of a superconductor. This phenomenon is known as the Meissner effect, which also implies that a superconducting state can only exist provided that all external magnetic fields are below a critical value  $H_c$  [18]. Figure 2.5 shows the requirements on temperature and external magnetic fields that have to be fulfilled to achieve superconductivity. The magnetic field impinging on the superconductor will decay according to London's equations, which are a set of phenomenological equations describing superconductors. One of London's equations, combined with Maxwell's equation  $\nabla \times \mathbf{h} = 4\pi\mathbf{J}/c$ , can be written as [18]

$$\nabla^2 \mathbf{h} = \frac{\mathbf{h}}{\lambda^2}, \quad (2.29)$$

where  $\lambda$  is known as the penetration depth. The penetration depth, which is temperature dependent, is one of the key parameters to characterize a superconductor.

Even though London's equations describe how superconductors behave, it says very little about what is happening on a microscopic level. Here the theory by Bardeen, Cooper, and Schrieffer from 1957 [19], BCS theory in short, offers a concept that explains the behavior of the electrons forming a supercurrent. The main idea of this theory is that the electrons interact pairwise, forming so called Cooper pairs in a boson-like state, and thereby obeying Bose-Einstein statistics. Pairing of electrons is made possible via a so called second order electron-phonon interaction in the material. One way to qualitatively understand how this interaction comes about is to first consider a system with a negatively

charged electron polarizing the material by attracting positively charged ions. Provided that this effect is strong enough, it can overcome the repulsive force between electrons and thereby creating a bound state of two electrons.

One important prediction of BCS theory is that there is a distinct energy  $E_g$  needed to break a Cooper pair, known as the depairing energy. It is given by [18]

$$E_g(T = 0 \text{ K}) = 3.52k_B T_c. \quad (2.30)$$

For a given  $T$  in the superconducting state this imposes a low frequency limit for the radiation that can be absorbed. However, a biased bolometer operating in a resistive state have a reduced energy gap which enables absorption of photons with less energy. There is no sharp upper energy limit of the photons that can be absorbed which therefore implies that superconducting devices are inherently broadband.

There are different ways to break the Cooper pairs and turning the superconductor into a normal state. As seen above, this will happen when an applied magnetic field become strong enough. It can also be done by applying a DC current. The current associated with the transition into the normal state is called critical current, denoted  $I_c$ . The current versus voltage characteristics are shown in figure 2.4.

Another, more phenomenological, theory of superconductivity was proposed by Ginzburg and Landau in 1950. This theory describes superconductivity using a pseudowavefunction  $\Psi$  that satisfies a non-linear version of the Schrödinger equation [18]. The local density of superconducting electrons  $n_s$  is given by  $n_s = |\Psi|^2$ . This theory is capable of explaining both the spatial variation of  $n_s$  and how  $n_s$  is influenced by external fields. A characteristic for each superconductor  $\xi$ , called the coherence length, is introduced in the Ginzburg-Landau theory that can be interpreted as the physical size of a Cooper pair, or more precisely the distance that  $\Psi$  can vary without changing its energy.  $\xi$  can together with  $\lambda$  be used to define one more parameter called the Ginzburg Landau parameter

$$\kappa = \frac{\lambda}{\xi} \quad (2.31)$$

It has been shown that this parameter can be used to characterize two distinct types of superconductors, namely type I and type II superconductors. More precisely,  $0 < \kappa < 1/\sqrt{2}$  gives a type I superconductor whereas type II has  $\kappa > 1/\sqrt{2}$ . The main difference between the two superconductor types is that type I has a distinct transition into the superconducting state when being cooled while type II has gradual transition involving a mixed state. Having a mixed state means that there are different regions in the material, some superconducting and others not. This is clearly seen when the magnetic field penetration is plotted versus applied external magnetic field, see figure 2.5. The sharper transition in type I superconductors can be explained with a longer coherence length that enables more electrons to interact [18].

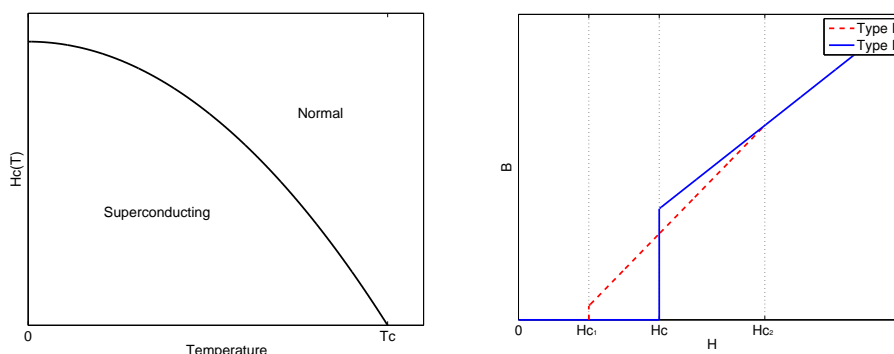


**Figure 2.5:** (left) Plot showing the superconducting region, encapsulated by the function for the critical magnetic field  $H_c(T) \approx H_c(0)[1 - (T/T_c)^2]$  [18]. (right) Plot showing a comparison between type I and type II superconductors. Magnetic field penetration is plotted versus an applied external magnetic field [18]. For type II superconductors there are two critical fields  $H_{C1}$  and  $H_{C2}$  with a mixed state sandwiched in between.

## 2.2.2 $\text{YBa}_2\text{Cu}_3\text{O}_{7-\delta}$

$\text{YBa}_2\text{Cu}_3\text{O}_{7-\delta}$  (YBCO) was discovered in 1987 and is classified as a high temperature type II superconductor with a critical temperature of 93 K in bulk material [20]. It was the first measured superconductor that exhibited superconductivity above liquid nitrogen temperature, which is a very attractive property when real applications are considered. Classical type I superconductors all had to be cooled using liquid helium which is more expensive and more technically challenging. The crystal structure of YBCO is shown in figure 2.6, where the lattice constants are  $a = 3.82 \text{ \AA}$ ,  $b = 3.89 \text{ \AA}$  and  $c = 11.68 \text{ \AA}$ . YBCO has a crystal structure that can be thought of as three perovskite unit cells, i.e. a three layer cell on the form ABA with A and B being metal oxide layers, stacked on top of each other. The penetration depths and the coherence lengths of YBCO are  $\lambda_{ab} \simeq 150 \text{ nm}$ ,  $\lambda_c \simeq 800 \text{ nm}$ ,  $\xi_{ab} \simeq 2 \text{ nm}$  and  $\xi_c \simeq 0.4 \text{ nm}$ . The indices  $a$ ,  $b$  and  $c$  correspond to the respective lattice constants.

The reason that the oxygen atoms in the YBCO crystal is numbered as  $7 - \delta$  in the stoichiometric formula is due to the uncertainty of actual oxygen content in real YBCO. Especially in thin films there can be a problem of degradation in the YBCO because of oxygen loss. When  $\delta$  grows the material will gradually go from metallic to semiconducting and finally insulating as shown in figure 2.7.

When making thin films of YBCO some of its bulk properties will inevitably change. The most obvious change is that  $T_c$  will decrease. For films with thicknesses around some tens of nm, a  $T_c$  in the range 85 - 87 K is usually obtained [22], [23]. Other superconducting materials such as NbN can be made in very thin films, typically a few nm. The actual size of the YBCO lattice makes it impossible to have this thickness in a continuous  $c$ -axis oriented film. In this work all films were deposited on  $\text{Al}_3\text{O}_2$  substrates with a  $\text{CeO}_2$  buffer

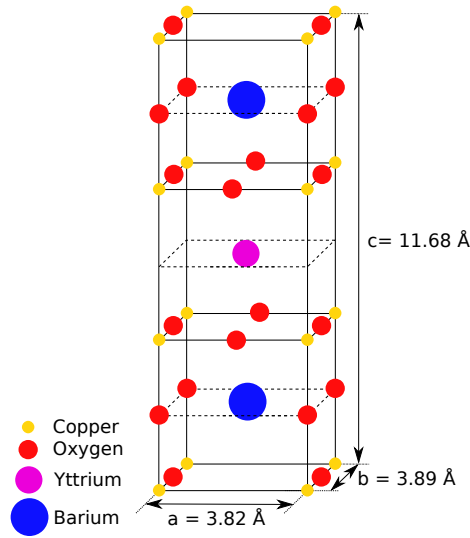
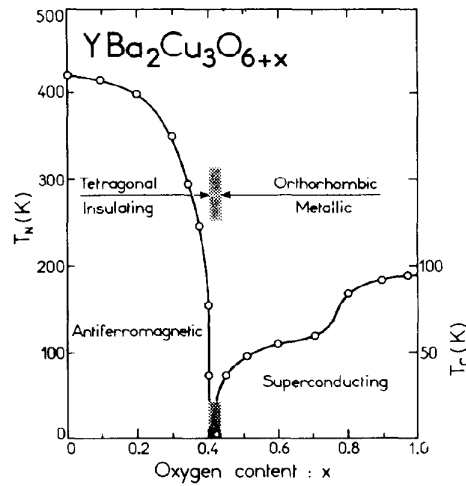


Figure 2.6: YBCO lattice.

Figure 2.7: Graph showing a phase diagram and critical temperature for different oxygen content,  $x$ , where  $x = 1 - \delta$ , in YBCO. Picture taken from [21].

layer and on MgO substrates. Both give  $c$ -axis oriented YBCO films.

## 2.3 Quasi-optical coupling

Since the size of a bolometer is small compared to wavelengths in the THz regime, some extra effort is required to efficiently couple the incoming radiation to the bolometer. This problem has its origin in the angular limit of resolution, given by [24]

$$\Delta l = 1.22 \frac{f\lambda}{D}, \quad (2.32)$$

where  $\Delta l$  is the distance between two objects to resolve,  $f$  a lens focal distance,  $\lambda$  the wavelength and  $D$  an aperture diameter.  $\Delta l$  can here be interpreted as the length of a bolometer,  $f$  some focusing element in front of it and  $D$  the aperture size of the focusing element. Having a bolometer with a typical size around  $1 \mu\text{m}$  and a wavelength of  $1 \text{ mm}$ , the criterion stated in equation 2.32 implies that  $\frac{f}{D} > 8.2 \cdot 10^{-4}$  has to be fulfilled in order to resolve the bolometer, or, equivalently have a focused beam on the bolometer. A common approach to solve this problem is to use a quasi-optical design with a dielectric lens on which an antenna-integrated bolometer is mounted on the flat backside, as suggested by Rutledge and Muha [25]. The main motivation for using an antenna is that it effectively makes  $\Delta l$  bigger, which lessens the demands of the lens.

### 2.3.1 Planar antennas

A bolometer is inherently broadband and the RF frequencies that can be detected by the whole system is in general limited by the bandwidth of the antenna. There are different types of planar antennas that can be used to couple radiation to a bolometer. Some examples are log-spiral, log-periodic and double slot antennas. For this project a log-spiral antenna was chosen. One of its big advantages is theoretical frequency independence (in practice, large bandwidth). This means that important antenna characteristics such as impedance, far field pattern, polarization etc. remain the same when altering the frequency. In general, this can be achieved if the antenna size and frequency are scaled by the same amount [26].

It has been showed that the shape of a frequency independent antenna in spherical coordinates with angles  $(\phi, \theta)$  must satisfy

$$r = F(\theta, \phi) = e^{a\phi} f(\theta), \quad (2.33)$$

where  $r$  is the distance along the antenna surface or edge,  $a = \frac{1}{K} \frac{dK}{dC}$  and  $f(\theta)$  is a completely arbitrary function.  $K$  is a scaling parameter used for the antenna when scaling the frequency by the same amount. This means that if the frequency is scaled by a factor of  $K$ , then  $r$  has to be scaled by the same amount to preserve the electrical dimensions.  $C$  is an angle, chosen such that  $KF(\theta, \phi) = F(\theta, \phi + C)$ . A two-dimensional spiral is then obtained by demanding  $\frac{df}{d\theta} = A\delta(\frac{\pi}{2} - \theta)$ , where  $A$  is a constant and  $\delta$  Dirac's delta function. An illustration of a spiral antenna structure and relevant angles, lengths etc. are found in figure 2.8. Equation 2.33 can now be solved and  $r$  be expressed in number of wavelengths, which gives

$$\rho_\lambda = \frac{r}{\lambda} = Ae^{a(\phi - \ln(\lambda)/a)}. \quad (2.34)$$

By studying equation 2.34 one sees that changing the wavelength means changing  $\ln(\lambda)/a$  which is equivalent to changing  $\phi$ , i.e. to rotate the spiral structure. Since the physical pattern only is rotated to preserve  $\rho_\lambda$  when changing the wavelength, a frequency independent antenna has been obtained<sup>1</sup>.

---

<sup>1</sup>See Balanis' book on antenna theory for a more detailed description [26].

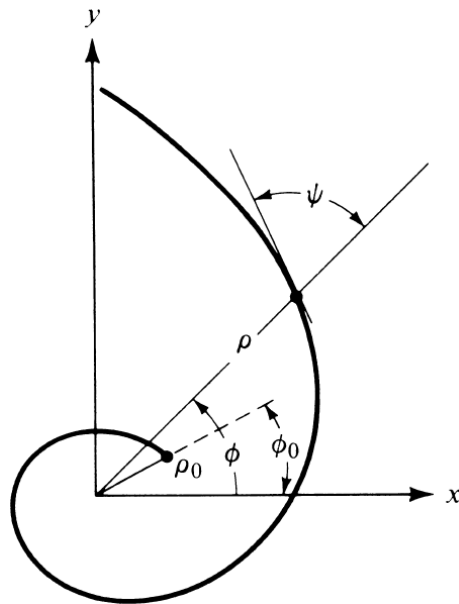


Figure 2.8: Curve showing a single spiral arm. Picture taken from [26].

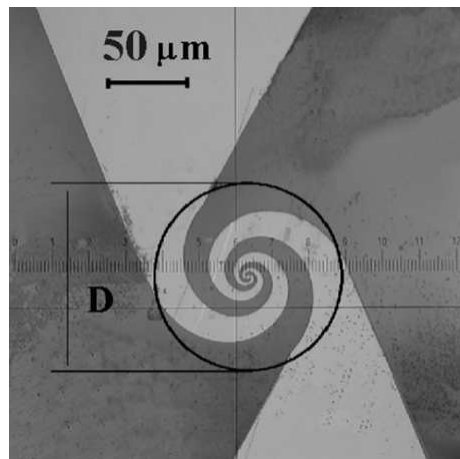
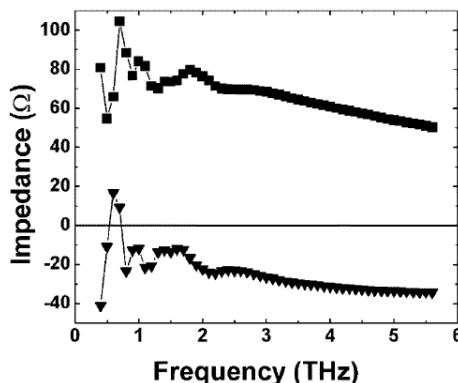


Figure 2.9: Spiral antenna with the outer diameter  $D = 48 \mu\text{m}$  and  $a = 0.36$ . The dark color represents the substrate. Picture taken from [27].



**Figure 2.10:** Graph showing the complex impedance of a log-spiral antenna versus frequency. Squares and triangles denote the real and imaginary parts of the impedance, respectively. Picture taken from [27].

The log-spiral antenna design used in this work is described by Semenov et. al. [27]. Measurements of the antenna impedance versus frequency is shown in figure 2.10. Here the impedance varies linearly in the range 2-6 THz. The antenna used in this work has an impedance of about  $90 \Omega$  which has to be matched to bolometer impedance in order to avoid impedance mismatch loss. Practically this means that the aspect ratio of the bolometer bridge has to be adjusted to achieve a bolometer-antenna impedance match.

### 2.3.2 THz lenses

One of the main motivations for having the antenna-substrate-lens configuration is to eliminate electromagnetic modes in the bolometer substrate. This is achieved by having the dielectric constants of the substrate and the lens similar. An antenna that is placed on a dielectric substrate mainly radiates its power to the dielectric side [28]. Having a high dielectric constant (compared to air) then makes the losses into air small. In addition, a dielectric lens will also focus the beam and therefore enhance the coupling of RF power to the bolometer.

The quasi-optical configuration using a dielectric lens with a bolometer chip on the backside is shown in figure 2.11. The lens used in the experiments, described in chapter 4, is slightly different from the hyperhemispherical type depicted in figure 2.11. What differs between the two is the shape; in particular, the shape of the elliptical silicon lens used in this work is more extended in the radiation propagation direction. An elliptical lens has the property that the beam is diffraction limited by its aperture size [29]. It offers a narrow beam that is highly desirable when performing experiments since it lessens the demands of other focusing elements (lenses, focusing mirrors etc.). One of its disadvantages is that the effective transmission is lowered because of a large incident angle far away from the optical axis. However, having a collimated beam with most of the energy in the optical axis, this problem is not of major importance. An anti-reflection coating can be used to minimize the losses, but

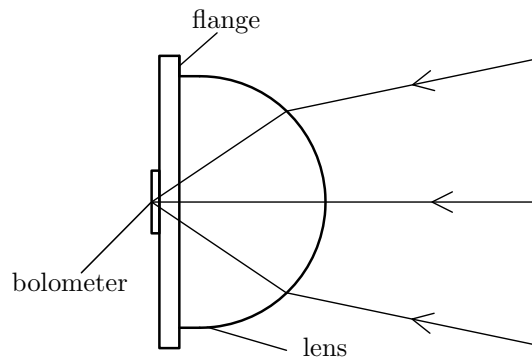


**Figure 2.11:** An antenna-integrated bolometer mounted on the back of a semiconductor lens. The radiation is focused by the lens and then propagates through the substrate (on which the bolometer is mounted) before being absorbed in the bolometer film.

this coating will strongly depend on the wavelength of the incoming radiation. No reflection coating was used in this work.



# Chapter 3

## Design and processing

This chapter will focus on the fabrication of the bolometers - from empty substrates to working devices - that took place in the cleanroom processing laboratory at MC2, Chalmers. Different processing procedures that were used are presented and discussed, whereof one is described in detail in appendix A. Problems that occurred in the processing are also discussed. The hope of the author is that it should be possible for anyone to use this chapter as a manual to fabricate new bolometers, thereof the detailed description.

### 3.1 Design

Spiral antennas, described in section 2.3.1, were coupled to all fabricated bolometers. Only the inner part, i.e. the width of the contact pads, were changed between different devices in order to fit the antenna to the bolometer bridge. Each sample (batch) consisted of a  $10 \times 10 \text{ mm}^2$  substrate containing 10 bolometers. Figure 3.1 is taken from a CAD drawing and it illustrates the layout of a  $2 \times 5$  array of devices on the substrate. Also shown is the antenna pattern and the big electric circuit contacts. All devices were short-circuited on the substrate at all times during the process to protect the bolometers from electrostatic discharges.

To ensure that power absorption only takes place in the center of the antenna, i.e. in the bolometer itself, it was decided to remove the YBCO film everywhere except for small patches, referred to as islands, typically  $20 \mu\text{m}$  long, that overlapped with the antenna. Whether this was necessary or not was never investigated, but the process was kept since it worked. It is illustrated in figure 3.2. To have a sufficiently big overlap can be important to avoid contact resistance between the YBCO island and the antenna. However, since the devices, having the overlap shown in figure 3.2 (about  $2 \times 100 \mu\text{m}^2$ ), had low residual resistance at  $T < T_c$ , the contact resistance dependence on overlap area was not investigated either.

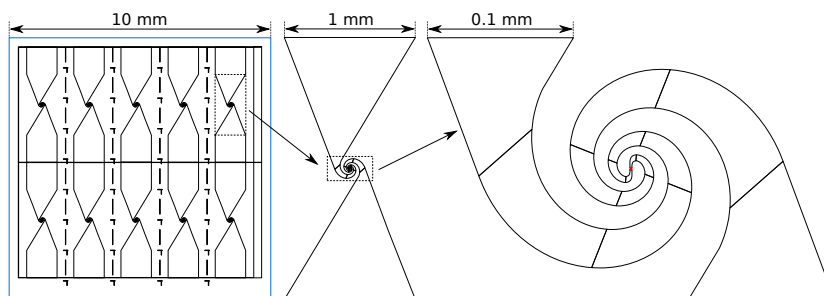


**Figure 3.1:** (left) Layout on  $10 \times 10 \text{ mm}^2$  substrate with  $2 \times 5$  array of devices. Dicing saw and photolithography alignment marks are also visible. The blue line indicates the edge of the substrate. (middle) Single device design, including bolometer, antenna and contact pads. (right) Antenna with bolometer in the middle (red), having typical size  $(2 - 4) \times 1 \mu\text{m}^2$ .

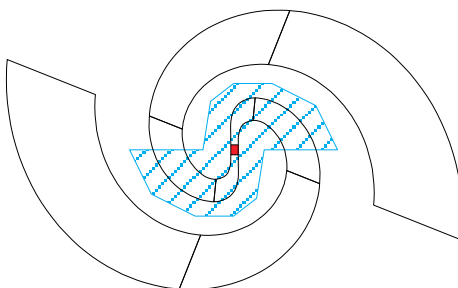


**Figure 3.2:** Inner part of the antenna illustrating the YBCO island-antenna overlap. The blue area denotes the YBCO island and the red rectangle the bolometer site.

## 3.2 Fabrication procedure and material choices

### 3.2.1 YBCO film deposition

The thin YBCO films were deposited on a double side polished R-cut  $(1\bar{1}02)$   $\text{Al}_2\text{O}_3$  (sapphire)  $10 \times 10 \text{ mm}^2$  substrate using a pulsed laser deposition (PLD) technique. A thin layer, 30-40 nm, of  $\text{CeO}_2$  was used as a buffer layer to enable growth of c-axis oriented YBCO, see figure 2.6. Detailed process parameters for  $\text{CeO}_2$  sputtering and YBCO deposition are found in appendix B.1.2 and B.1.3, respectively. Figure 3.4 shows a schematic picture of the deposition process.

After having deposited  $\text{CeO}_2$  and YBCO, the film was protected with a 20 nm thick film of Au. The whole process was done in-situ. To measure  $T_c$  in the films, a test utilizing the Meissner effect was performed. In this test, the substrate was placed between two coils while being cooled. Electric current was driven through the first coil to induce a magnetic field whereas the second coil picked up the signal which dropped significantly at  $T_c$ . The films displayed a  $T_c$  around 86 K which coincided well with the values measured for the finished bolometers. It was therefore concluded that the processing was not harmful for the YBCO films.

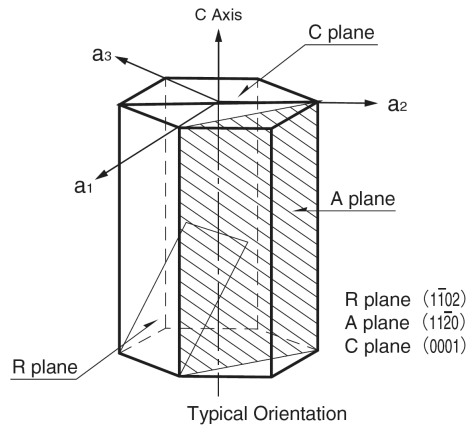


**Figure 3.3:** Sapphire crystal with the R, A and C-planes indicated. Picture taken from [30].

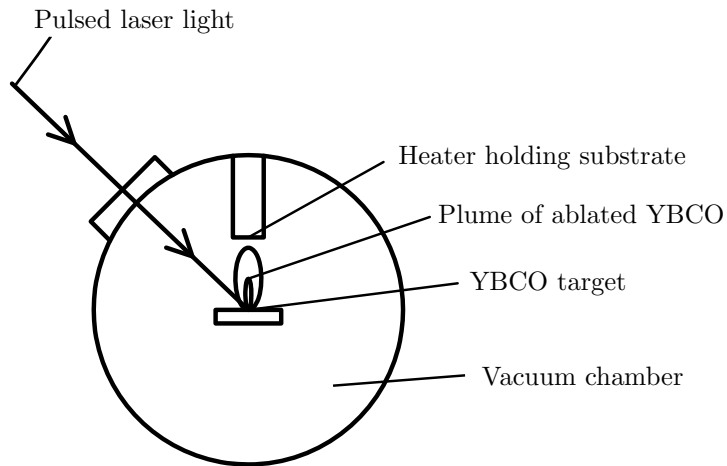


**Figure 3.4:** Illustration of the pulsed laser deposition process. The heater was continuously translated and rotated at a fixed distance from the YBCO source to ensure a uniform film deposition across the whole substrate.

Sapphire is a suitable material for applications in the THz region due to its low loss tangent. Around 17 GHz the loss tangent is about  $10^{-7}$  at 77 K [31]. The high thermal conductivity of sapphire, about 40 W/mK [30] below 100 K, is also important when making a bolometer where fast cooling is crucial for the device performance. Figure 3.3 illustrates the hexagonal crystal structure with the R-plane indicated. Sapphire is birefringent with refractive indices of about 3.07 and 3.41 of the ordinary and extra-ordinary beam [32] (for 90-400 GHz), respectively. In order to investigate how this birefringence influences the RF measurements, a few films were deposited directly on MgO (100) substrates, which is a commonly used substrate for YBCO deposition, [22]. Just like sapphire, it has suitable thermal and optical properties for bolometric applications

in the THz regime. The films displayed a somewhat lower  $T_c$  (85-86 K). No buffer layer was needed and this enabled YBCO growth with c-axis orientation, directly on the MgO substrate. Even though the films seemed promising, no bolometers were fabricated using MgO substrates due to processing issues described in section 3.2.2 below.

### 3.2.2 Bolometer and antenna patterning

All processing described in this section deals with UV photolithography, Ar-ion etching (referred to as ion milling), metal (Au and Ti) evaporation, C deposition using PLD and O<sub>2</sub> RF plasma etching. The processing procedure was developed over time and it is therefore described in three sections below, which were named after the working title of the batches. The devices on a substrate were named according to its position in the 2×5 array. For instance, "device 2:3" refers to the device on row 2 and column 3, see figure 3.1. References are made to the process step descriptions and processing recipes in appendix A and B, respectively.

#### Batch 1 & 2

The first step for these batches was to fabricate a small rectangle defining the width of the bolometer, similar to step 5-8 in appendix A. This was done using positive photolithography (see recipe B.1.5) which left a rectangle of resist that served as protective mask during the following ion milling step. The ion milling was done with the same settings for current, voltage and Ar flow as in B.1.7, but no breaks were taken for cooling. The protective mask of, now hardened, photoresist was removed with Shipley 1165 remover in an ultrasonic bath. The in-situ gold was removed, again with the same ion milling settings, from the rectangle in batch 1 whereas it was kept for batch 2; see figure 3.5 and 3.6 .

Next step was to define the antennas using image reversal photolithography B.1.4, which is shown in figure 3.5 and 3.6 for batch 1 and batch 2, respectively. After followed the deposition of 400 nm Au with a 5 nm Ti adhesive buffer layer according to recipe B.1.8. The lift-off was done using Shipley 1165 remover. It should be added that it was time consuming to get a good alignment for the YBCO rectangles to the antenna pads and this was one of the main motivations for using the islands, as shown in figure 3.2. Batch 1 was now finished since the in-situ Au had been removed earlier. Batch 2 was finished after an ion milling session, analogous to step 17 in A. Dicing of the substrate was done using an automatic dicing saw. The substrate was covered with photoresist to protect it from the cooling water used by the dicing saw.

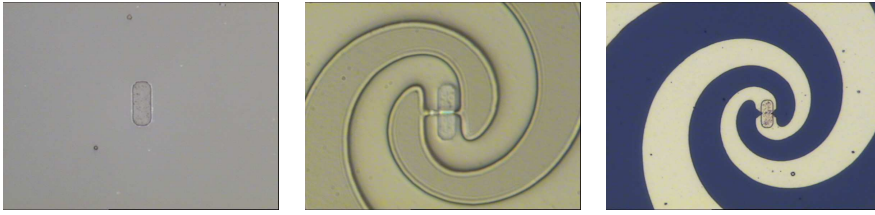


**Figure 3.5:** Processing pictures for batch 1. (left) Exposed YBCO rectangle. (middle) Antenna patterned with AZ 5214 resist prior to Au deposition. (right) Finished bolometer integrated with antenna.

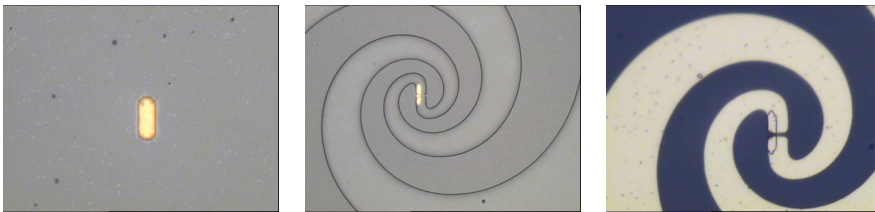


**Figure 3.6:** Processing pictures for batch 2. (left) YBCO rectangle protected with in-situ Au. (middle) Antenna patterned with AZ 5214 resist prior to Au deposition. (right) Bolometer integrated with antenna.

### Batch 3 & 5

The processing procedures for these two batches were identical<sup>1</sup>. Figure 3.7 shows the main steps in the process. First, the bolometer islands were defined (see figure 3.7:1) according to step 5-8 in appendix A. Photolithography recipe B.1.4 was then used to pattern the antennas, see figure 3.7:2. This was the main difference from the process described in appendix A, where the bolometers were defined prior to the antennas. After that, 5 nm Ti and 350 nm Au was deposited. Then, a mask of C was deposited using PLD and the pattern was developed using lift-off in acetone according to recipe B.1.6, see figure 3.7:3. Excess YBCO was then removed using ion milling etching according to recipe B.1.7, see figure 3.7:4. Next step was to use photolithography recipe B.1.5 to pattern small rectangles that effectively defined the bolometer length. A 60-70 nm film of C was then deposited and lifted, again according to recipe B.1.6, figure 3.7:5. At this stage, the whole sample was protected with C, except for the rectangles that defined the bolometers. Recipe B.1.7 was again used, this time to remove the gold from the bolometer bridge. The result is illustrated in figure 3.7:6. The C mask was removed according to recipe B.1.6. The batches were now finished, apart from the dicing step.

As described in section 4.1.1, the bolometers in batch 5 displayed too low resistance and it was therefore decided to make a new batches with the aspect ratios changed to obtain a an impedance that better matched the RF impedance of

<sup>1</sup>Batch 4 was never finished and since the processing for batch 5 was already in progress, the name for the latter was kept.

the antenna.

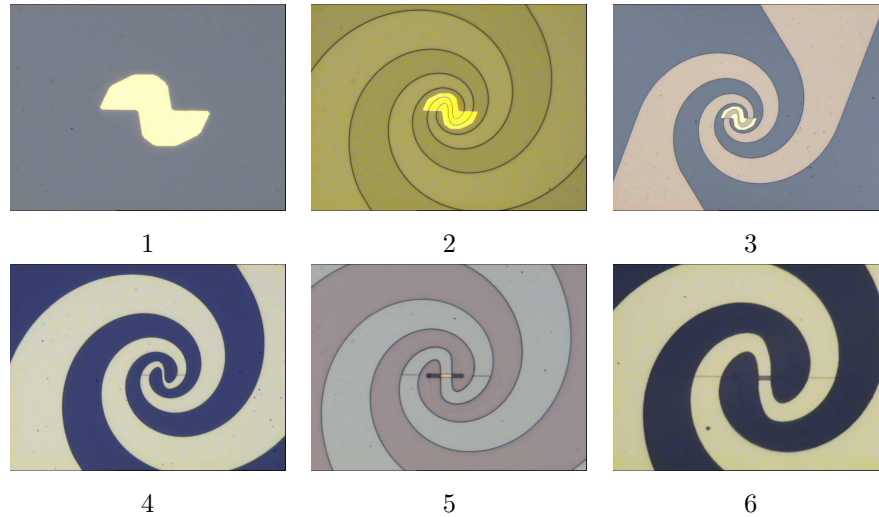


**Figure 3.7:** Processing pictures for batch 3 and 5. 1: YBCO island protected with in-situ Au. 2: Antenna patterned with AZ 5214 resist prior to Au deposition. 3: Au and C deposited to define the antenna. 4: Excess YBCO removed using ion milling. 5: C film deposited with rectangle opening defining the bolometer position. 6: In-situ Au removed from bolometer using ion milling.

### Batch 6-12

Apart from having new aspect ratios of the remaining bolometers, the processing procedure was also simplified. The process is illustrated in appendix A. One difficulty in the process used for batch 3 and batch 5 was that an Au layer,  $350 \text{ nm} + 20 \text{ nm}$ , was left until the final ion milling step. This required a long ion milling etching time, which was undesirable due to the uncertainty of the etching rate of Au. The new process only required ion milling of  $20 \text{ nm}$  Au at the very end of the process. All bolometers for batch 6 - 11 displayed an open circuit impedance which probably was the result of continuous ion milling without pauses. The bolometers from two batches could have deteriorated since the short circuit on the substrate was broken. Before fabricating batch 12, this problem was identified and solved. Thus, batch 12 had performance similar to batch 5, but with higher impedance.

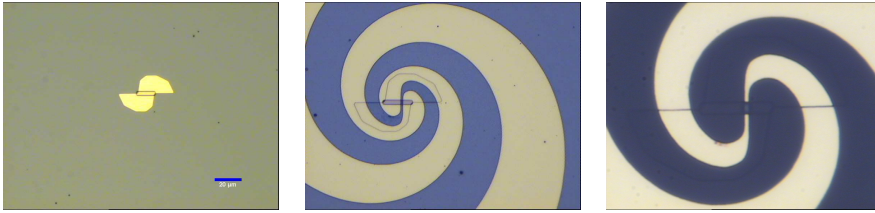


**Figure 3.8:** (left) Island of YBCO with a photoresist rectangle that defines the bolometer length. (middle) Au deposited with a carbon mask defining the spiral antenna pattern. (right) Finished bolometer integrated with an antenna.

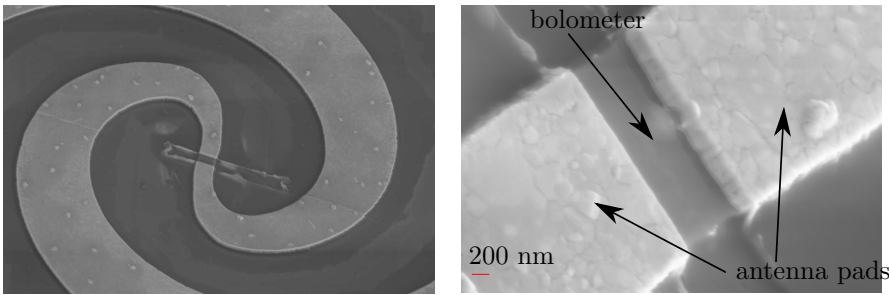


**Figure 3.9:** (left) Scan electron microscope picture of an antenna integrated bolometer. (right) Scan electron microscope picture of the bolometer bridge connected to the antenna contact pads.

### 3.2.3 Submicron bolometers using electron beam lithography

One of the most important conclusions from the measurements, described in chapter 4, was that bolometers with lengths and widths smaller than  $1 \mu\text{m}$  should have better overall performance. A process based on electron beam lithography (e-beam) patterning of the devices, i.e. bolometers and antennas, was therefore investigated. However, due to lack of time it never resulted in any working devices. Nevertheless, the gained experiences are briefly summarized in this section.

The idea for this process was similar to that used for the previous batches, i.e. to first make a small island of superconducting material to which an antenna was coupled. All bolometers were to have a width of  $0.2 \mu\text{m}$  and the width should be varied between  $0.1 \mu\text{m}$  to  $0.5 \mu\text{m}$  for the same batch. The first step was to spin copolymer (MMA 8.5 EL 10), 3000 rpm with 200 ms acceleration for 90 s, and then baking it at  $130^\circ$  for 5 min. The same procedure was done for the resist (PMMA A2). In the first e-beam session, alignment marks (crosses) were patterned and later defined by Au deposition followed by lift-off, see recipe B.1.8.

Next, the islands were patterned in the same fashion as for the alignment marks.

A mask of C was then deposited, analogous with the process described in appendix A, see figure 3.10. This was followed by an ion milling step according to recipe B.1.6. The next step was to make a combined exposure for the bolometer contact pads and a current dose test on the same sample. The resist was prepared as described above. here was a build-up of charge in the dielectric substrate during the exposure which completely ruined the process. All contact pads were heavily misaligned and marks from discharge currents were visible near every exposed part of the sample, see figure 3.10. It was concluded that some film, Al or ESPACER conductive resist for example, needs to be deposited on the sample prior to this e-beam step to enable removal of charges.

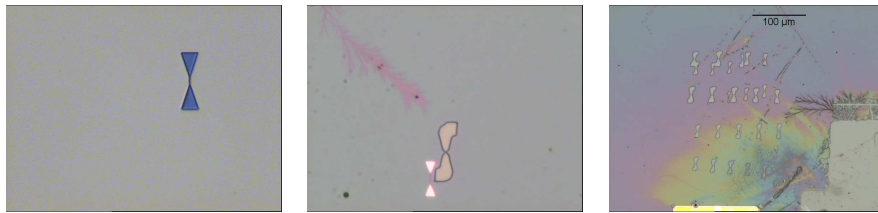


**Figure 3.10:** (left) Island of YBCO with  $0.2 \mu\text{m}$  bridge. (middle) Heavily misaligned contact pad and discharge. (right) Failed dose test and massive discharges.

## Chapter 4

# Measurements, results and analysis

In this section all experimental results are presented. The measurements setups are illustrated and the validity of the methods are motivated. The subsequent analysis is based on the bolometer theory in section 2.1. One dimensional bolometer temperature profiles, for different bias currents, are calculated using a second order non-linear differential equation. The calculated data is then used to calculate theoretical plots of the current versus voltage (I(V)-curves).

### 4.1 DC characteristics

Prior to all RF tests a DC test was made for all bolometers. It consisted of two parts. First, the voltage was measured while the device was cooled from room temperature to 77 K at constant current bias of  $1 \mu\text{A}$ . This data was used to obtain a resistance versus temperature curve (R(T)-curve) which clearly showed the transition into the superconducting state. After that, at 77 K, I(V)-curves were recorded. The current was swept so that it well exceeded  $I_c$ .

#### 4.1.1 DC measurements

The DC measurements were made using a dip-stick, as shown in figure 4.1. All devices were broken for batch 1. Afterwards it was clear that the film degraded during the processing, since the YBCO film was unprotected for several processing steps and an oxygen loss was therefore likely. The bolometers all displayed an open circuit impedance.

#### Batch 2

The results from batch 2 is shown in figure 4.2. As described in section 3, some bolometers were disconnected from the contact pads and therefore no DC measurements were performed for these. When studying figure 4.2, it is clear that the characteristics differs a lot between the bolometers. Devices 1, 7, 8

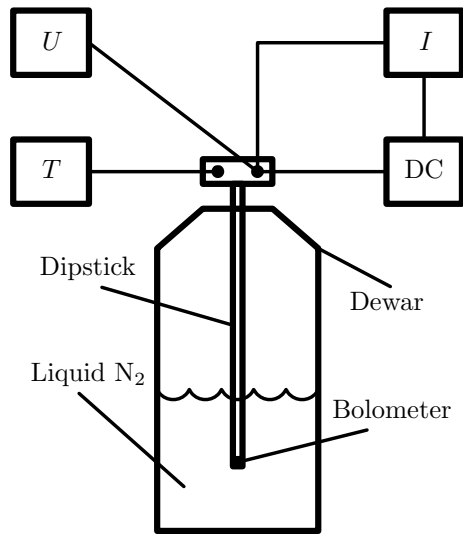


**Figure 4.1:** Schematic sketch of the setup showing the dipstick with a bolometer mounted on the inside. Current, voltage and temperature readouts are marked with  $I$ ,  $U$  and  $T$ , respectively. DC denotes the constant current source.

and 9 all have a negative  $\alpha$  for  $T > T_c$ . The origin of behavior is hard to determine, but one hypothesis is that the YBCO film quality across the  $10 \times 10$  mm substrate was uneven. Another explanation can be the remover (Shipley 1165) that was used for washing and lift-off for this batch. It is known to be more aggressive than acetone and it is not impossible that it influenced the film quality. The bolometers from batch 2 were never tested in any RF experiments.

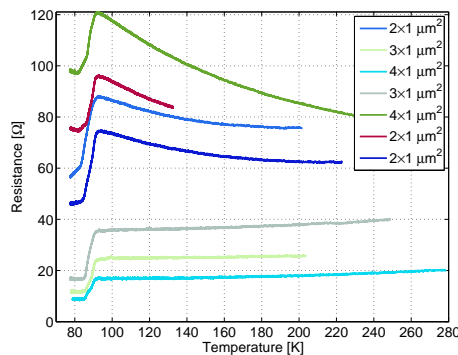


**Figure 4.2:** Resistance versus temperature for bolometers from batch 2.

### Batch 3

As mentioned in section 3, the processing procedure was changed after batch 2 which proved to give better overall results. Figure 4.3 shows the DC results for batch 3:

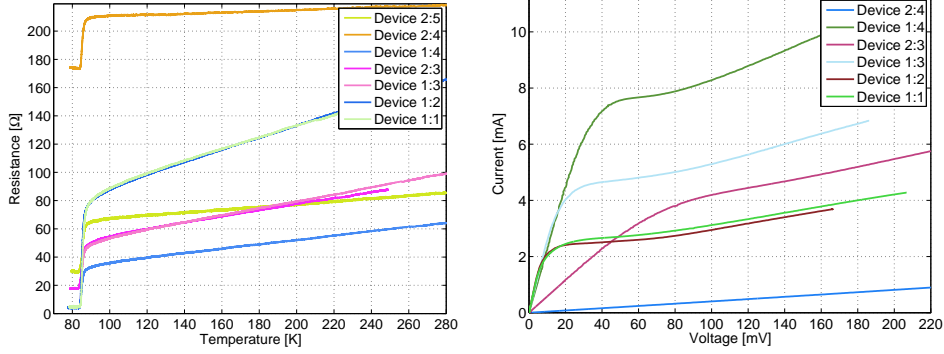


**Figure 4.3:**  $R(T)$  and  $I(V)$  curves for batch 3.  $R(T)$  was recorded in a constant current mode with a bias current of  $1\mu\text{A}$ . The temperature was 77 K.

All bolometers made a transition, but only device 1:4, 1:3, 1:2 and 1:1 reached a superconducting state. The fact that these bolometers were from the first row may suggest a non-uniform YBCO film quality or partial degradation in some unknown processing step. It should be added that device 1:5 was never measured since one spiral arm of its antenna was detached. Relevant data for batch 3 is found in table 4.1.  $T_c$  is here defined as the temperature where  $\frac{dR}{dT}$  has its maximum. Since device 1:4, 1:3, 1:2 and 1:1, which have different bolometer geometries, show the same residual resistance for  $T < T_c$  makes it possible to deduce that the residual resistance is due to resistance in cables, contacts etc.

Device	1:1	1:2	1:3	1:4	2:3	2:4	2:5
$w$ [ $\mu\text{m}$ ]	2	2	3	4	3	4	4
$T_c$ [K]	86.6	86.5	85.7	86.2	87.5	87.5	87.5
$R\alpha(T \gg T_c)$ [ $\Omega/\text{K}$ ]	0.40	0.42	0.25	0.15	0.21	0.05	0.10
$\Delta T$ [K]	2.0	2.3	1.4	2.1	2.5	2.5	2.5
$R(T \approx 300 \text{ K})$ [ $\Omega$ ]	168	171	103	65	97	218	87
$R(T < T_c)$ [ $\Omega$ ]	4.47	4.07	3.97	4.65	17.62	$\sim 175$	$\sim 30$

**Table 4.1:** DC parameters for batch 3.  $w$  is the nominal bolometer width,  $T_c$  critical temperature,  $R$  resistance and  $T$  temperature.  $\Delta T$  denotes the width of the superconductive transition. All bolometer lengths were  $1 \mu\text{m}$ .

From the data in table 4.1 one can easily compute the sheet resistance of the YBCO film as

$$R_{\square} = \frac{Rw}{L} = \frac{\rho L w}{s L} = \frac{\rho L w}{dw L} = \frac{\rho}{d}, \quad (4.1)$$

where  $L$  is the bolometer bridge length,  $s$  the cross sectional area,  $\rho$  the resistivity and  $d$  the film thickness. If  $d$  is known, then  $\rho$  can be calculated, but since  $d$  was never measured for the films - from which the actual devices were fabricated

- it is assumed that the nominal thickness,  $d = 50$  nm, is correct. Excluding the devices with highest and lowest room temperature sheet resistance, i.e. device 1:4 and device 2:4, one can calculate the mean value for the sheet resistance and the film resistivity:

$$R_{\square, \text{batch 3}} = 325 \Omega$$

$$\rho_{\text{batch 3}} = 1.63 \cdot 10^{-5} \Omega\text{m}$$

### Batch 5

Seven bolometers from batch 5 were measured and the results are shown in figure 4.4:

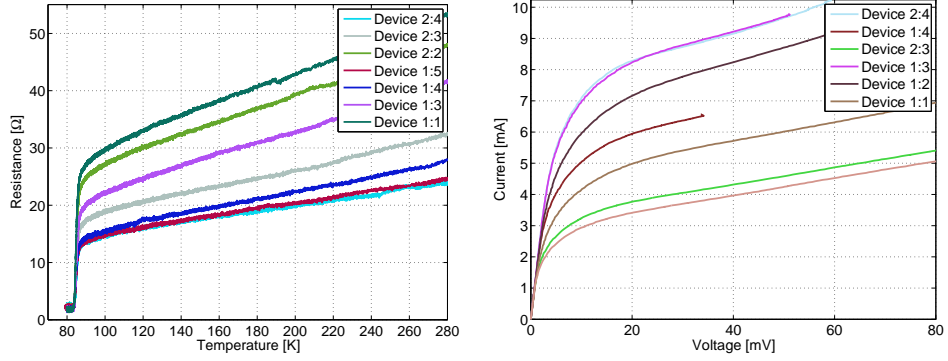


**Figure 4.4:**  $R(T)$  and  $I(V)$  curves for batch 5.  $R(T)$  was recorded in a constant current mode with a bias current of  $1\mu\text{A}$ . Device 2:2 broke before its  $I(V)$  was recorded. The temperature was 77 K.

The remaining bolometers were disconnected because of broken antennas. However, when comparing figure 4.3 and 4.4 it is obvious that the results were much more even for batch 5. Bolometers of similar size have similar  $R(T)$  and  $I(V)$  characteristics. It is also worth to note that all bolometers reached the superconducting state this time. A summary of the most important data from the DC measurements is found in table 4.2

Using equation 4.1 again gives the sheet resistance and resistivity:

$$R_{\square, \text{batch 5}} = 78.7 \Omega$$

$$\rho_{\text{batch 5}} = 3.94 \cdot 10^{-6} \Omega\text{m}$$

Because of the much lower sheet resistance these bolometers had worse impedance matching to the antenna and it was therefore decided to fabricate longer bolometers to get a transition to the superconducting state at  $R(T \gtrsim T_c) \simeq 100 \Omega$ .

Device	1:1	1:3	1:4	1:5	2:2	2:3	2:4
$w$ [ $\mu\text{m}$ ]	2	3	4	4	2	3	4
$T_c$ [K]	86.0	86.4	86.0	86.2	86.3	86.3	86.7
$R\alpha(T \gg T_c)$ [ $\Omega/\text{K}$ ]	0.13	0.10	0.07	0.05	0.11	0.07	0.05
$\alpha(180\text{K})$ [ $\text{K}^{-1}$ ]	0.0031	0.0033	0.0031	0.0027	0.0030	0.0030	0.0026
$\Delta T$ [K]	2.1	2.7	2.3	2.4	2.4	2.4	3.2
$R(T \simeq 300\text{K})$ [ $\Omega$ ]	55	43	29	25	50	35	30

**Table 4.2:** DC parameters for batch 5.  $w$  is the nominal bolometer width,  $T_c$  critical temperature,  $R$  resistance and  $T$  temperature.  $\Delta T$  denotes the width of the superconductive transition.

### 4.1.2 Calculation of temperature profiles under DC bias

In a lumped element model, it is assumed that heating in a bolometer bridge is entirely uniform. In reality this is, of course, not the case. A simple one-dimensional single temperature model for the heat distribution in the bolometer is considered here. More advanced models employ a two temperature description where the temperature of electrons and phonons are divided into two interacting subsystems. Such a model is used in reference [33].

The purpose of doing these calculations is to get a rough understanding of the workings of a fabricated bolometer. Temperature profiles are calculated for different bias currents and these are used to calculate the I(V) characteristics of a bolometer. It is assumed that the heat produced in the bolometer is purely ohmic. The ability to calculate an I(V) curve which coincides fairly with what is measured gives validity to the model and it indicates how the thermal bolometer parameters ( $C$ ,  $G$  etc.) influence the actual electric characteristics.

The heat balance equation 2.1 is formulated for a case with a time variant power  $P(t)$ . It is assumed in the following calculations that the power is time invariant and a steady state is therefore obtained for the heat distribution.  $T = T(x)$  denotes the temperature variation along the bolometer, i.e. in the direction  $x$  in which the current flows. A one dimensional heat equation can now be used:

$$Ks\nabla^2 T + q(x) = Ks\frac{d^2 T}{dx^2} + q(x) = p(x), \quad (4.2)$$

where  $K$  is the thermal conductivity,  $s = wd$  the cross sectional area of the bolometer.  $p(x)$  represents the space dependent ohmic heat dissipation in the bolometer and  $q(x)$  the space dependent heat removal process.  $p(x)$  and  $q(x)$  are given by

$$p(x) = \frac{I^2}{s}\rho(x) = \frac{I^2\rho}{s\left[1 + \exp\frac{T_c - T(x)}{\Delta T}\right]}, \quad (4.3)$$

and

$$q(x) = \frac{c_{\text{vol}}s}{\tau}(T(x) - T_0), \quad (4.4)$$

where  $\rho(x)$  denotes the resistivity as a function of  $x$  and  $\rho$  the normal state resistivity. Other parameters have been introduced in section 2.1. Matlab's numerical boundary value problem solver `bvp4c` [34] was used to solve equation 4.2. The resistance for a given current is calculated as

$$R = \int \frac{\rho s}{1 + \exp \frac{T_c - T(x)}{\Delta T}} dx \approx \Delta x \sum_i \frac{\rho s}{1 + \exp \frac{T_c - T(x_i)}{\Delta T}}, \quad (4.5)$$

where the summation on the right hand side is the numerical implementation used to calculate  $R$  once  $T(x)$  is known.  $\Delta x$  denotes a small length segment of the bolometer and is specified in the numerical solver. Figure 4.5 and 4.6 show the results from the calculations where it is assumed that the temperature at the boundaries, i.e. at the antenna contact pads, are 77 K.

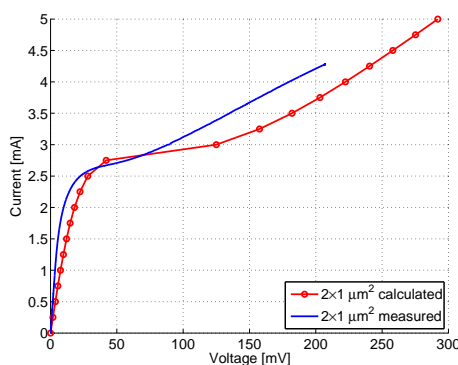


**Figure 4.5:** Calculated and measured I(V) characteristics for dev 1:1 from batch 3.

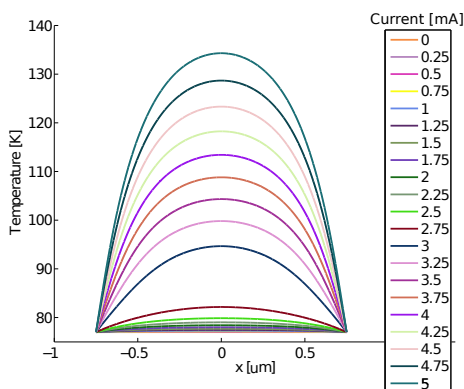


**Figure 4.6:** Calculated temperature profiles showing temperature versus bolometer  $x$  coordinate for device 1:1 from batch 3.

An iterative approach was used to obtain the results in figure 4.5 and 4.6, meaning that the constants  $\rho$ ,  $\Delta T$ ,  $K$  and  $c$  were altered to obtain a decent fit. The parameters,  $T_c$ ,  $\Delta T$  and  $\tau$ , were measured experimentally ( $\tau$  is calculated in section 4.3.1). This means that the actual numbers used to obtain the results

do not necessarily correspond to the real values of the physical entities.

It is clearly seen in figure 4.5 that the critical current is mimicked even though the model does not include any theory of superconductivity. A corresponding "jump" for a currents around 2.75 mA are seen in figure 4.6. This model predicts an entirely linear  $I(V)$  curve with  $R = 62.2 \Omega$  for  $I > 4$  mA where the bolometer is driven into a normal state. This value can be compared to a measured value of about  $48 \Omega$ . How valid this model is at higher currents is unclear. High temperatures in the film may cause the assumed boundary conditions to break down and constants such as  $K$  may vary with temperature.

## 4.2 Direct detection

Prior to the mixing experiments, a direct detection investigation was done to the tested bolometers. The frequencies which were investigated were 100 GHz, 350 - 530 GHz, 690 GHz and 1.63 THz. At 100 GHz, Gunn diodes were used with relatively high output power (10 mW) and good frequency stability. Backward wave oscillators (BWOs) were used for 350 - 530 GHz whereas a far infrared (FIR) gas laser was used at 690 GHz and 1.63 THz. A simplified experimental setup is shown in figure 4.7.

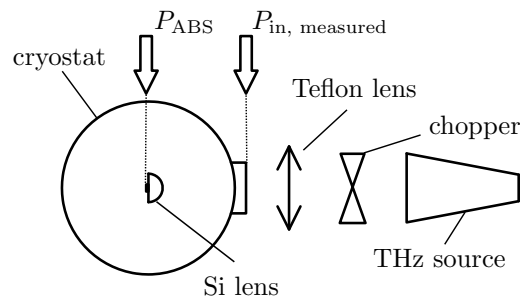


**Figure 4.7:** A simplified, not including readout circuitry, experimental setup for direct detection measurements. Two power reference planes are indicated by  $P_{ABS}$  and  $P_{in, measured}$ , where the former is the absorbed power in the film and the latter is the power measured outside the cryostat window.

A mechanical chopper, with a frequency reference signal to the lock-in amplifier, was used to modulate the beam from the source. The beam was aligned to the detector by moving the cryostat and the lens until a maximum was found. It was assumed that the best possible coupling, i.e. well collimated and centered beam, was obtained when the signal readout was the highest and when the system was very sensitive to movements. The reflection/transmission losses in the cryostat window (made of Teflon) were measured to be 30% for all used frequencies, i.e. a power transmission factor of 0.7. The polarization of the antenna beam is in general elliptical [27]. Therefore, a factor of 0.5 was used for all frequencies to account for the polarization mismatch between the linearly polarized source and the elliptically polarized antenna beam. This assumption was later justified experimentally by rotating the bolometer  $90^\circ$  outside the cryostat while recording how signal changed.

### 4.2.1 Responsivity

Batch 3 was tested around 77 K whereas batch 5 was tested at room temperature. The setup was simpler at room temperature since no cryostat was needed. All measurements were performed in a constant current mode.

#### Superconducting state

Device 1:1 from batch 3 was measured at frequencies 330, 530, 690, and 1630 GHz at a temperature of 77 K. Device 1:3 from the same batch was measured at 330 GHz, also at 77 K. The results are summarized in figure 4.8:

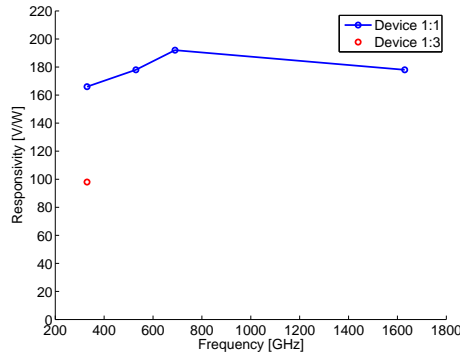


**Figure 4.8:** Measured responsivity at 77 K and modulation frequency 18 Hz for two different devices from batch 3. The reference plane for the incoming RF power is taken outside the cryostat window.

The incoming power was measured outside the cryostat using a Thomas Keiting power meter at 1.63 THz and an Erickson PM4 for the other frequencies. The responsivity was calculated as  $S_V = \frac{2.3 \cdot \Delta U_{\text{lock-in}}}{P_{\text{REF}}}$ , where  $\Delta U_{\text{lock-in}}$  is the voltage swing read off from the lock-in amplifier and  $P_{\text{REF}} = 0.5 \cdot 0.7 \cdot P_{\text{in, measured}}$ . The factor  $2.3 \simeq \sqrt{2} \cdot 1.6$  is included to compensate for the fact that the lock-in amplifier shows the root mean square value of the amplitude instead of the peak-to-peak value. Figure 4.9 illustrates the measured voltage swing when an RF signal is applied.

Combining equations 2.12 and 2.13 gives that the responsivity can be written as  $S_V = \frac{IR(T_0)\alpha}{(G_{\text{dyn}} - I^2 R(T_0)\alpha)(1 + \omega^2 \tau^2)}$ . Using the chain rule, the dynamic thermal conductance can be rewritten as

$$G_{\text{dyn}} = \left. \frac{dP}{dT} \right|_{T=T_0} = \left. \frac{dP}{dR} \right|_{R=R(T_0)} \left. \frac{dR}{dT} \right|_{T=T_0}. \quad (4.6)$$

Knowing the bias point of operation, the numerical values for  $\frac{dP}{dR}$  and  $\frac{dR}{dT}$  at  $T_0$  can be obtained by taking the data from an I(V) curve and plotting  $P = VI$

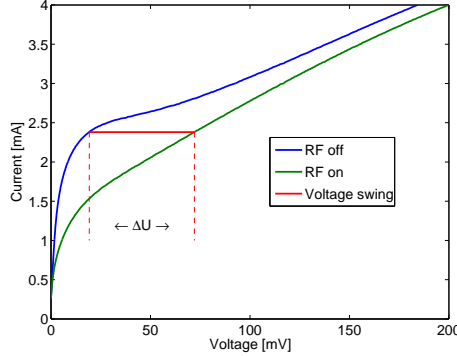


**Figure 4.9:** Two I(V) curves with the measured voltage swing indicated with a red line.

versus  $R = V/I$ . Equation 4.6 and 2.13 can be combined, yielding

$$\begin{aligned}
 S_V &= \frac{IR(T_0)\alpha}{(G_{\text{dyn}} - I^2R(T_0)\alpha)(1 + \omega^2\tau^2)} \\
 &= \frac{I \frac{dR}{dT} \Big|_{T=T_0}}{\left[ \frac{dP}{dR} \Big|_{R=R(T_0)} \frac{dR}{dT} \Big|_{T=T_0} - I^2 \frac{dR}{dT} \Big|_{T=T_0} \right] (1 + \omega^2\tau^2)} \\
 &= \frac{\left[ \frac{dP}{dR} \Big|_{R=R(T_0)} - I^2 \right] (1 + \omega^2\tau^2)}{I} \\
 &\approx \frac{\left[ \frac{dP}{dR} \Big|_{R=R(T_0)} - I^2, \right]}{I}
 \end{aligned} \tag{4.7}$$

where the last step is valid provided that  $1 \gg \omega^2\tau^2$ . If  $\frac{dP}{dR} \Big|_{R=R(T_0)} \gg I^2$ , then the responsivity can be written as

$$S_V = I \frac{dR}{dP} \Big|_{R=R(T_0)} \equiv IC_0. \tag{4.8}$$

Hence, the relevant data needed for a rough estimate of the responsivity is obtained from the plot showing the dissipated DC power as function of resistance. The approximate operation points for device 1:1 was 40 mV, 2.65 mA ( $R = 15.0 \Omega$ ) and 30 mV, 4.50 mA ( $R = 6.7 \Omega$ ) for device 1:3. To get the actual resistance over the bolometer bridge, it is necessary to subtract the voltage drop in cables and other equipment. The residual resistances are found in table 4.1. Using this together with the data from figure 4.10 one obtains  $\frac{dP}{dR} \Big|_{R=R(T_0)} = 7.63 \cdot 10^{-6}$

W/ $\Omega$  and  $\frac{dP}{dR} \Big|_{R=R(T_0)} = 2.25 \cdot 10^{-5}$  W/ $\Omega$  for device 1:1 and device 1:3, respectively. Plugging this into equation 4.7 gives

$$S_V = 4362 \text{ V/W, for device 1:1}$$

and

$$S_V = 2000 \text{ V/W, for device 1:3.}$$

The vast deviation from the measured responsivity values might have several explanations. First, the calculations above assume that all (incident)

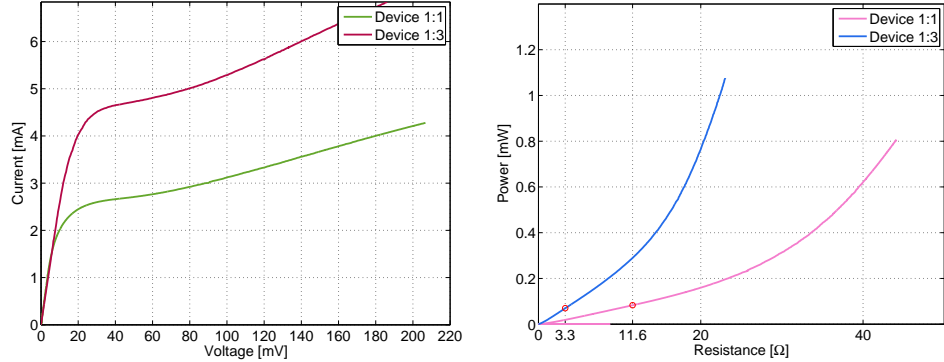


**Figure 4.10:** (left) Plot showing I(V) curves for device 1:1 and 1:3. (right) Plot showing the dissipated DC power as a function of resistance at 77 K with no incident RF power. The operation resistances 11.6  $\Omega$  and 3.3  $\Omega$  for device 1:1 and 1:3, respectively, are marked with red circles.

power is absorbed which is of course not the case for a real detector. By studying two I(V) curves, one with no RF signal (unpumped) and one with the full RF signal (pumped), it is possible to calculate the absorbed power using the isothermal technique. It is then assumed that the response is entirely bolometric, i.e. the change in resistance is due only to the increased temperature. This means that two I(V) curves, one pumped and the other unpumped, are plotted simultaneously together with a line of constant resistance. The intersections then gives two bias points, where the difference in corresponding DC power gives the absorbed RF power. This technique is illustrated in figure 4.11, where  $P_1 = I_1 U_1$  and  $P_2 = I_2 U_2 + P_{\text{RF}}$ . Solving for  $P_{\text{RF}}$  with  $P_1 = P_2$  gives  $P_{\text{RF}} = U_2 I_2 - U_1 I_1$ . This technique has best accuracy when the RF power is much less than the total power in the bolometer.

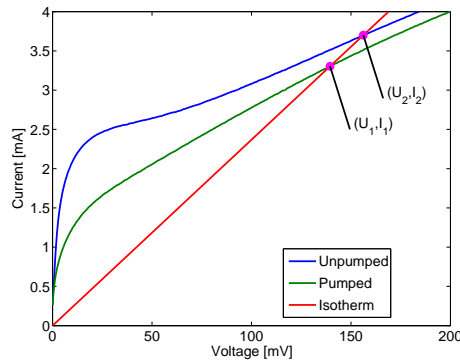


**Figure 4.11:** The isothermal technique illustrated. The absorbed power is given by  $P_{\text{RF}} = U_2 I_2 - U_1 I_1$ .

There is also some uncertainty about antenna properties such as the impedance

and beam polarization. Assuming an antenna impedance of  $90 \Omega$  and taking the bolometer impedance from the  $R(T)$  curves in figure 4.3 at the point where superconducting transition takes place one gets the reflection coefficients

$$|\Gamma|^2 = \left( \frac{90 - 80}{90 + 80} \right)^2 = 0.0035, \text{ for device 1:1}$$

and

$$|\Gamma|^2 = \left( \frac{90 - 50}{90 + 50} \right)^2 = 0.0816, \text{ for device 1:3.}$$

The assumed antenna-signal polarization coupling factor of 0.5 can overestimate the responsivity by a factor of 2 maximum. However, it can also underestimate the responsivity by an arbitrary factor. A bolometer to source beam mismatch can also play a role.

Since the boiling temperature of liquids decrease with pressure, it was possible reach temperatures between 77 K and 66 K by lowering the pressure in the liquid nitrogen container. Doing this increases the critical current, which is seen in figure 4.12. The bolometers will therefore operate with a bigger voltage swing and consequently a larger responsivity. Figure 4.13 shows the responsivity versus temperature for device 1:1 from batch 3. The responsivity goes up rapidly for temperatures down to 76 K and it seems like it would be desirable to cool the bolometers even further. This is not the case though. If the  $I(V)$  curves shown in figure 4.12 are considered, one sees that the state of the bolometer is such that  $\frac{dV}{dT}$  is very high just above the critical current. Because of this the curves are recorded in a constant voltage mode to avoid unstable voltage oscillations. This instability of the device increases voltage fluctuation noise considerably and makes the bolometer useless for  $T < 76$  K.

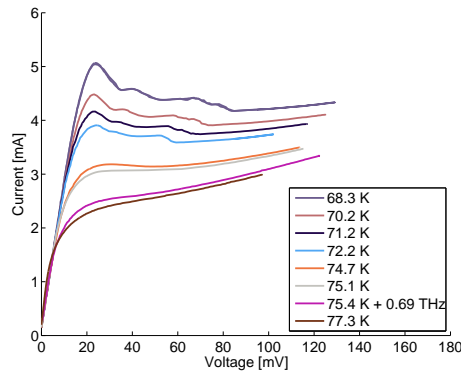


**Figure 4.12:**  $I(V)$  curves recorded in a constant voltage mode at different temperatures.

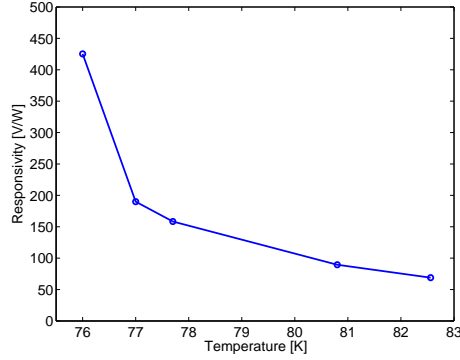


**Figure 4.13:** Measured responsivity at different temperatures and modulation frequency 18 Hz for device 1:1 from batch 3. The reference plane for the incoming RF power is taken outside the cryostat window. The RF frequency was 330 GHz. Best bolometer response was obtained at 40 mV bias voltage for all temperatures.

### Room temperature

These measurements were performed at 100 GHz and 330 GHz. Both sources were equipped with horn antennas. A measurement setup similar to the one illustrated in figure 4.7 was used, but since the bolometers were not cooled, no cryostat was needed. Figure 4.19 shows a photograph of the mixing experiment setup at room temperature. This setup was also used for direct detection, but with a single source. Again, the bolometers were biased with constant current and the voltage oscillations were read out using a lock-in amplifier.

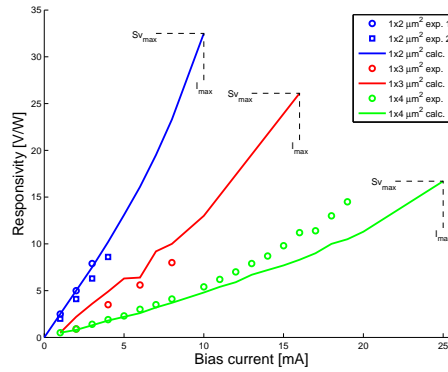


**Figure 4.14:** Plot showing the measured responsivity versus bias current at room temperature for devices with sizes  $2 \times 1 \mu\text{m}^2$ ,  $3 \times 1 \mu\text{m}^2$  and  $4 \times 1 \mu\text{m}^2$  from batch 5. Predicted responsivities are drawn with solid lines. The RF frequency was 100 GHz.

When having a superconducting bolometer operating at room temperature, well above  $T_c$ , the responsivity will drop significantly. The main reason is that  $\alpha$  will decrease, which is clearly seen in figure 4.4. The measurement results

are summarized in figure 4.14. Here the responsivity has been measured versus bias voltage at 100 GHz. When the responsivities were obtained, the power reference was taken as the absorbed RF power. This method was verified by feeding a 1 GHz signal of known power via the antenna contact pads while measuring the I(V) characteristics.

Again, equation 2.12 and 2.13 can be used to understand how the responsivity will behave. A large increase of the current at cryogenic temperatures will drive the bolometer into a resistive state where  $\alpha$  and consequently the responsivity are drastically reduced, see figure 4.12. This is not the case at room temperatures where the R(T) curves are linear, see figure 4.4. Increasing the bias current increases the responsivity, see equation 2.11. However, as described in section 2.1.2, increasing the bias current will eventually break the device. This breakage was seen for some devices from batch 5 which completely deteriorated due to overheating in the film. To avoid this thermal runaway an upper limit for the bias current  $I_{\max}$  was satisfying

$$I_{\max}^2 \alpha R = 0.3 G_{\text{dyn}}. \quad (4.9)$$

The corresponding maximum voltages are indicated in figure 4.14. A highest responsivity of 15 V/W was measured for a  $4 \times 1 \mu\text{m}^2$  device. For a  $2 \times 1 \mu\text{m}^2$  device a responsivity of at least 30 V/W was predicted.

The thermal conductance was experimentally obtained at 292 K for three different devices using equation 4.6 and the measured I(V) curves,

$$G_{\text{dyn}} = 1.45 \cdot 10^{-4} \text{ W/K}, A = 4 \times 1 \mu\text{m}^2$$

$$G_{\text{dyn}} = 0.86 \cdot 10^{-4} \text{ W/K}, A = 3 \times 1 \mu\text{m}^2$$

$$G_{\text{dyn}} = 0.53 \cdot 10^{-4} \text{ W/K}, A = 2 \times 1 \mu\text{m}^2,$$

which shows how  $G_{\text{dyn}}$  scales linearly with the area  $A$ . Small bolometers therefore implies smaller values for  $I_{\max}$ , i.e. higher responsivity for the corresponding bias current. From equation 4.8,

$$S_V = I \frac{dR}{dP} \Big|_{R=R(T_0)} = \frac{I}{G} \frac{dR}{dT} \Big|_{T=T_0} = \frac{\alpha R I}{G}.$$

From table 4.2, it is clear that  $\alpha$  stays constant as the area decreases while  $R$  increases. Thus, it is possible to conclude that a reduction of the bolometer area will increase the responsivity significantly.

### 4.3 Mixing

The mixing experiments were performed at both cryogenic and room temperature with LO frequencies of 100 and 530 GHz. At 690 GHz and 1.63 THz there was no matching RF source to enable mixing. A sketch of the experimental setup is shown in figure 2.2. The output signal was read out using a spectrum analyzer or a lock-in amplifier, depending on the noise level at the measured frequency. Gain-bandwidth was measured as was the LO power dependence of the gain.

### 4.3.1 Superconducting state

Device 1:1 from batch 3 was used for all mixing experiments at cryogenic temperatures. The results from measurements at 100 and 530 GHz are depicted in figure 4.16. A thin film of Mylar was used as a beam splitter to combine the two signals. The output signal was measured using a two-stage amplifier system prior to the spectrum analyzer. The IF chain - i.e. the coaxial cables and the amplifiers - was calibrated using a tunable RF source and a spectrum analyzer. When using BWO sources, the LO frequency was tuned by changing the anode-cathode voltage. Since the output power for a BWO scales with the anode-cathode voltage it was necessary to adjust the bias voltage to remain the absorbed power in the bolometer constant. To measure the LO power, the isothermal technique was employed and the RF power was measured using the responsivity results presented in section 4.2.1. Figure 4.15 illustrates mixing using two BWO sources.



**Figure 4.15:** Mixing experiment using two BWO sources. The beam splitter is mounted inside a block also containing a polarization grid power attenuator.

Theoretically, the measured gain  $g$  can be understood by studying equation 2.24 which, once again, is given by

$$g(\omega_{IF}) = \frac{g(0)}{1 + \omega_{IF}^2 \tau^2}.$$

What is interesting here is to extract a value for  $\tau$  by making a fit for the measured gain. However, to do this it is necessary to have sufficient data at high frequencies and at low frequencies where the gain versus  $\omega_{IF}$  curve flattens (in logarithmic scale). It was difficult to measure the gain at low IFs for 530 GHz LO since the IF signal was broad and the spectrum contained many

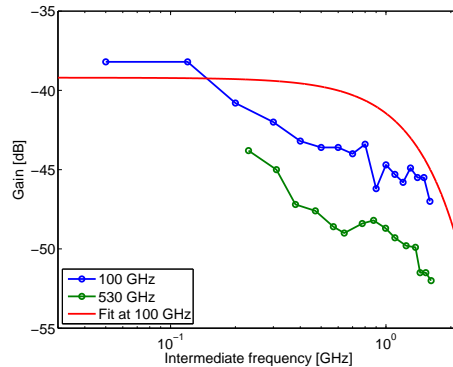


**Figure 4.16:** Mixing at 77 K for device 1:1 from batch 3. The fit is made with  $\tau = 0.24$  ns.

disturbing signals. When using Gunn diodes at 100 GHz it was easier to make accurate measurements at low frequencies since the IF signal width was much narrower.

$\tau$  is 0.24 ns in the 100 GHz fit in figure 4.16. One way to improve the gain bandwidth is to make bolometers based on thinner films. This is clear when studying equation 2.15 where  $\tau$  scales linearly with the thickness  $t$ .

The maximum gain that could be obtained was also studied. Due to lack of power in the 500 GHz BWO sources, it was difficult to see which LO power level would be the optimal for the bias settings that were used. Therefore, this experiment was also performed at 100 GHz where the available LO power was higher. The results are displayed in figure 4.17. Besides the measured gain, there are also two curves showing the gain at lower IF. Based on the gain bandwidth curve in figure 4.16, the gain versus LO power curves at 100 GHz and 500 GHz are corrected by 2.6 dB and 3.8 dB, respectively.

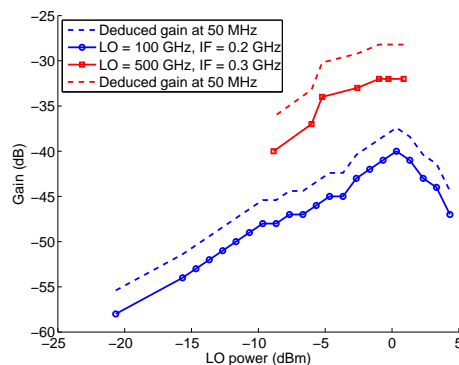


**Figure 4.17:** Gain is plotted as a function of LO power for IFs of 0.2 GHz and 0.3 GHz for LO frequencies 100 GHz and 500 GHz, respectively.

Theoretically the gain is given by equation 2.23, which is repeated here:

$$g = \frac{2I^2 C_0^2 P_{LO} R_L}{(R_L + R_0)^2} \left( 1 - I^2 C_0 \frac{R_L - R_0}{R_L + R_0} \right)^{-2},$$

where  $C_0 = \frac{1}{G} \frac{\partial R}{\partial T}$ . It is seen here that the gain will scale linearly with the LO power. Simultaneously, the gain will also scale with a factor  $I^2 C_0^2 = S_V^2$ . To test this experimentally, the LO power was decreased while the bias current was increased which also increased the responsivity.  $S_V^2 P_{LO}$  is plotted (normalized) in logarithmic scale together with the gain in figure 4.18 where it is clear that the characteristics are the same for both curves.

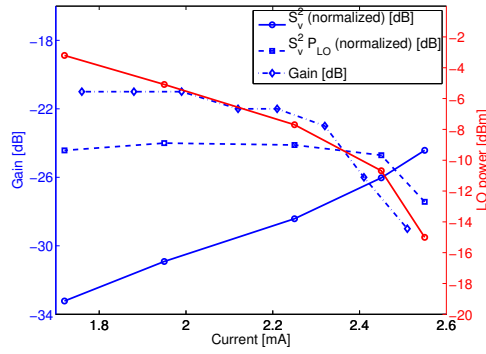


**Figure 4.18:** Plot showing gain as a function of bias current at 20 MHz IF. The LO power, the responsivity squared and responsivity squared times LO power is also plotted in a normalized scale.

### 4.3.2 Room temperature

Mixing was performed at room temperature using sources at 100 GHz, combined using a directional coupler. The LO signal was acquired using a signal generator and an active multiplier which could easily be tuned frequency wise. The RF signal source was a Gunn diode. A schematic illustration of the measurement setup is shown in figure 2.2 and a photograph from the actual experiment is shown in figure 4.19. The bolometers were measured using a constant current bias. The IF readout was done using a frequency analyzer at low IFs and a lock-in amplifier at frequencies  $> 1$  GHz. The reason for doing this was that the signal to noise ratio was too low below 1 GHz to enable the use of the spectrum analyzer.



**Figure 4.19:** Photograph showing the experimental setup for mixing experiments at 100 GHz.

Figure 4.20 shows the mixer signal spectrum for a  $4 \times 1 \mu\text{m}^2$  from batch 5. It was not possible to make a fit by simply applying equation 2.24. Instead a two constant fit was employed where the fit curve is given by

$$g = g_1(0)/(1 + \omega_{\text{IF}}^2 \tau_1^2) + g_2(0)/(1 + \omega_{\text{IF}}^2 \tau_2^2).$$

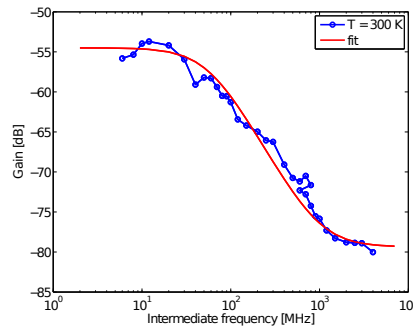


**Figure 4.20:** Plot showing the gain versus IF for a device from batch 5 with dimensions  $4 \times 1 \mu\text{m}^2$ .

The time constants used in this fit are 3 ns and 0.18 ns. Physically, this behavior can be explained by the different cooling mechanisms at low and high IFs. The thermal conductivity at high IFs is determined by the electron

phonon relaxation time whereas at low IFs it will be determined by the thermal boundary resistance [35].

In order to have a safe device operation, the same bias current limiting condition that was used for direct detection (given in equation 4.9) was also used for mixing. In the case of direct detection, the maximum dissipated power was given as  $P_{\text{DC,max}} = I_{\text{max}}U_{\text{max}}$ . This condition is slightly modified for mixing, where the total maximum power is given by  $P_{\text{max}} = P_{\text{DC,max}} + P_{\text{LO,max}}$ . Equation 2.23 states that  $g \propto P_{\text{LO}}P_{\text{DC}}$ . Combining these two conditions gives that the maximum gain is obtained when  $P_{\text{LO,max}} = P_{\text{DC,max}} = 0.5P_{\text{max}}$ . Together with the measured device parameters (thermal conductance, thermal capacitance), this condition was then used to calculate the maximum gain for the different device sizes of batch 5. A summary is found in table 4.3. It is here seen that the gain does not differ significantly when the device sizes are varied between  $2 \times 1$  and  $4 \times 1 \mu\text{m}^2$ .

Size [ $\mu\text{m}^2$ ]	$2 \times 1$	$3 \times 1$	$4 \times 1$
$g_{\text{max}}$ [dB]	-18.6	-16.9	-18.7
$C$ [ $\Omega/\text{mW}$ ]	1.6	1.6	0.4
$I_{\text{max}}$ [mA]	8.2	11.4	18.0
$R_0$ [ $\Omega$ ]	72	58	40
$P_{\text{LO}}$ [mW]	4.8	7.5	13.0

**Table 4.3:** Calculated maximum gain for three different devices from batch 5. Important device and experimental parameters are also given.

The gain versus bias current was measured at 100 GHz for one device, having the size  $3 \times 1 \mu\text{m}^2$ . These results are presented in figure 4.21. The highest measured gain was -28 dB for a bias current of 10 mA and a LO power level of 0.74 mW. This can be compared to the predicted maximum gain of -16.9 for an LO power of 7.5 mW given in table 4.3. Since the power of THz sources are limited it would be desirable to have smaller devices whose LO power requirements are less.

## 4.4 Noise

All noise measurements of the bolometers were performed using a lock-in amplifier with an internal frequency reference. Just as in the direct detection and mixing experiments, the bolometers were biased using constant currents, but without RF signals. As seen in equations 2.26, the total NEP in a bolometer will decrease for smaller sizes because of higher responsivity (see figure 4.14). The thermal noise, being proportional to the thermal conductance (see equation 2.27), will also decrease for smaller bolometers since the thermal conduction is proportional to the device area. One potential noise source at low frequencies is the dc bias current source. To determine how this current source affects the noise it can be replaced with for instance a 9 V battery that could provide better current stability. This was never tested though.

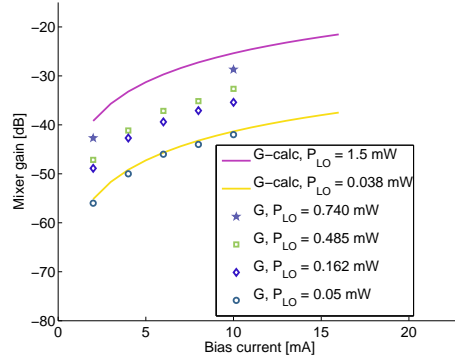


**Figure 4.21:** Measured and calculated gain for a  $3 \times 1 \mu\text{m}^2$  device. The LO frequency was 100 GHz.

#### 4.4.1 Room temperature

A  $4 \times 1 \mu\text{m}^2$  bolometer from batch 5 was measured from 20 Hz to 100 kHz. To determine the noise contribution from the lock-in amplifier itself, the bolometer was replaced by a  $50 \Omega$  resistor which has a voltage noise given by equation 2.25. The results are shown in figure 4.22.

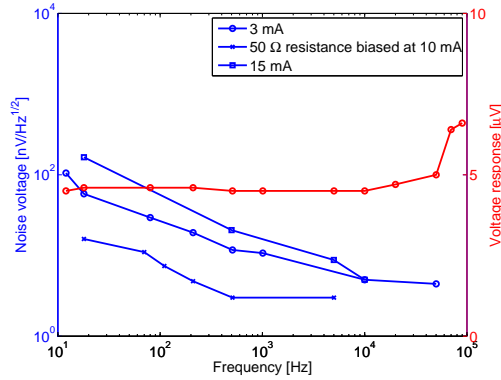


**Figure 4.22:** Total measured noise voltage versus frequency at 1, 3 and 15 mA bias currents for a  $4 \times 1 \mu\text{m}^2$  bolometer from batch 5. The noise voltage of a  $50 \Omega$  resistor is measured at 10 mA. Also shown is the voltage response from the bolometer versus frequency. All measurement were done at room temperature.

At higher frequencies, the lock-in amplifier noise becomes more pronounced. It dominates at and above 500 Hz, where the over all noise decreases but the lock-in amplifier noise stays constant. The noise measured for the whole system was about  $5\text{-}6 \text{ nV/Hz}^{1/2}$  for frequencies above 5 kHz. Simultaneously, the lock-in amplifier contributed to the total noise with  $3\text{-}4 \text{ nV/Hz}^{1/2}$ , which is obtained from the data in figure 4.22 and the Johnson noise from the  $50 \Omega$  resistor ( $0.9 \text{ nV/Hz}^{1/2}$  according to equation 2.26). Therefore, the projected NEP at room

temperature for a 15 mA bias current is estimated by

$$\text{NEP}_{\text{RT}} = \frac{((6 \text{ nV/Hz}^{1/2})^2 - (4 \text{ nV/Hz}^{1/2})^2)^{1/2}}{10 \text{ V/W}} = 450 \text{ pW/Hz}^{1/2},$$

where the responsivity 10 V/W have been used (see table 4.22).

#### 4.4.2 Superconducting state

As seen in figure 4.23, for temperatures near  $T_c$  the low frequency noise decreases. The noise voltage is constant at about 3 nV/Hz<sup>1/2</sup> from 77 to 81 K and 1 kHz frequency. Changing the frequency from 1 kHz and up to 100 kHz did not affect the noise. At low frequencies, i.e. around and less than 200 Hz, the bolometer's contribution to noise dominates. The NEP at 77 K was calculated to be 110 pW/Hz<sup>1/2</sup> at 18 Hz and 20 pW/Hz<sup>1/2</sup> at 1 kHz.

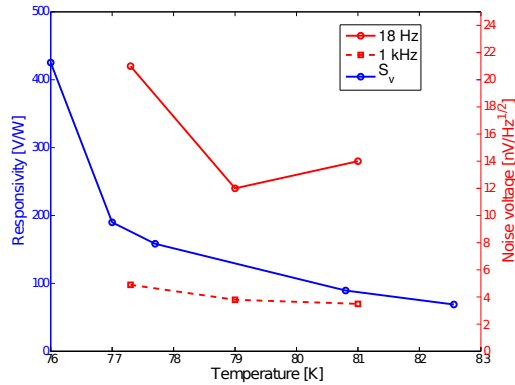


**Figure 4.23:** Noise voltage versus temperature for 18 Hz and 1 kHz. The tested bolometer had a size of  $2 \times 1 \mu\text{m}^2$ .

## Chapter 5

# Conclusions and future outlook

It has been shown in this thesis that antenna integrated bolometers, with sizes around  $1\ \mu\text{m}$ , based on thin films of YBCO can be fairly easily fabricated using standard cleanroom processing techniques, such as pulsed laser deposition, UV photolithography, Ar ion milling and thin film metal deposition. Some difficulties were encountered during the fabrication, but it is believed that these can, and have been, overcome. The bolometers have proved to be very versatile with good performance as both direct detection and heterodyne mixers at 77 K and room temperatures.

As direct detectors, responsivities of about 450 V/W at 76 K have been measured. The power reference plane was outside the cryostat in this case. The highest responsivity measured at room temperature is 15 V/W with the absorbed power taken as the reference. It has been showed that the responsivity will increase significantly for smaller bolometers.

When used as mixers, a gain of -24 dB and -28 dB have been obtained at 77 K and room temperature, respectively. Just as for the responsivity, the gain will also increase for smaller bolometers whereas the LO power requirements decrease.

The response time has been measured to be about 300 ps at 77 K and 2 ns at room temperature. Making the YBCO films thinner will decrease the response time, or equivalently increase the IF bandwidth.

A NEP of  $20\ \text{pW}/\text{Hz}^{1/2}$  was measured at 77 K and 1 kHz. The corresponding number for room temperature was  $450\ \text{pW}/\text{Hz}^{1/2}$ .

As mentioned above, making smaller bolometers will imply over all improved performance. A future cleanroom process involving electron beam lithography to make bolometers with sizes less than  $1\ \mu\text{m}$  is discussed in the thesis. Practical problems with discharges is during the exposure have to be solved.

It can also be of interest to deposit the YBCO film on some alternative substrate, such as MgO. By doing this, it will be possible to investigate how the effect of birefringence in sapphire influences the performance.

The thermal conductance has been proven to scale with the bolometer area. However, it is also dependent of the interface between the substrate and the YBCO film and it can therefore be good to have some insight in how it will depend on the CeO<sub>2</sub> buffer layer thickness.

Lastly, it would be of great interest to fabricate a multi-pixel receiver based on YBCO bolometers in arrays. Having such a receiver would enable real time imaging in the THz regime. To do this, a stable process has to be established and practical problems, as having a multiple readout and coupling a LO source to all bolometers, have to be solved. However, since the bolometers have proven to be both sensitive and fast, the prospects for imaging are good.

# Acknowledgements

First, I would like to thank my supervisor Sergey Cherednichenko who proposed this project and guided me through it at all times. His patience and will to teach has been invaluable for my understanding of THz detectors and the field of THz technology. He also deserves extra credits for the help he provided with all device measurements. I would also like to express my gratitude to Vladimir Drakinskiy who introduced me to almost all cleanroom equipment that was used for the bolometer fabrication. The many discussions we had were very important to solve the problems that were encountered. I am also thankful to Stella Bevilacqua. Our collaboration in the beginning of the project was very valuable when we both were new on the subject. I am also thankful to Alexey Kalabukhov for all help with thin film deposition of YBCO. My gratitude also goes to Shahid Nawaz who helped me with YBCO deposition on MgO substrates. Last, but not least, I would like to thank all of the staff at the Terahertz and Millimetre Wave Laboratory at Chalmers. There was always someone to ask and willing to help whenever problems were encountered. The good spirit in this group really helps to form a creative and pleasant working environment.



# References

- [1] P. Siegel, “Terahertz technology,” *Microwave Theory and Techniques, IEEE Transactions on*, vol. 50, no. 3, pp. 910–928, mar 2002.
- [2] M.-A. Brun, F. Formanek, A. Yasuda, M. Sekine, N. Ando, and E. Y., “Contrast improvement of terahertz images of thin histopathologic sections,” *Biomedical Optics Express*, vol. 2, no. 1, p. 58, 2011.
- [3] H. Quast and T. Loffler, “Towards real-time active thz range imaging for security applications,” in *Electromagnetics in Advanced Applications, 2009. ICEAA '09. International Conference on*, sept. 2009, pp. 501–504.
- [4] M. Griffin, G. Pilbratt, T. de Graauw, and A. Poglitsch, “The herschel space observatory,” in *Infrared, Millimeter and Terahertz Waves, 2008. IRMMW-THz 2008. 33rd International Conference on*, sept. 2008, pp. 1–2.
- [5] T. Wilson, “The atacama large millimeter array,” in *Infrared and Millimeter Waves, 2007 and the 2007 15th International Conference on Terahertz Electronics. IRMMW-THz. Joint 32nd International Conference on*, sept. 2007, pp. 591–593.
- [6] (2011, May) Overview of SOFIA. [Online]. Available: <http://www.sofia.usra.edu/Science/overview/index.html>
- [7] S. Cherednichenko, V. Drakinskiy, T. Berg, P. Khosropanah, and E. Kollberg, “Hot-electron bolometer terahertz mixers for the herschel space observatory,” *Review of Scientific Instruments*, vol. 79, no. 3, pp. 034501–034501–10, mar 2008.
- [8] F. Sizov, “Thz radiation sensors,” *Opto-Electronics Review*, vol. 18, pp. 10–36, 2010, 10.2478/s11772-009-0029-4. [Online]. Available: <http://dx.doi.org/10.2478/s11772-009-0029-4>
- [9] L. Liu, J. Hesler, H. Xu, A. Lichtenberger, and R. Weikle, “A broadband quasi-optical terahertz detector utilizing a zero bias schottky diode,” *Microwave and Wireless Components Letters, IEEE*, vol. 20, no. 9, pp. 504–506, sept. 2010.
- [10] B. Karasik, M. Gaidis, W. McGrath, B. Bumble, and H. LeDuc, “A low-noise 2.5 thz superconductive nb hot-electron mixer,” *Applied Superconductivity, IEEE Transactions on*, vol. 7, no. 2, pp. 3580–3583, jun 1997.

- [11] S. Cherednichenko, V. Drakinskiy, K. Ueda, and M. Naito, "Terahertz mixing in MgB<sub>2</sub> microbolometers," *Applied Physics Letters*, vol. 90, no. 2, pp. 023 507 –023 507–3, jan 2007.
- [12] (2011, May) Ricor Cryogenic & Vacuum Systems - Miniature cryocoolers. [Online]. Available: <http://ricor.com/Index.asp?CategoryID=59>
- [13] P. Richards, "Bolometers for Infrared and Millimeter Waves," *Journal of Applied Physics*, vol. 76, no. 1, pp. 1–24, JUL 1 1994.
- [14] M. Nahum, S. Verghese, P. L. Richards, and K. Char, "Thermal boundary resistance for YBa<sub>2</sub>Cu<sub>3</sub>O<sub>7-δ</sub> films," *Applied Physics Letters*, vol. 59, no. 16, pp. 2034 –2036, oct 1991.
- [15] F. Arams, C. Allen, B. Peyton, and E. Sard, "Millimeter mixing and detection in bulk insb," *Proceedings of the IEEE*, vol. 54, no. 4, pp. 612 – 622, april 1966.
- [16] R. E. Collin, *Foundations for Microwave Engineering*, 2nd ed. Wiley-Interscience, 2001.
- [17] Rönning, Fredrik, "Heterodyne Mixers Based on YBa<sub>2</sub>Cu<sub>3</sub>O<sub>7-δ</sub> Thin Films," Ph.D. dissertation, Chalmers Universtiy of Technology, 2003.
- [18] M. Tinkham, *Introduction to Superconductivity*. Dover Publications, 2004.
- [19] J. Bardeen, L. N. Cooper, and J. R. Schrieffer, "Microscopic theory of superconductivity," *Phys. Rev.*, vol. 106, no. 1, pp. 162–164, Apr 1957.
- [20] M. K. Wu, J. R. Ashburn, C. J. Torng, P. H. Hor, R. L. Meng, L. Gao, Z. J. Huang, Y. Q. Wang, and C. W. Chu, "Superconductivity at 93 K in a new mixed-phase Y-Ba-Cu-O compound system at ambient pressure," *Phys. Rev. Lett.*, vol. 58, no. 9, pp. 908–910, Mar 1987.
- [21] J. Rossat-Mignod, L. P. Regnault, C. Vettier, P. Burlet, J. Y. Henry, and G. Lapertot, "Investigation of the spin dynamics in YBa<sub>2</sub>Cu<sub>3</sub>O<sub>6+x</sub> by inelastic neutron scattering," *Physica B: Condensed Matter*, vol. 169, no. 1-4, pp. 58 – 65, 1991.
- [22] C.-T. Li, B. S. Deaver, M. Lee, R. M. Weikle, R. A. Rao, and C. B. Eom, "Low power submillimeter-wave mixing and responsivity properties of YBa<sub>2</sub>Cu<sub>3</sub>O<sub>7</sub> hot-electron bolometers," *Applied Physics Letters*, vol. 71, no. 11, pp. 1558 –1560, sep 1997.
- [23] P. Larsson, B. Nilsson, and Z. G. Ivanov, "Fabrication and transport measurements of YBa<sub>2</sub>Cu<sub>3</sub>O<sub>7-x</sub> nanostructures," *Journal of Vacuum Science Technology B: Microelectronics and Nanometer Structures*, vol. 18, no. 1, pp. 25 –31, jan 2000.
- [24] Hecht, Eugene, *Optics*, 4th ed., 2002.
- [25] D. Rutledge and M. Muha, "Imaging antenna arrays," *Antennas and Propagation, IEEE Transactions on*, vol. 30, no. 4, pp. 535 – 540, jul 1982.

- [26] Balanis, Constantine A., *Antenna Theory - Analysis and Design*, 3rd ed., 2005.
- [27] A. D. Semenov, H. Richter, H.-W. Hubers, B. Gunther, A. Smirnov, K. S. Il'in, M. Siegel, and J. P. Karamarkovic, "Terahertz performance of integrated lens antennas with a hot-electron bolometer," *Microwave Theory and Techniques, IEEE Transactions on*, vol. 55, no. 2, pp. 239–247, feb. 2007.
- [28] Ganzevles, Walter, "A Quasi-Optical THz Mizer Based on a Nb Diffusion-Cooled Hot-Electron-Bolometer," Ph.D. dissertation, Delft University of Technology, 2002.
- [29] Kroug, Matthias, "Heterodyne Mixers Based on  $\text{YBa}_2\text{Cu}_3\text{O}_{7-\delta}$  Thin Films," Ph.D. dissertation, Chalmers University of Technology, 2001.
- [30] (2011, May) Single crystal sapphire. [Online]. Available: <http://global.kyocera.com/prdct/fc/product/pdf/s.c.sapphire.pdf>
- [31] J. Krupka, K. Derzakowski, M. Tobar, J. Hartnett, R. G. Geyer, "Complex Permittivity of Some Ultralow Loss Dielectric Crystals at Cryogenic Temperatures," *Measurement Science and Technology*, vol. 10, pp. 387–392, 1999.
- [32] Goldsmith, Paul F., *Quasioptical Systems - Gaussian Beam Quasioptical Propagation and Applications*, 1998.
- [33] P. Khosropanah, "Modeling hot electron bolometer thz mixers," Licentiate thesis, Chalmers University of Technology, Oct. 2000.
- [34] (2011, May) Solve boundary value problems for ordinary differential equations - matlab. [Online]. Available: <http://www.mathworks.com/help/techdoc/ref/bvp4c.html>
- [35] V. A. Trifonov, B. S. Karasik, M. A. Zorin, G. N. Goltsman, E. M. Gershenson, M. Lindgren, M. Danerud, and D. Winkler, "9.6  $\mu\text{m}$  wavelength mixing in a patterned  $\text{YBa}_2\text{Cu}_3\text{O}_{7-\delta}$  thin film," *Applied Physics Letters*, vol. 68, no. 10, pp. 1418–1420, mar 1996.



# Appendix A

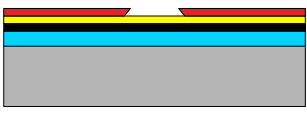
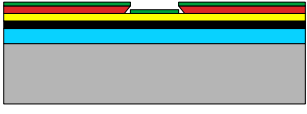
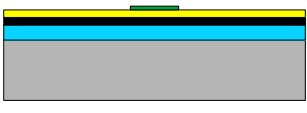
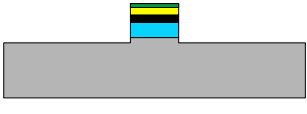
## Processing steps

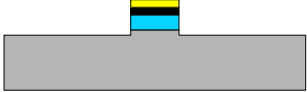
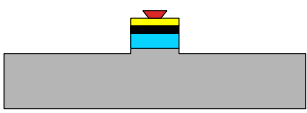
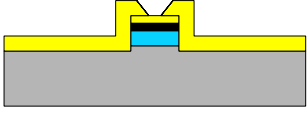
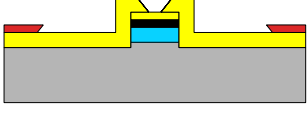
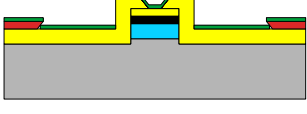
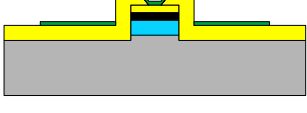
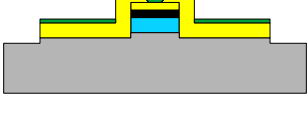
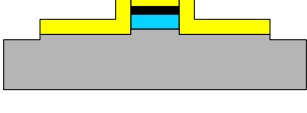
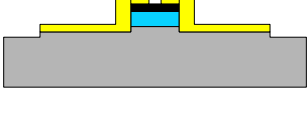
The fabrication of the bolometers is described here as a step-by-step manual where a cross section side view of a bolometer is showed for all steps. A chart explaining the meaning of different colors for these pictures is given in the table below. It should be added that all pictures are out of scale and only give schematic description of what was done. All used tools, detailed recipes and important tool parameters are given in appendix B and C, respectively. The tool numbers correspond to MC2's labelling, see <http://labbokning.mc2.chalmers.se/>

Material	Color
$\text{Al}_2\text{O}_3$	
$\text{CeO}_2$	
YBCO	
Au	
resist	
C	

**Description**

1. This step applies to both kinds of substrates used, i.e.  $\text{Al}_2\text{O}_3$  and  $\text{MgO}$ .
2. The recipe used to sputter  $\text{CeO}_2$  was the same for all batches. Note that this step is not used when YBCO is deposited on  $\text{MgO}$ .
3. It is important to measure the energy in laser as accurate as possible. The pulse energy after the last lens (before being transmitted into the chamber) should be 84 mJ.
4. The thickness of the in-situ sputtered Au layer was 20 nm in most cases. 40 nm was once tested when troubleshooting, but it made no difference to the results, i.e. 20 nm and 40 nm seem to protect the YBCO equally well.
5. Image reversal photolithography is used to pattern a small "island", which will later make up the bolometer bridge. Note that this island is much bigger than the actual bolometer, which is formed simultaneously with the antenna using ion milling (step 15).
6. -
7. -
8. The island is defined.
9. -
10. This step defines the actual bolometer length. To resolve sizes  $< 1 \mu\text{m}$ , it was sometimes necessary to develop for as much as 50 s instead of 30 s. However, this made the lift-off more difficult.
11. The whole  $10 \times 10$  substrate gets covered with Au and only small "windows" defining the bolometers and the alignment marks are visible after lift-off.
12. Photolithography to define the antenna pattern. Once again, it was sometimes necessary to increase the developing time to resolve small sizes.
13. -
14. -
15. The antennas are defined.
16. -
17. The whole sample is etched for about 2 min to remove the in-situ Au. Note that no protective mask of carbon or other material is used.

Process	Recipe	Tool	Comments	Side view
1. Surface cleaning	B.1.1	-	-	
2. CeO <sub>2</sub> sputtering	B.1.2	1143, C	30-40 nm	
3. YBCO deposition	B.1.3	1142,C	50 nm	
4. Au sputtering	-	1144, C	20 nm	
5. Photolithography	B.1.4	213, C	image reversal	
6. C deposition	B.1.6	11413, C	60-70 nm	
7. Lift-off	B.1.6	-	-	
8. Ion milling	B.1.7	417, C	-	

9. C mask removal	B.1.6	419, C	60-70 nm	
10. Photolithography	B.1.4	213, C	image reversal	
11. Au evaporation	B.1.8	C	350 nm	
12. Photolithography	B.1.4	213, C	image reversal	
13. C deposition	B.1.6	11413, C	60-70 nm	
14. Lift-off	B.1.6	-	-	
15. Ion milling	B.1.7	417, C	-	
16. C mask removal	B.1.6	419, C	60-70 nm	
17. Ion milling	B.1.7	417, C	-	

# Appendix B

## Processing recipes

The purpose of this appendix is to give a complete processing recipe description to enable future development.

### B.1 Recipes and tool settings

#### B.1.1 Substrate cleaning prior to PLD

put substrate in 60° C Acetone for 5 min and rub with cotton stick  
while in acetone, put the sample in ultrasonic bath for 5 min  
transfer the substrate to 60° C methanol for 5 min and rub with cotton stick  
while in methanol, put the sample in ultrasonic bath for 5 min  
transfer the substrate to 60° C isopropanol  
while in isopropanol, put the sample in ultrasonic bath for 5 min  
blow dry using N<sub>2</sub> gas

#### B.1.2 CeO<sub>2</sub> sputtering

Complete process, written in the system's syntax:

```
Total Time: 1885.0
Open 1CM
Set Manipulator Position H1
Pause 10.0
Wait Until User continues / Turbo standby on-heater power supply on?
Set Pressure Control Mode Upstream
Set Pressure Control Setpoint [mbar] 0.1
Set Pressure Control O2 Flow 25.00
Set Pressure Control Ar Flow 100.00
Open O2 CeO2
Open Ar CeO2
Set Pressure Control Regulation ON
Wait Until Pressure CM [mbar] > 0.09
Set Manipulator Ramp Rate 10.0
Set Manipulator Setpoint 100.0
```

```
Wait Until Manipulator Temperature > 100.0
Set Manipulator Ramp Rate 50.0
Set Manipulator Setpoint 750.0
Wait Until Manipulator Temperature > 749.0
Pause 60.0
Wait Until User continues /Ready for presputtering?
Open CeO2
Set CeO2 RF-Control
Set CeO2 RF-Regulation Power
Set CeO2 Forward Power 50
Start CeO2
Wait Until CeO2 Forward Power > 48
Wait Until CeO2 Reflected Power < 5.0
Pause 600.0
Close CeO2
Wait Until User continues / going to set dep.pressure
Set Manipulator Position H3
Wait Until User continues / Heater position ok?
Open CeO2
Pause 1200.0
Stop CeO2
Close CeO2
Set Pressure Control Regulation OFF
Close O2 CeO2
Close Ar CeO2
Set Pressure Control O2 Flow 0.00
Set Pressure Control Ar Flow 0.00
Pause 5.0
Close Gate Valve
Close 1CM
Pause 5.0
Start Backfilling
Wait Until Pressure Convectron [Torr] > 500.000
Stop Backfilling
Set Manipulator Ramp Rate 10.0
Set Manipulator Setpoint 0.0
Wait Until Manipulator Temperature < 50.0
Open Roughing Valve
Wait Until Pressure Convectron [Torr] < 0.100
Close Roughing Valve
Pause 5.0
Reset Alarm
Open Gate Valve
Set Manipulator Position HL
End
```

### B.1.3 YBCO deposition using PLD

Before running the automatic process, the laser pulse energy was measured prior to the PLD chamber. The laser voltage was manually adjusted, so that

the pulse energy was 84 mJ<sup>1</sup>, and entered in the process file.

Complete process, written in the system's syntax:

```
Total Time: 3640.0
Open 1CM
Set Pressure Control Setpoint [mbar] 0.600
Close Gate Valve
Pause 10.0
Set Pressure Control Mode Downstream
Set Pressure Control O2 Flow 50.000
Open O2
Wait Until Pressure CM [mbar] > 0.590
Set Manipulator RPM 2
Set Manipulator Ramp Rate 10.0
Set Manipulator Setpoint 200.0
Wait Until Manipulator Temperature > 199.0
Set Manipulator Setpoint 830.0
Set Manipulator Ramp Rate 50.0
Wait Until Manipulator Temperature > 829.0
Wait Until User continues
Start Manipulator Rotation
Set Target YBCO
Set Target RPM 20
Set Target Frequency 0.20
Start Target Sweep
Start Target Rotation
Set Manipulator Motion Scan 29.50; 34.50; 10.50; 15.50; 4.00; 4.00; 10; 10
Start Manipulator Motion
Set Laser Mode HV
Set Laser HV 25.5
Set Laser Pulse Rate 10.0
Open Targetshutter
Wait Until User continues / Ready to start deposition?
Start Laser
Wait Until Laser Counter > 1000
Stop Laser
Pause 10.0
Stop Target Sweep
Stop Target Rotation
Stop Manipulator Rotation
Stop Manipulator Motion
Close O2
Close 1CM
Close Gate Valve
Pause 10.0
Wait Until User continues / Backfill manually to 6,5E2 Torr
```

---

<sup>1</sup>The glass window to the PLD chamber was replaced after the fabrication for this thesis was completed. This should change the pulse energy calibration from 82-84 mJ/pulse to about 65 mJ/pulse, according to the tool responsible for the PLD system.

```

Set Target MgO
Close Targetshutter
Set Manipulator Ramp Rate 10.0
Set Manipulator Setpoint 550.0
Wait Until Manipulator Temperature < 551.0
Pause 3600.0
Set Manipulator Ramp Rate 40.0
Set Manipulator Setpoint 0.0
Wait Until Manipulator Temperature < 50.0
Wait Until User continues
Open Roughing Valve
Wait Until User continues / Pressure Convectron [Torr] < .6,0E-2?
Close Roughing Valve
Reset Alarm
Open Gate Valve
Pause 10.0

```

#### B.1.4 Image reversal photolithography, resist: AZ 5214E

cleaning: 60° C acetone 3 min, 60° C isopropanol 3 min, N<sub>2</sub> blow dry  
 spin resist: HDMS primer + resist, 4000 rmp, 30 s each  
 bake: 60 s, 110°  
 edge bead exposure: 20 s, 6 mW/cm<sup>2</sup>  
 develop: 60 s in AZ351B and water 1:5, water rinse, N<sub>2</sub> blow dry  
 pattern exposure: 6 s, 6 mW/cm<sup>2</sup>  
 reversal bake: hot plate 60 s, 125° C  
 flood exposure: 60 s, 6 mW/cm<sup>2</sup>  
 develop: 30-50 s in AZ351B and water 1:5, water rinse, N<sub>2</sub> blow dry  
 descum: RIE O<sub>2</sub>, 20 sccm, 90 W, 100 mTorr, 20 s

#### B.1.5 Positive photolithography, resist: AZ 1512HS

cleaning: 60° acetone 3 min, 60° isopropanol 3 min, N<sub>2</sub> dry  
 spin resist: HDMS primer + resist, 4000 rpm, 30 s (1.3 μm)  
 bake: hot plate 60 s, 100° C  
 edge bead exposure: 30 s at 6 mW/cm<sup>2</sup> develop: 30 s in AZ351B and water (1:5), water rinse, N<sub>2</sub> blow dry  
 pattern exposure: 9 s at 6 mW/cm<sup>2</sup>  
 develop: 20 s in AZ351B and water (1:5), water rinse, N<sub>2</sub> blow dry  
 descum: RIE O<sub>2</sub>, 20 sccm, 90 W, 100 mTorr, 20 s  
 dry etch hard bake: oven 30 min, 120 deg C (optional, only used when used for protection in ion milling)

#### B.1.6 Carbon mask deposition using PLD

pump the pressure to  $P < 5 \cdot 10^{-6}$  mbar  
 turn on Ar gas flow so that  $P = 3 \cdot 10^{-4}$  mbar  
 run laser at  $\sim 105$  mJ/pulse at 10 Hz  
 wait 5 min (3000 pulses)

lift carbon mask in room tempered acetone using ultrasound (60% power, degas mode)  
remove carbon mask using O<sub>2</sub> plasma, 50 W at 10 min

### **B.1.7 Ar ion milling**

glue substrate to chuck using 1512 HS resist. bake resist for 10 min at 100° C.  
pump to base pressure,  $\sim 2 \cdot 10^{-7}$  mbar  
beam current: 13 mA  
beam voltage: 250 V  
Ar flow: 2 ccm  
process for 5 min, close shutter for 5 min to cool and repeat.  
etching rate for Au: 10.5 - 11 nm/min  
etching rate for YBCO: 3.5 nm/min

### **B.1.8 Au evaporation**

pump for 1 hour  
deposit 5 nm Ti  
deposit Au  
lift-off using acetone at room temperature



# Appendix C

## Equipment lists

### Processing tools

1143: DCA - MTD 450, Oxide sputter  
1142: DCA - UHV PLD, Pulsed Laser Deposition - DCA UHV  
1144: DCA - MTD 450, Sputter - DCA Metal  
213: Suss MicroTec - MA6, Mask aligner - KS MA/BA 6, #2  
11413: Chalmers, Pulsed Laser Deposition - Carbon System  
417: Oxford Plasma Technology - Ionfab 300, Ion Beam Milling System  
-CAIBE Oxford Ionfab  
420: AVAC - HVC600, Evaporator - AVAC HVC600  
419: Plasmatherm - BatchTop m/95, Plasma etch- Plasma Therm BatchTop  
PE/RIE m/95

### Measuring instruments

Keithley 2000 Multimeters  
LakeShore 332 Temperature controller  
Stanford Research Systems - SR830 DSP Lock-In Amplifier  
Yokogama 7651 DC source  
Tektronix 2754 Spectrum analyzer  
ZAX ZMT - 10/20/93.25/13.5 Gunn oscillator  
Low noise amplifiers 0.1-20 GHz



## Appendix D

# Publications

This section contains papers and conference contributions that have been presented during the spring of 2011:

- Sergey Cherednichenko, Arvid Hammar, Stella Bevilacqua, Vladimir Drakinskiy, Jan Stake and Alexey Kalabukhov, "A room temperature bolometer for terahertz coherent and incoherent detection", *IEEE Terahertz Science and Technology*, paper accepted in May 2011.
- Arvid Hammar, Sergey Cherednichenko, Stella Bevilacqua, Vladimir Drakinskiy, and Jan Stake, "Terahertz direct detection in  $\text{YBa}_2\text{Cu}_3\text{O}_7$  microbolometers", *IEEE Terahertz Science and Technology*, paper submitted in April 2011.
- Arvid Hammar, Sergey Cherednichenko, Vladimir Drakinskiy, Stella Bevilacqua and Jan Stake, "Terahertz Direct Detection in  $\text{YBa}_2\text{Cu}_3\text{O}_7$  Bolometers for Applications at Cryogenic and Room Temperatures", *22<sup>nd</sup> International Symposium on Space Terahertz Technology (ISSTT)*, Tucson, Arizona, USA, poster presentation held in April 2011
- Arvid Hammar, Sergey Cherednichenko, Vladimir Drakinskiy, Stella Bevilacqua and Jan Stake, "Terahertz Mixing in  $\text{YBa}_2\text{Cu}_3\text{O}_7$  Bolometers for Applications at Cryogenic and Room Temperatures", *22<sup>nd</sup> International Symposium on Space Terahertz Technology (ISSTT)*, Tucson, Arizona, USA, poster presentation held in April 2011
- Sergey Cherednichenko, Arvid Hammar, Stella Bevilacqua, Vladimir Drakinskiy and Jan Stake, "Wideband THz detectors based on YBCO thin films at 77 K and at room temperature", *6<sup>th</sup> ESA Workshop on Millimetre-Wave Technology and Applications, MilliLab, Espoo, Finland*, oral presentation held in May 2011

# A room temperature bolometer for terahertz coherent and incoherent detection

Sergey Cherednichenko, Arvid Hammar, Stella Bevilacqua, Vladimir Drakinskiy, Jan Stake, *Senior Member, IEEE*, and Alexey Kalabukhov

**Abstract**—We present a novel room temperature bolometer with nanosecond response that can be used both for coherent and incoherent detection through the entire terahertz frequency range. A responsivity of up to 15 V/W, and a noise equivalent power (NEP)  $\sim 450$  pW/Hz were measured at modulation frequencies from 0.5 kHz to 100 kHz. A conversion gain of -28 dB was demonstrated at an intermediate frequency of 20 MHz with a Local Oscillator power of 0.74 mW. Possible improvements of the bolometer characteristics are discussed.

**Index Terms**—Bolometer, mixer, terahertz (THz), submillimeter, YBCO.

## I. INTRODUCTION

THz waves (300 GHz-10 THz) have a wide area of applications, e.g. security and medical imaging, gas and solids spectroscopy, communication, etc [1,2]. The progress in those areas depends on the availability of the key components: detectors, sources, filters, etc. A great progress in electro-optical THz wave generation/detection has led to a breakthrough in the development of pulsed THz systems. For example, THz time domain spectrometers offer a wide frequency coverage, which is a valuable feature for spectroscopy of solids and large molecules (e.g. DNA) [3,4].

Continuous wave (CW) systems have been extensively used in radio astronomy, where many cryogenic detectors have been developed, offering a high power sensitivity [5]. Apart from radio astronomy, where sensitivity is the main drive for the choice of a detector, many other applications are critically dependent on compact, non cryogenic (or moderately cooled) THz detectors. Currently, such detectors are limited to Schottky diodes that are the most sensitive room temperature detectors practically available today for frequencies up to at least 1THz [6]. Schottky diodes are used both for coherent and direct detection. As an alternative, tunnel diodes have shown a high responsivity in the millimeter wave range, although they have not been extended to the THz range yet [7].

Room temperature bolometers are widely used in IR cameras. They are primarily based on VOx films that are thermally isolated on a thin membrane. With an adapted optics, such cameras have also been shown to operate at 4.3THz [8]. The discussed bolometers are known to be slow, with a typical response time of several ms [9]. Moreover, at

frequencies lower than 4 THz, antenna integrated bolometers would be required, because the radiation wavelength becomes much greater than the bolometer patch size ( $\sim 40$   $\mu\text{m}$ ). Using an air-bridge approach, a microsecond response time was reported for Nb antenna coupled bolometers [10].

Recently, we reported on fast antenna coupled superconducting bolometers, which are based on high-temperature superconducting films of YBa<sub>2</sub>Cu<sub>3</sub>O<sub>7</sub>. At a 77K operation temperature, they achieve a NEP of  $\sim 20$  pW/Hz and a voltage responsivity of  $\sim 190$  V/W in a frequency range of 0.3-1.6THz [11]. The response time was approximately 1ns.

In this paper we demonstrate that using a similar antenna-integrated YBCO bolometer, a ns-response time and a high sensitivity are feasible at room temperature operation. The bolometers are placed on a bulk substrate, and, therefore, they are very robust. In fact, bolometer operation temperature is not critical for the device performance. We investigate these devices both as a direct detectors as well as mixers.

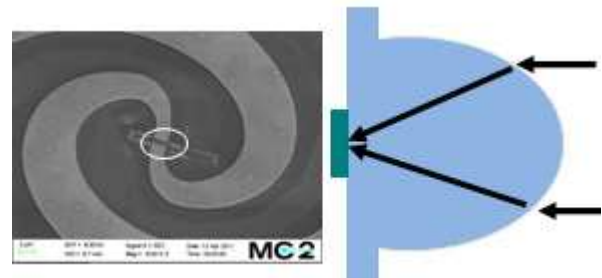


Fig. 1. A quasi-optical THz bolometer is integrated with a spiral antenna on a sapphire substrate. The bolometer chip is glued to a Si lens.

## II. DEVICE FABRICATION

Bolometers were fabricated using a 50-nm-thick YBCO film. The film was made on a sapphire substrate with a CeO<sub>2</sub> buffer layer using pulsed laser deposition. The critical temperature of the YBCO film is about 88 K. A large Temperature Coefficient of Resistance (TCR) in the normal state ( $T > 88\text{K}$ ) was our prime interest. The YBCO film was patterned as a microbridge to overlap with the antenna made of 350 nm thick gold film via UV photolithography (see Fig. 1). The bolometer area between antenna pads was (the width,  $w$ , times the length,  $l$ )  $2 \mu\text{m} \times 1 \mu\text{m}$ ,  $3 \mu\text{m} \times 1 \mu\text{m}$ , and  $4 \mu\text{m} \times 1 \mu\text{m}$ . The choice of a logarithmic spiral antenna was motivated by its real impedance of  $90 \Omega$  in a wide frequency range [12]. A scanning electron microscope image of a bolometer between antenna terminals is shown in

Manuscript received April 4, 2011. This work was supported the Swedish Research Council (VR) and the Swedish National Space Board.

The authors are with Chalmers University of Technology, Department of Microtechnology and Nanoscience, SE-412 96, Göteborg, Sweden (corresponding author phone: +46-31-7728499; fax: +46-31-164513; e-mail: sergei@chalmers.se).

Fig.2. After the fabrication, the substrate was diced for single bolometer chips. The chips were clamped to the backside of a 12-mm elliptical silicon lens, forming a quasioptical THz detector. In the detector block, the readout was arranged via a coaxial waveguide and a bias-T.

The resistance versus temperature for the bolometers is shown in Fig.3.

### III. EXPERIMENTAL TECHNIQUE

For the responsivity measurements, amplitude modulated signal sources at 100 GHz (a Gunn diode oscillator) and 330 GHz (a Backward Wave Oscillator) were used. The sources were equipped with horn antennas. A Teflon lens focused the beam on the Si lens/bolometer. The optical coupling efficiency to the spiral antenna bolometers on a silicon lens has been discussed in [11]: ~4-5dB, that accounted for the Si lens reflection losses, polarization losses, and beam coupling losses. In this paper, THz power, absorbed in the bolometer, was used for the responsivity calculation. The absorbed power was obtained using the isothermal technique [13]. We also verified this method using a 1GHz signal, which was fed into the bolometer via a coaxial cable, i.e. no optical losses were present. In this case, the absorbed power (from the isothermal technique) corresponded very well to the output power of the signal generator.

The bolometers were biased with a constant current. Both the voltage response to the THz signal and the bolometer noise voltage (THz signal blocked) were measured using a lock-in amplifier.

The mixer conversion gain was measured at 90 GHz, using a second 90 GHz source (an active multiplier) as a Local Oscillator (LO). A low noise amplifier (100 K input noise temperature) amplified the IF signal before it was measured using a spectrum analyzer. The LO power was estimated in the same method as the power of the signal source.

### IV. BOLOMETRIC DETECTOR

#### A. Direct detector

At modulation frequencies  $\omega \ll 1/\tau$ , where  $\tau$  is the bolometer response time, the voltage responsivity of the bolometer to an amplitude modulated RF signal can be obtained from a system of two thermal balance equations:

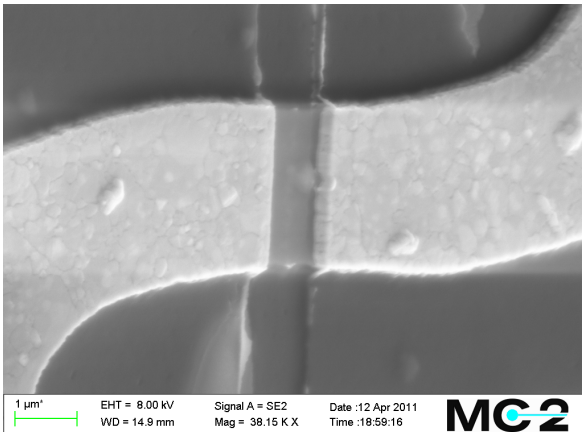


Fig. 2. SEM image of a bolometer at the center of the spiral antenna.

$$G \cdot \Delta T_1 = i^2 \cdot R_1 \quad (1a)$$

$$G \cdot \Delta T_2 = i^2 \cdot R_2 + P_{RF} \quad (1b)$$

where  $G$  is the thermal conductance from the bolometer to the heat sink (the substrates and the contact pads),  $\Delta T_{1,2}$  are the bolometer temperature rise (relative to the substrate temperature) with and without the RF power,  $i$  is the dc bias current,  $R_{1,2}$  are the bolometer dc resistance with and without the RF power,  $P_{RF}$  is the RF power absorbed in the bolometer. Equations (1a) and (1b) represent thermal balance with and without applied RF power.

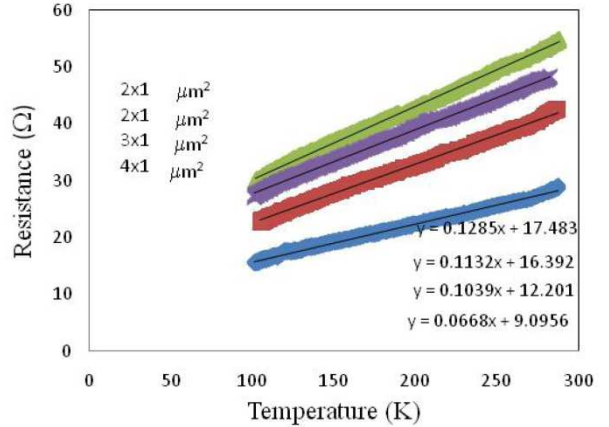


Fig. 3. Resistance versus temperature for 4x1um, 3x1um, and 2x1um bolometers. Equations of the fitting lines are given in the legend.

The bolometer is assumed to be constant current biased. The voltage responsivity is defined as a ratio of the bolometer voltage swing to the absorbed RF power [14]:

$$R_V = \frac{i \cdot \alpha \cdot R}{G - i^2 \cdot \alpha \cdot R} \quad (2)$$

where  $\alpha \equiv \partial R / \partial T \cdot 1/R$  is the TCR. As it follows from Fig.3, in the temperature range from 100K to 300K  $\alpha \times R$  is temperature independent. However,  $\alpha \times R$  is larger for higher resistance devices. On contrary,  $\alpha$  is approximately constant for all devices discussed here. At modulation frequencies that exceed  $1/\tau$ , the responsivity reduces as  $1/(1 + \omega^2 \tau^2)^{0.5}$  [14].

The dominant noise contributors in a bolometer are: the Johnson noise,  $U_{NJ}$ , the phonon noise,  $U_{NF}$ , and the low frequency flicker noise,  $U_{NFL}$ . For a 1 Hz (post-detection) bandwidth, the corresponding noise voltages are [14]:

$$U_{NJ} = (4RkT)^{0.5} \quad (3)$$

$$U_{NF} = (4kT^2G)^{0.5} S_V$$

$$U_{NFL} = i^x f(\omega)$$

where  $x (>0)$  depends on the device nature, and  $f(\omega)$  is the flicker noise frequency dependence. The Noise Equivalent Power (NEP) is calculated as:

$$NEP^2 = 4RkT/R_V^2 + 4kT^2G + i^{2x} f(\omega)^2/R_V^2 \quad (4)$$

#### B. Mixer

The theory of bolometric mixers has been discussed e.g. in [15]. Interference of the Local Oscillator (LO) and the Signal (S) waves results in an amplitude modulation of the

signal at an Intermediate Frequency (IF),  $\omega_0 = |\omega_{LO} - \omega_S|$ . It has been shown [15], that the mixer conversion gain is :

$$G_m = \frac{2 \cdot i^2 \cdot C_0^2 \cdot P_{LO} \cdot R_L}{(R_L + R_0)^2} \cdot \left(1 - i^2 \cdot C_0 \cdot \frac{R_L - R_0}{R_L + R_0}\right)^{-2} \quad (5)$$

where  $C_0 = \partial R / \partial T \cdot 1/G$  is the self-heating parameter,  $R_L$  is the IF load impedance (50 Ohm in the most cases),  $R_0$  is the bolometer dc resistance. Using the definition of the self-heating parameter, the expression for the voltage responsivity (2) can be simplified to:

$$R_V = i \cdot C_0 \quad (6)$$

From the analysis of equations (2) and (5) we conclude that the conversion gain is proportional to the square of the responsivity,  $G_m \sim R_V^2$ . In (5), we assume that  $C_0$  is an invariant of both  $i$  and  $P_{LO}$ . Because the temperature of the bolometer increases when either the bias current or the LO power is applied, the mentioned condition is valid only if the thermal conductance  $G$  is temperature independent (see the definition of  $C_0$  above).

## V. MEASUREMENTS OF THE THERMAL CONDUCTANCE

Using equation (1a), the thermal conductance  $G$  can be derived from  $IV$ -curves and  $\partial R / \partial T$  (Fig.3). In Table I we summarize the thermal conductance for several devices that were measured at room temperature. The  $G$  scales approximately with the bolometer area.

TABLE I. THERMAL CONDUCTANCE FROM THE BOLOMETERS.

Device size ( $\mu\text{m}^2$ )	4x1	3x1	2x1
$G$ at 292K ( $\times 10^{-4}$ W/K)	1.45	0.86	0.53

For a  $3\mu\text{m} \times 1\mu\text{m}$  bolometer, the thermal conductance versus temperature was measured at several temperatures down to 112K, see Table II.

If the heat flow into the substrate is the dominant bolometer cooling path, then the  $G$  equals to a ratio of the bolometer area to the bolometer/substrate thermal boundary resistance,  $R_{bd}$ :

$$G = A / R_{bd} \quad (7)$$

A temperature independent thermal boundary resistance for YBCO films on a sapphire substrate has been reported earlier, although for much larger structures [16]. From these facts we can conclude that for our micrometer scale YBCO bolometers the cooling occurs mainly into the substrate and the heat diffusion into the contact pads is still not visible.

TABLE II. THERMAL CONDUCTANCE FROM A  $3\mu\text{m} \times 1\mu\text{m}$  BOLOMETER VERSUS TEMPERATURE.

$T$ (K)	293	218K	171K	112K
$G \times 10^{-4}$ , W/K	1.66	1.58	1.42	1.66

Because the  $G$  is temperature independent, both the LO power and the bias current can be increased in order to maximize the mixer conversion gain. This statement is also

true for the bolometer responsivity (although, for the bias current only). The upper limits for both  $i$  and  $P_{LO}$  will be discussed in Section VII.

## VI. RESPONSIVITY MEASUREMENTS

In order to correlate variations of the thermal conductance to the bolometer responsivity, we compared the measured responsivity of devices of several sizes at the same bias current, 1mA (Table III)

TABLE III SUMMARY OF THE RESPONSIVITY MEASURED AT 1mA BIAS CURRENT. DEVICE #4 WAS TESTED AT 1GHZ RF FREQUENCY. DATA FOR THE REST OF THE DEVICES REFER TO 330GHZ RF FREQUENCY.  $U_{LIA}$  IS THE VOLTAGE RESPONSE (MEASURED WITH THE LOCK-IN) FOR THE SPECIFIED ABSORBED RF POWER  $P_{abs}$ .

$w \times l$ , $\mu\text{m}^2$	$R_{300}$ , Ohm	$U_{LIA}$ ( $\mu\text{V}$ ) (at 290K, 1mA)	$R_V$ (V/W) at $i=1\text{mA}$	$P_{abs}$ , $\mu\text{W}$
4x1	30	17	0.63	63
3x1	45	38	1.40	63
2x1	55	65	2.40	67
2x1	53	30*	3.00	25*

\*at 1GHz RF.

Most of the measurements were done at 330GHz, except for one bolometer, which was tested at 1GHz.

At the constant bias current the responsivity scales inversely with the bolometer area (Table III), which is in agreement with our measurements of the thermal conductance for the same devices.

The measured responsivity scales linearly with the bias current (Fig.4, symbols), as it is expected from (2) (Fig.4, solid lines). For large bias currents, the  $R_V(i)$  deviates from a linear function, because the denominator in (2) starts to decrease.

A nearly constant responsivity from 300GHz till 1.6THz for the discussed YBCO bolometers was reported in [11] for an operation temperature of 77K. At room temperature, the bolometers are expected to have similar RF bandwidth that is limited by the antenna.

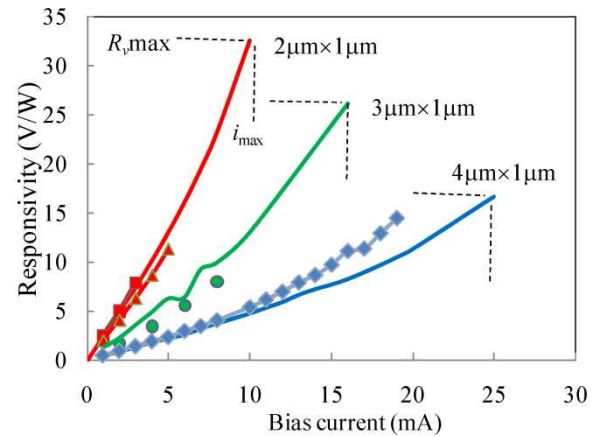


Fig. 4. Calculated from the devices dc parameters (solid lines) and measured (dots) voltage responsivity of YBCO bolometers at room temperature. The maximum bias currents and the corresponding maximum responsivity are marked by the dashed lines.

## VII. RESPONSIVITY LIMITS

### A. Direct detection

The voltage responsivity (2) of a bolometer is proportional to the bias current, the temperature derivative of the

resistance,  $\partial R/\partial T$ , and the thermal conductance to the substrate. The later is proportional to the device area; such that a smaller device should provide a higher responsivity. In Fig. 4, we plot the calculated responsivity versus the bias current for several devices (solid lines). For the calculations we used values of  $G$  as discussed in the previous sections. In order to obtain a higher responsivity the bias current can be increased, although until the device breaks. Our experience shows that the breakdown voltage scales with the device size and it seems to be caused by device overheating. The rise of the bolometer temperature over the substrate temperature can be calculated from equations (1):

$$\Delta T = \frac{i^2 \cdot R}{G - i^2 \cdot \alpha \cdot R}$$

A rapid increase of the bolometer temperature occurs when the  $i^2 \cdot \alpha \cdot R$  term approaches the value of  $G$  (commonly discussed as thermal runaway for current biased bolometers). We introduce a bias current limit as:

$$i_{max} = (0.3 G / \alpha R)^{0.5} \quad (8)$$

Using present device parameters, it can be calculated that the maximum current corresponds approximately to a bolometer temperature rise of 150- 200 K.

We calculate the maximum bias current values for the devices and show them in Fig. 4 together with the corresponding maximum values for the responsivity.

As expected, larger bolometers allow for a larger bias current. However, the resulting maximum responsivity increases as the bolometer size is reduced. A responsivity of up to 30 V/W can be achieved for a  $2\mu\text{m} \times 1\mu\text{m}$  bolometer at the room temperature at the 11 mA bias current.

For the maximum bias currents of 11mA, 16mA, and 26mA for the discussed bolometers of  $2\mu\text{m} \times 1\mu\text{m}$ ,  $3\mu\text{m} \times 1\mu\text{m}$ , and  $4\mu\text{m} \times 1\mu\text{m}$  in size, the corresponding values for the dissipated dc (Joule) power are: 9mW, 16mW, and 27mW.

### B. Mixer

In the case of heterodyne detection, both the bias current and the LO power act towards a higher conversion gain. For safe operation of the mixer, the total dissipated power ( $P_{dc} + P_{LO}$ ) has not to exceed the maxim values discusses in the previous Section. From (5) it is also seen that the conversion gain is proportional to a product  $i^2 \times P_{LO} = P_{dc} \times P_{LO} / R_0$ . For a constant  $(P_{dc} + P_{LO}) = P_{max}$ , the  $P_{dc} \times P_{LO}$  product is maximized when  $P_{dc} = P_{LO} = 0.5 P_{max}$ .

Using measured device parameters, the computed maximum total dissipated power, and the maximum bias current, we calculated the maximum conversion gain for the discussed bolometric mixers. The maximum gain is the same for the discussed devices, as shown in Table IV. However, the optimal  $P_{LO}$  is reduced for smaller devices. Because at THz frequencies the output power of LO sources is low, reduction of the bolometer size to a submicrometer scale will be desirable.

The calculated conversion gain as a function of the bias current for a  $3\mu\text{m} \times 1\mu\text{m}$  bolometer is plotted in Fig. 5 for the LO power of 0.038mW (red line) and 1.5 mW (blue line). The conversion gain, measured at 100 GHz for various LO power values, is shown by symbols. The measured points

follow the theoretical curves very well. For the maximum available LO power of 0.74mW, the measured conversion gain was -28dB at 10mA bias current.

TABLE IV.  
MAXIMUM CONVERSION GAIN,  $G_{max}$  CALCULATED FOR THE DISCUSSED BOLOMETERS. DEVICE PARAMETERS, WHICH WERE USED FOR THE CALCULATIONS, ARE ALSO GIVEN.

Size ( $\mu\text{m}^2$ )	2x1	3x1	4x1
$G_{max}$ (dB)	-18.6	-16.9	-18.7
$C$ ( $\Omega/\text{mW}$ )	2.6	1.6	0.5
$i_{max}$ (mA)	8.2	11.4	18
$R_0$ ( $\Omega$ )	72	58	40
$P_{LO}$ (mW)	4.8	7.5	13

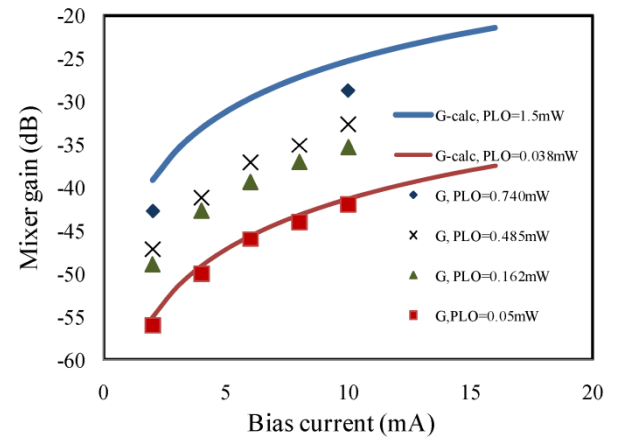


Fig. 5. Calculated (solid lines) and measured (scattered symbols) conversion gain for various LO power for a  $3\mu\text{m} \times 1\mu\text{m}$  YBCO bolometers mixer at room temperature.

### VIII. RESPONSE TIME

The bolometer response time is defined as a ratio of the bolometer heat capacitance,  $C$  to the thermal conductance into the heat sink,  $G$ :

$$\tau = C/G \quad (9)$$

Up to now, we discussed the bolometer operation in the quasi-stationary regime, i.e. when the RF signal modulation frequency  $\omega \ll 1/\tau$ , where  $\tau$  is the bolometer time constant, or the response time. At an arbitrary modulation frequency,  $\omega$  the bolometer responsivity is [14]:

$$R_V(\omega) = \frac{R_V(0)}{\sqrt{1 + \omega^2 \tau^2}} \quad (10)$$

where  $R_V(0)$  is the responsivity at  $\omega=0$ .

A faster response time allows for higher acquisition rates (e.g. for a greater frame rate in a THz camera). Using high modulation frequencies also helps to avoid the flicker noise of the readout electronics (which normally scales as  $1/\omega$ ).

For a bolometric mixer, a faster response time means a larger gain bandwidth. The gain bandwidth is defined by a cut-off IF frequency, where the mixer gain rolls down by a factor of two of its value at zero frequency:

$$G_m(\omega_{IF}) = \frac{G_m(0)}{1 + \omega_{IF}^2 \tau^2} \quad (11)$$

Because both the heat capacitance and the thermal conductance are proportional to the bolometer area, the time constant does not depend on the bolometer area, but scales with the product of the YBCO specific heat, the film thickness, and the thermal boundary resistance (see (7) and (9)).

The specific heat of YBCO films at room temperature is approximately 400 J/kg×K (see e.g. [17]). Therefore, the response time can be calculated using (9) and results of the thermal conductance measurements from Section V. We obtain a time constant of approximately 2.2 ns.

The time constant can be also obtained by fitting the measured responsivity versus modulation frequency by (10), or the IF signal versus IF by (11).

We measured the voltage response of an YBCO microbolometer using a 90GHz active multiplier chain [18]. The input signal from an Agilent signal generator (15 GHz) was amplitude modulated in the range from 10Hz to 100kHz. In this frequency range, the bolometer response remained constant, with approximately 15% signal rise from 50 kHz to 100 kHz, which we currently cannot explain.

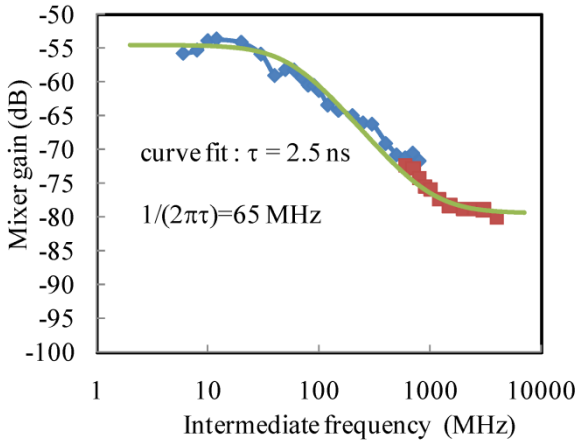


Fig. 6. Room temperature YBCO mixer signal versus IF (symbols), and a fitting curve corresponding to a response time of 2.5 ns (solid line). The corresponding mixer gain bandwidth is 65 MHz. Two microwave amplifiers were used in order to cover the IF range from 8MHz to 4 GHz.

In order to extend measurements to higher modulation frequencies, a mixing of two 90GHz sources was used. The sources were coupled to the mixer via a W-band 20dB directional coupler. A stronger source was used as the LO. The frequency of the other source (the signal) was tuned to provide an IF from 8MHz to 4GHz. The IF line width of a few MHz did not allow an IF lower than 8 MHz to be used. At each frequency point the signal source was amplitude modulated at a low frequency (20Hz) and the voltage response was measured using the lock-in amplifier. This signal was later used to calibrate for the power variation of the signal source during the frequency tuning. The result of the measurement is shown in Fig.6.

The measured  $G_m(\text{IF})$  curve has two time constants present, as it has already been reported for superconducting YBCO bolometers [19]. The lower frequency roll-off is associated with the thermal conductance through the film/substrate interface (often called a bolometric response).

A reasonable fit to our measurements can be done using a 2.5 ns time constant. This response time corresponds to a 3dB gain roll-off at 65 MHz. Above 1 GHz, the mixer gain has a second plateau that has previously been associated with the non-equilibrium response of the YBCO film [19]. For an YBCO film at room temperature, the effect of the THz current is entirely thermal because there is no other mechanism to increase the film's resistance except the Joule heating. Therefore, the shape of the  $G_m(\text{IF})$  curve will remain the same at higher RF frequencies. Our measurements on similar bolometers in the resistive state at 77K [11] showed that this is true for  $G_m(\text{IF})$  recorded at both 90 GHz and 530 GHz.

## IX. NOISE

The noise voltage in the  $4\mu\text{m} \times 1\mu\text{m}$  YBCO bolometer was measured from 20 Hz up to 100 kHz using the lock-in amplifier. The input noise of the lock-in amplifier was measured with a 50  $\Omega$  resistor connected instead of the bolometer and biased at 10mA (Fig.7, circles). The Johnson noise of the resistor at room temperature is 0.9 nV/Hz<sup>0.5</sup>. Therefore, as it appears from Fig. 7, the readout noise is determined by the noise of the lock-in amplifier (3-4 nV/Hz<sup>0.5</sup>) at and above 200 Hz. At lower frequencies, the 1/f noise is dominating, probably originating from the dc bias current source.

Results of the bolometer noise measurements at 1mA, 3mA, and 15mA bias currents are shown in Fig.7 with crosses, diamonds, and triangles, respectively. The 1/f noise is clearly visible at low frequencies. It scales approximately linearly with the bias current. At 15mA, the system noise is reduced to 5-6 nV/Hz<sup>0.5</sup> for frequencies above 5kHz, close to the noise of the lock-in amplifier. For a responsivity of 10V/W (corresponding to the 15 mA bias, Fig.4), the system noise equivalent power is calculated as  $NEP=600 \text{ pW/Hz}^{0.5}$ . By subtracting the readout noise, the bolometer NEP is calculated as  $((6 \text{ nV/Hz}^{0.5})^2 - (4 \text{ nV/Hz}^{0.5})^2)^{0.5} / 15 \text{ V/W} = 450 \text{ pW/Hz}^{0.5}$ .

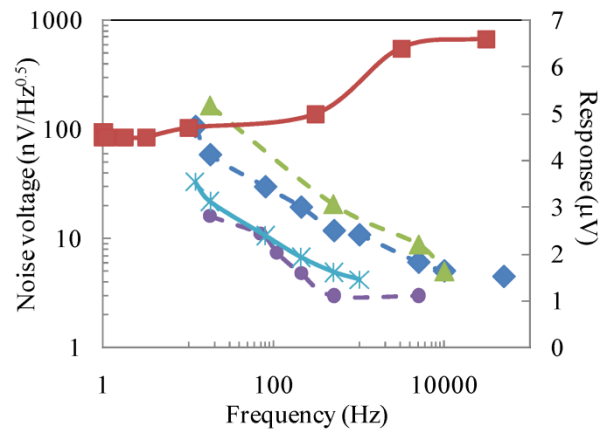


Fig. 7. Noise spectra of a  $4\mu\text{m} \times 1\mu\text{m}$  YBCO bolometer at 1mA (crosses), 3mA (diamonds), and 15mA (triangles) bias current. Response spectrum (squares) is shown for a 3mA bias current. Circles show the noise of a biased (10mA) 50 Ohm resistor.

Using bolometer characteristics as discussed in the previous sections, the Johnson noise and the phonon noise can be calculated from (3) as 0.72 nV/Hz<sup>0.5</sup>, and 0.33 nV/Hz<sup>0.5</sup>, respectively. Therefore, for the  $4\mu\text{m} \times 1\mu\text{m}$  YBCO bolometer the projected minimum NEP is

78 pW/Hz<sup>0.5</sup> for a bias current of 15 mA and modulation frequencies above the cut-off of the  $I/f$  noise. These results show that the measured NEP is limited by the readout and it can be further reduced for a preamplifier with a lower input noise.

As we discussed in Section V, the responsivity inversely scales with the bolometer size. The bias current will be reduced proportionally to the bolometer width. The later fact might lead to a reduced low frequency noise. However, more research on the noise in nanometer size bolometers is needed.

Due to a low TCR of YBCO films at room temperature, the Johnson noise will also dominate over the phonon noise in YBCO mixers [15]. Therefore, the output noise of YBCO mixers at room temperature shall be approximately 300 K (-174dBm/Hz). During our mixer tests, the system output noise (at 20 MHz) was measured to be approximately the same as with a 50 Ω load replacing the mixer at the IF amplifier input. It means that our estimate for the mixer IF noise is correct. With a -28dB conversion loss, the input noise is calculated to be -146 dBm/Hz.

## X. CONCLUSION

Thin YBCO films appear to be very promising for room temperature THz microbolometers. Made on a bulk substrate, bolometers demonstrate a response time of 2 ns (65MHz), which is approximately a factor of 1000 smaller than for any other room temperature bolometers. Integrated with an antenna, the bolometer area can be made very small that reduces the bolometer thermal coupling to the substrate and, hence, increases the responsivity. At the present bolometer size (~μm) the measured NEP is 450 pW/Hz<sup>0.5</sup>. This NEP is similar to the NEP recently reported for MOSFET detectors [20]. Using e-beam lithography, bolometers of 100nm×100nm can be fabricated. In [11] the following equation for the bolometer responsivity was obtained:  $S_V = \frac{1}{3} \times (j_c \times \alpha \times \rho_n \times R_b) / w$ , where  $j_c$  is the bias current density. This equation accounts both for the thermal conductance for the bias current decrease when the bolometer size is reduced. For submicrometer size bolometers, the responsivity and, likely, the NEP are projected to improve by a factor of 10. Although in the superconducting state a higher responsivity and a lower NEP can be achieved [11], ability to operate at room temperature offers undeniable advantages. The RF bandwidth of the discussed YBCO bolometers is limited only by the antenna that can span over a few THz. Fabrication of the YBCO microbolometers is very straightforward and large bolometer arrays are quite feasible.

For heterodyne detection, YBCO bolometer mixers demonstrate a conversion gain of -28dB with a -3dB roll-off at 65MHz. For these devices (3μm×1μm) the maximum conversion gain is projected to be -17dB for a LO power of 7.5 mW. The optimal LO power scales inversely with the bolometer size. Therefore, using submicrometer size bolometers will relax the LO source requirements. The input noise of the 3μm×1μm mixer is -146dBm/Hz, i.e. approximately 30dB lower, compared to the aforementioned

MOSFET detectors in the heterodyne mode [20].

## REFERENCES

- [1] P.H. Siegel, "Terahertz technology," *IEEE Trans. Microw. Theory Tech.*, vol. 50, no. 3, pp. 910-928, March 2002.
- [2] J. Federici and L. Moeller, "Review of terahertz and subterahertz wireless communications," *J. Appl. Phys.*, **107**, 111101, 2010
- [3] A. Leitenstorfer, S. Hunsche, J. Shah, M. C. Nuss, and W. H. Knox, "Detectors and sources for ultrabroadband electro-optic sampling: Experiment and theory," *Appl. Phys. Lett.* **74** (11), 1516-1518 (1999)
- [4] H.-B. Liu, H. Zhong, N. Karpowicz, Y. Chen, and X.-C. Zhang, "Terahertz spectroscopy and imaging for defense and security applications," *Proc. IEEE*, Vol. 95, No. 8, pp.1514-1527, August 2007
- [5] J. Zmuidzinas, and P.L. Richards, "Superconducting detectors and mixers for millimeter and submillimeter astrophysics," *Proc. IEEE*, vol.92, no. 10, pp. 1597-1616, Oct. 2004.
- [6] L. Liu, J. L. Hesler, H. Xu, A.W. Lichtenberger, and R. M. Weikle, "A broadband quasi-optical terahertz detector utilizing a zero bias Schottky diode," *IEEE Microwave Wireless Comp. Lett.*, vol. 20, no.9, pp. 504-506, Sept. 2010..
- [7] N. Su, R. Rajavel, P. Deelman, J. N. Schulman, and P. Fay, "Sb-Heterostructure millimeter-wave detectors with reduced capacitance and noise equivalent power" *IEEE Electron Device Lett.*, vol. 29, no. 6, pp. 536-539, June 2008.
- [8] A. W. M. Lee, B. S. Williams, S. Kumar, Q. Hu, and J. L. Reno, "Real-Time Imaging Using a 4.3-THz Quantum Cascade Laser and a 320×240 Microbolometer Focal-Plane Array," *IEEE Photonics Technol. Lett.*, vol. 18, pp. 1415-1417, Jul. 2006.
- [9] N. Butler, R. Blackwell, R. Murphy, R. Silva, and C. Marshall, "Dual use, low cost microbolometer imaging system," in *Infrared Technology XXI, Proc. SPIE*, vol. 2552, pp. 583-592, 1995.
- [10] A. J. Miller, A. Luukanen, E. N. Grossman, "Micromachined antenna-coupled uncooled microbolometers for terahertz imaging arrays," *Proc. SPIE - Int. Soc. Opt. Eng. (USA)* vol.5411, pp. 18-24, 2004.
- [11] A. Hammar, S. Cherednichenko, S. Bevilacqua, V. Drakinskiy, and J. Stake, "Terahertz direct detection in YBa<sub>2</sub>Cu<sub>3</sub>O<sub>7-x</sub> microbolometers," submitted to *IEEE Trans. Terahertz Science Technol.*, 2011.
- [12] A. D. Semenov, H. Richter, H.-W. Hübers, B. Günther, A. Smirnov, K. S. Il'in, M. Siegel, and J. P. Karamarkovic, "Terahertz performance of integrated lens antennas with a hot-electron bolometer," *IEEE Trans. Microwave Theory Tech.*, vol. 55, no.2, pp. 239-247, Feb. 2007.
- [13] H. Ekström, B. S. Karasik, E. L. Kollberg, and K. S. Yngvesson, "Conversion gain and noise of niobium superconducting hot electron mixers," *IEEE Trans. Microwave Theory Tech.*, vol. 43, no.4, pp. 938-947, Apr. 1995.
- [14] P.L. Richards, "Bolometers for infrared and millimeter waves," *J. Appl. Phys.* Vol. 76, pp.1-24, July 1994.
- [15] F.Arams, C. Allen, P. Peyton, E. Sard, "Millimeter mixing and detection in bulk InSb," *Proc. IEEE*, Vol. 54, No. 8, pp.612-622, Apr. 1966.
- [16] M. Nahum, S. Verghese, P. L. Richards, and K.Char, "Thermal boundary resistance for YBa<sub>2</sub>Cu<sub>3</sub>O<sub>7-x</sub> films," *Appl. Phys. Lett.*, vol. 59, no. 16, pp. 2034-2036, Oct. 1991.
- [17] P. Langlois, D. Robbes, M. Lam Chok Sing, C. Gunther, D. Bloyet, J. F. Hamet, R. Desfeux, and H. Murray, "Superconducting fast microbolometers operating below their critical temperature," *J. Appl. Phys.*, vol.76, no.6, pp. 3858-3868, Sept. 1994.
- [18] ALMA VWR LO source, Omnisys Instruments AB, Göteborg, Sweden.
- [19] O. Harnack, K. S. Il'in, M. Siegel, B. S. Karasik, W. R. McGrath, and G.de Lange, "Dynamics of the response to microwave radiation in YBa<sub>2</sub>Cu<sub>3</sub>O<sub>7-x</sub> hot-electron bolometer mixers," *Appl. Phys. Lett.* Vol.79, pp.1906-1908, Sept. 2001.
- [20] D. Glaab, S. Boppel, A. Lisauskas, U. Pfeiffer, E. Öjefors, and H. G. Roskos, "Terahertz heterodyne detection with silicon field-effect transistors," *Appl. Phys. Lett.*, **96**, 042106 (2010).



**Sergey Cherednichenko**, was born in Mariupol, Ukraine in 1970. He received the Diploma with Honours in Physics in 1993 from Taganrog State Pedagogical Institute, and Ph.D. in physics in 1999 from Moscow State Pedagogical University. He is working at the Department of Microtechnology and Nanoscience at Chalmers University of Technology (Gothenburg, Sweden). From 2000-2006 he was involved in development of terahertz band superconducting mixers for the Herschel Space Observatory; and from 2008 till 2009 in the water vapour radiometer for ALMA. From 2007 he is Associate Professor at the department of Microtechnology and Nanoscience of Chalmers University of Technology. His research interests include terahertz heterodyne receivers and mixers, photon detectors; THz antennas and optics; thin superconducting films and their application for THz and photonics; and material properties at THz frequencies.



**Arvid Hammar** was born in Uddevalla, Sweden in 1986. He received the B.Sc. degree in 2008 from the department of Earth and Space Sciences at Chalmers University of Technology, Gothenburg, Sweden. The thesis included measurements of the characteristic 21 cm line from H1 gas in the Milky Way and an evaluation of a minor radio telescope system at Onsala Space Observatory. In 2009 he was working at the Institute of High Energy Physics and Astrophysics at University of Florida where he was involved in various programming tasks for the CMS detector at CERN, mainly error analysis and particle trajectory simulations. Since 2010 he has been working as amanuensis at the Terahertz and Millimetre Wave Laboratory, Chalmers University of Technology, where he also currently is working towards the M.Sc. degree. The diploma work is about the development of high Tc hot electron bolometer based on thin YBCO films.



**Stella Bevilacqua**, was born in Pizza Armerina, Italy in 1981. She received B.Sc. degree in Electronic Engineering from the University of Catania, Italy, in 2006. During a four months period, she has done her thesis work in the Smart-Card group of the MPG division of Catania STMicroelectronics. In April 2010, she received M.Sc. degree in Microelectronic Engineering from the University of Catania. She was a diploma worker at Chalmers University of Technology in the Department of Microtechnology and Nanoscience, where she was working towards her master thesis: 'Fabrication and Characterization of Graphene field-effect transistors (GFETs)', for a six months period. Currently, she is a PhD student the department of Terahertz Millimeter Wave Laboratory of the Chalmers University of Technology, working on MgB2 Hot Electron Bolometers.



**Vladimir Drakinskiy** was born in Kurganinsk, Russia, in 1977. He received the Diploma degree in Physics and Informatics (with honors) from the Armavir State Pedagogical Institute, Armavir, Russia, in 2000. From 2000 to 2003, he was with the Physics Department, Moscow State Pedagogical Univ., Russia, as a post-graduate student, junior research assistant. Since 2003 he has been with the Department of Microtechnology and Nanoscience of Chalmers University of Technology (Gothenburg, Sweden). In 2003-2005 he was responsible for mixer chips fabrication for the Herschel Space Observatory in 2003-2005. From 2008 he is Research Engineer at the department Microtechnology and Nanoscience of Chalmers University of Technology. His research interests include micro- and nanofabrication techniques, detectors for submillimetre and terahertz ranges and superconducting thin films.



**Jan Stake** (S'95-M'00-SM'06) was born in Uddevalla, Sweden in 1971. He received the degrees of M.Sc. in electrical engineering and Ph.D. in microwave electronics from Chalmers University of Technology, Göteborg, Sweden in 1994 and 1999, respectively. In 1997 he was a research assistant at the University of Virginia, Charlottesville, USA. From 1999 to 2001, he was a Research Fellow in the millimetre wave group at the Rutherford Appleton Laboratory, UK, working on HBV diode multiplier circuits for submillimeter-wave signal generation. He then joined Saab Combitech Systems AB as a Senior System Consultant, where he worked as an RF/microwave engineer until 2003. From 2000 to 2006, he held different academic positions at Chalmers and was also Head of the Nanofabrication Laboratory at MC2 between 2003 and 2006. During the summer 2007, he was a visiting professor in the Submillimeter Wave Advanced Technology (SWAT) group at Caltech/JPL, Pasadena, USA. He is currently Professor and Head of the Terahertz and Millimetre Wave Laboratory at the department of Microtechnology and Nanoscience (MC2), Chalmers, Göteborg, Sweden. His research involves sources and detectors for terahertz frequencies, high frequency semiconductor devices, graphene electronics, terahertz techniques and applications. He is also co-founder of Wasa Millimeter Wave AB.



**Alexey Kalabukhov** was born in Moscow, Russia in 1975. He received his PhD degree in physics and mathematics from Moscow State University in 2003. His main research work is in design and fabrication of high-Tc SQUIDS for various applications including non-destructive evaluation and high-frequency amplifiers. In 2003, he joined the Quantum Device Physics group of the Microtechnology and Nanoscience department, Chalmers University of Technology. Recently, he has been working in the field of oxide electronics and functional oxide interfaces.

# Terahertz direct detection in $\text{YBa}_2\text{Cu}_3\text{O}_7$ microbolometers

Arvid Hammar, Sergey Cherednichenko, Stella Bevilacqua, Vladimir Drakinskiy, and Jan Stake,  
*Senior Member, IEEE*

**Abstract**— A high sensitivity broadband terahertz direct detector based on  $\text{YBa}_2\text{Cu}_3\text{O}_7$  high-Tc superconductor microbolometers is presented. At 77 K, the responsivity of the spiral antenna-integrated microbolometers ( $1.5 \mu\text{m} \times 1.5 \mu\text{m}$ ) is 190 V/W, referenced to the input of the silicon substrate lens, across the frequency range of 330 GHz to 1.63 THz in a single device. The response time is approximately 300 ps. Using a room temperature readout, we measure an optical noise equivalent power (NEP) of  $20 \text{ pW/Hz}^{1/2}$  (readout noise limited) for modulation frequencies ranging from 500 Hz to 100 kHz.

**Index Terms**—Terahertz (THz) detectors, microbolometers, spiral antenna, superconductor, YBCO.

## I. INTRODUCTION

Antenna integrated superconducting microbolometers have been used both for heterodyne and direct detection at terahertz frequencies (100 GHz to 10 THz), although mainly for radio astronomy [1], [2]. Necessity of LHe cooling prevented bolometers from being used in other applications, like THz imaging, spectroscopy [3]. After the discovery of high-temperature superconductors, significant attention has been paid to the implementation of superconducting bolometers that are capable of operating at temperatures as high as 90 K [4], [5]. At the moment, very compact cryocoolers are available, with a cooling capacity down to 77K [6]. It makes high-Tc bolometers potentially attractive for a wide use.

As direct detectors,  $\text{YBa}_2\text{Cu}_3\text{O}_7$  (YBCO) bolometers have been theoretically predicted to reach a phonon noise-limited NEP of  $3 \text{ pW/Hz}^{0.5}$ . This is much lower than for other wideband THz detectors, like Golay cells or pirodetectors. In [7], an NEP of  $\sim 9 \text{ pW/Hz}^{0.5}$  was reported for an YBCO bolometer with a log-periodic antenna. Such sensitivity was achieved by thermally isolating the bolometer using an air-bridge approach. The resulting response time was  $\tau \sim 10 \mu\text{s}$ . In [8], an YBCO bolometer on a bulk YSZ substrate was discussed with an electrical NEP of  $\sim 4.5 \text{ pW/Hz}^{0.5}$ ; however, the optical efficiency was only 5%. This bolometer had a time

constant of  $\sim 20 \mu\text{s}$ . In both cases, the THz optical responsivity was measured using broadband black body sources. Therefore, spectral information on the YBCO bolometer responsivity across the THz range was not accessible. Furthermore, many applications require detectors with even higher response rate.

In general, bolometers on bulk substrates are more attractive from a practical point of view. This device structure makes them more robust, and the fabrication process is more reproducible. For YBCO thin films on bulk substrates, a bolometric response on the order of  $\sim \text{ns}$  can be achieved [9].

In this paper, we present an antenna integrated YBCO microbolometer, where we combine both a high sensitivity (comparable to Schottky diode detector) and a sub-nanosecond response time in a single device. We performed optical characterization of the bolometer over a wide frequency range, from 330 GHz to 1.63 THz. Both the responsivity and the noise were optimized versus the bolometer operation temperature.

## II. DEVICE FABRICATION

Bolometers were fabricated using 50-nm-thick YBCO films on sapphire substrates with a  $\text{CeO}_2$  buffer layer using pulsed laser deposition. The critical temperature was 88 K in continuous film. The YBCO film was patterned as a microbridge so as to overlap the antenna (made of 350 nm thick gold film) via UV photolithography (see Fig. 1). The bolometer area between the antenna pads was (the width,  $w$ , times the length,  $l$ )  $1.5 \mu\text{m} \times 1.5 \mu\text{m}$ ,  $2 \mu\text{m} \times 1 \mu\text{m}$ , and  $4 \mu\text{m} \times 1 \mu\text{m}$ . The choice of a logarithmic spiral antenna was motivated by its real impedance of  $90 \Omega$  in a wide frequency

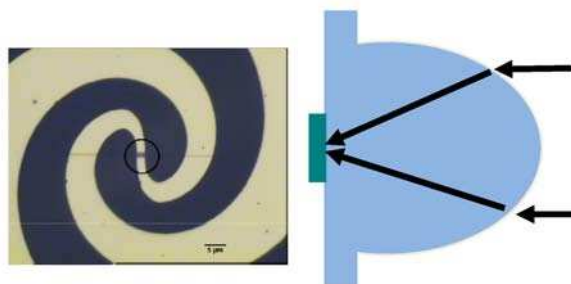


Fig. 1. A photograph of a spiral antenna-integrated YBCO microbolometer. The bright area is gold. The bolometer is at the center (in the circle). (left) The bolometer chip is mounted on an elliptical silicon lens. (right)

Manuscript received April 4, 2011. This work was supported the Swedish Research Council (VR) and the Swedish National Space Board.

The authors are with Chalmers University of Technology, Department of Microtechnology and Nanoscience, Terahertz and Millimetre Wave Laboratory, SE-412 96, Göteborg, Sweden (corresponding author phone: +46-31-7728499; fax: +46-31-164513; e-mail: serguei@chalmers.se).

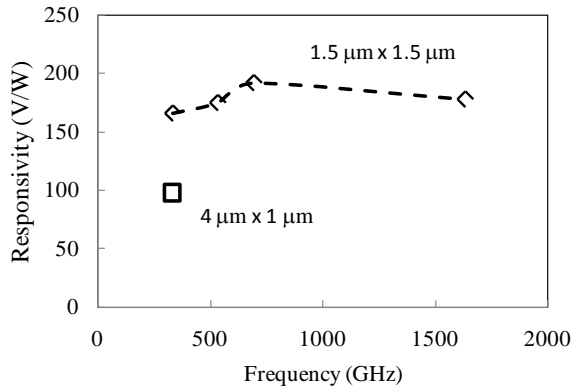


Fig. 2. Responsivity versus signal frequency at 77 K for the  $1.5 \mu\text{m} \times 1.5 \mu\text{m}$  (diamonds) and  $4 \mu\text{m} \times 1 \mu\text{m}$  (square) sized bolometers.

range [10]. The substrate with the antenna-integrated bolometer was then clamped to the backside of a 12-mm elliptical silicon lens. The fabricated microbolometers exhibited a normal state resistivity of  $\rho_n = 270 \mu\Omega \times \text{cm}$  and a critical current density of  $j_c = 4 \text{ MA/cm}^2$  at 77 K, indicating that the high quality of the film was preserved through the fabrication process.

### III. MEASUREMENT TECHNIQUE

The responsivity (the ratio of the output voltage to the incident RF power) was measured at 330 GHz and 530 GHz using a backward wave oscillator (BWO) and at 0.69 THz and 1.63 THz using a FIR gas laser as signal sources. The sources were amplitude modulated by a chopper wheel at 18 Hz, which provided a 100% modulation depth. The incoming THz beam was matched to the bolometer (on the silicon lens) beam using a Teflon lens. The beam power at the cryostat window was calibrated with two types of THz power meters: a Thomas Keating and an Erickson PM4. Spiral antennas are generally elliptically polarized with an axial ratio that varies from zero (linearly polarized at the edges of its frequency band) to 1 (circularly polarized in the middle of the band) [10]. Because the polarization of the THz sources was linear, we assumed a polarization coupling factor to our antenna of 0.5. Another factor, which we included in the beam power calibration, was the transmission coefficient through the cryostat window: 0.7. We have not corrected for Si lens reflection losses. The correction factors (for the polarization and the window loss) were verified during the bolometer tests. For this purpose, the bolometer was heated to a temperature that was above  $T_c$ . In this case, the effects of both the RF power and the dc power on the bolometer were entirely thermal and were, hence, the same. Therefore, the isothermal technique for computation of the RF power absorbed in the bolometer is valid [11]. In this way, we identified that the ratio of the THz power that was incident on the cryostat to the power absorbed by the bolometer was approximately 3.5:1. This ratio agrees with our estimates presented above.

The bolometer response was measured using a lock-in

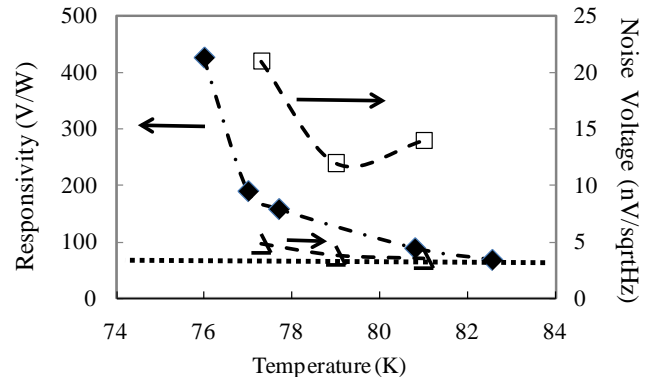


Fig. 3. Responsivity as a function of temperature for a  $2 \mu\text{m} \times 1 \mu\text{m}$  in size bolometer at 330 GHz is shown with filled diamonds. The total system noise (bolometer + readout) is shown with open squares (18 Hz) and triangles (1 kHz). The lock-in amplifier noise (1 kHz) is shown with a dotted line.

amplifier, which had a noise level of approximately 10 and  $3 \text{ nV/Hz}^{0.5}$  at 18 Hz and 1 kHz, respectively. For the noise measurements, the same lock-in amplifier was used with an internal reference source from 18 Hz to 100 kHz. The bolometer response time was measured by mixing both two Gunn diode oscillators (at 100 GHz) and two BWOs (at 530 GHz), and recording the roll-off of the bolometer response versus the beating frequency from 50 MHz to 1.5 GHz. The superior frequency stability of the Gunn oscillators permitted lower beating frequencies to be reached. During all of the measurements, the bolometers were constant current biased to the resistive state, i.e. exceeding the critical current value. At each temperature, responsivity maximums were observed at approximately 40 mV for the  $1.5\text{-}\mu\text{m}$ - and  $2\text{-}\mu\text{m}$ -wide bolometers and at approximately 30 mV for the  $4\text{-}\mu\text{m}$ -wide bolometers. The dc resistance at this point was  $\sim 1/3$  of the normal state value.

### IV. RESULTS AND DISCUSSION

Fig. 2 summarizes the results of the responsivity measurements at 77 K. The responsivity variation from 330 GHz to 1.63 THz appears to be small. For the larger size bolometer, the responsivity is reduced, scaling approximately as the reverse of the bolometer area. The responsivity drastically degrades as the bolometer temperature approaches  $T_c$  (Fig.3).

The measured system noise,  $V_n$ , is strongly dominated by the noise that is coming from the readout. At low modulation frequencies (e.g., at 18 Hz in Fig. 3) up to approximately 200 Hz, the bolometer noise exceeds the lock-in amplifier noise. This low frequency noise decreases as the temperature approaches  $T_c$ . On the contrary, at modulation frequencies above 500 Hz (at 1 kHz in Fig. 3), the lock-in amplifier noise was dominating. The temperature dependence in this case was negligible. From 1 kHz and up to 100 kHz (the higher frequency limit of the lock-in amplifier), the noise stayed constant at approximately  $3 \text{ nV/Hz}^{0.5}$ .

Using the responsivity,  $S_V$ , and the noise voltage, the NEP

was calculated as  $NEP = V_n/S_V$ . The presently achieved NEP is  $110 \text{ pW/Hz}^{0.5}$  at 18 Hz and  $20 \text{ pW/Hz}^{0.5}$  at modulation frequencies of 500 Hz and higher.

The roll-off of the bolometer response to the mixing signal from two THz sources was measured and fitted with a single-pole Lorentzian  $S(f_{IF}) = S(0)/[1+(2\pi \times f_0 \tau)^2]$ , where  $f_0$  is the beating frequency,  $S(0)$  is the response at  $f_0=0$ , and  $\tau$  is the bolometer time constant. The resulting time constant was  $300 \text{ ps} \pm 100 \text{ ps}$ . Considering the volume of the device,  $V$ , and the YBCO specific heat,  $C$  [12], at 90 K, we observed that the heat conductivity from the bolometer to the heat sink ( $G = C \cdot V / \tau$ ) was approximately  $50 \text{ } \mu\text{W/K}$  and  $100 \text{ } \mu\text{W/K}$  for the 2- $\mu\text{m}$ - and the 4- $\mu\text{m}$ -wide devices. Another method of measuring the heat conductivity from the bolometer is as discussed in [8]. The bolometer was heated just above the  $T_c$ , and the resistance change versus the dissipated dc power was measured,  $\partial P_{dc} / \partial R$ . Using the  $\partial R / \partial T$  from the  $R(T)$  curve, the heat conductivity was calculated as  $G = \partial P_{dc} / \partial R \times \partial R / \partial T$ . We performed such computations for the 2- $\mu\text{m}$ - and the 4- $\mu\text{m}$ -wide devices. The obtained values for  $G$  were  $70 \text{ } \mu\text{W/K}$  and  $180 \text{ } \mu\text{W/K}$  for the given sizes, respectively. Although these values are somewhat higher than those we obtained from the time constant measurements, the trend of the heat conductivity versus the device size remains. This trend indicates that at the present bolometer scale, heat removal predominantly occurs into the substrate. Previously measured thermal boundary resistance from the YBCO films to the sapphire substrates [13], is approximately  $10 \text{ } \mu\text{W/K}$  per each  $1 \text{ } \mu\text{m} \times 1 \text{ } \mu\text{m}$  device area. The discrepancy with our results may derive from a superior YBCO/CeO<sub>2</sub>/substrate interface in our devices.

The bolometer responsivity is a function of the temperature coefficient of resistance  $\alpha \equiv \partial R / \partial T \times 1/R$ , the bias current  $i$ , and the thermal conductance to the heat sink  $G$ :  $S_V = i \times \alpha \times R / (G - i^2 \times \alpha \times R)$  [4]. For the used bias conditions, the second term in the denominator (the self-heating coefficient) is much smaller than  $G$ , and it can be neglected. As we have mentioned, the bias current is just above the critical current. The dc resistance is  $R = 1/3 \times \rho_n \times l / (w \times d)$ . Therefore, the expression for the responsivity can be rewritten as:  $S_V = \frac{1}{3} \times (j_c \times \alpha \times \rho_n \times R_b) / w$ . It appears that the bolometer responsivity linearly scales as  $1/w$ , as we experimentally observed (Fig. 2).

It is important to note that nearly all of the YBCO bolometer direct detectors presented in the literature operate at temperatures that are close to the middle of the superconducting transition. Our measurements demonstrate that a higher responsivity can be achieved at lower temperatures; however, the output noise (at least at low frequencies) also increases (Fig.3).

## V. CONCLUSION

We demonstrate that an NEP of  $\sim 20 \text{ pW/Hz}^{0.5}$  is presently achieved with an YBCO microbolometer in the terahertz

range from 330 GHz to 1.63 THz at a 77-K operation temperature and with a room-temperature readout. The response time is  $< 1 \text{ ns}$ . This NEP is comparable to Schottky diode detectors for frequencies below 1 THz [14]. However, YBCO bolometers have real RF impedance, and, therefore are easy to integrate with broadband antennas to extend to several THz. Further sensitivity improvement is feasible for even smaller bolometers. Fabrication of such detectors in large arrays is also quite straightforward.

## ACKNOWLEDGMENT

The authors are grateful to Dr. A. Kalabukhov for the help with the YBCO film deposition.

## REFERENCES

- [1] P.H. Siegel, "Terahertz technology," *IEEE Trans. Microw. Theory Tech.*, vol. 50, no. 3, pp. 910-928, March 2002.
- [2] J. Zmuidzinas, and P.L. Richards, "Superconducting detectors and mixers for millimeter and submillimeter astrophysics," *Proc. IEEE*, vol.92, no. 10, pp. 1597-1616, Oct. 2004.
- [3] R. Appleby, and H.B. Wallace, "Standoff Detection of Weapons and Contraband in the 100 GHz to 1 THz Region," *IEEE Trans. Antennas Propag.*, vol. 55, no. 11, pp. 2944-2956, Nov. 2007.
- [4] P. L. Richards, J. Clarke, R. Leoni, Ph. Lerch, S. Verghese, M. R. Beasley, et al., "Feasibility of the high Tc superconducting bolometer," *Appl. Phys. Lett.*, vol. 54, no. 3, pp. 283-285, Jan. 1989.
- [5] E. M. Gershenzon, G. N. Gol'tsman, I. G. Gogidze, A. I. Elant'ev, B. S. Karasik, and A. D. Semenov, "Millimeter and submillimeter range mixer based on electronic heating of superconducting films in the resistive state," *Sov. Phys. Superconductivity*, vol. 3, no. 10, pp. 1582-159, Oct. 1990.
- [6] <http://www.ricor.com>
- [7] J.P. Rice, E.N. Grossman, and D.A. Rudman, "Antenna-coupled high-Tc air-bridge microbolometers on silicon," *Appl. Phys. Lett.*, vol. 65, no. 6, pp. 773-775, Aug. 1994.
- [8] M. Nahum, Q. Hu, P. L. Richards, S.A. Sachtjen, N. Newman, and B.F. Cole, "Fabrication and measurements of high Tc superconducting microbolometers," *IEEE Trans. Magnetics* . vol. 27, no2, pp. 3081-3084, March 1991.
- [9] A. V. Sergeev, A. D. Semenov, P. Kouminov, V. Trifonov, I. G. Goghidze, B. S. Karasik, G. N. Gol'tsman, and E. M. Gershenzon, "Transparency of a YBa<sub>2</sub>Cu<sub>3</sub>O<sub>7-x</sub> film/substrate interface for thermal phonons measured by means of voltage response to radiation," *Phys. Rev. B*. vol. 49, no.13, pp. 9091-9096 , Apr. 1994
- [10] A. D. Semenov, H. Richter, H.-W. Hübers, B. Günther, A. Smirnov, K. S. Il'in, M. Siegel, and J. P. Karamarkovic, "Terahertz performance of integrated lens antennas with a hot-electron bolometer," *IEEE Trans. Microwave Theory Tech.*, vol. 55, no.2, pp. 239-247, Feb. 2007.
- [11] H. Ekström, B. S. Karasik, E. L. Kollberg, and K. S. Yngvesson, "Conversion gain and noise of niobium superconducting hot electron mixers," *IEEE Trans. Microwave Theory Tech.*, vol. 43, no.4, pp. 938-947, Apr. 1995.
- [12] P. Langlois, D. Robbes, M. Lam Chok Sing, C. Gunther, D. Bloyet, J. F. Hamet, R. Desfeux, and H. Murray, "Superconducting fast microbolometers operating below their critical temperature," *J. Appl. Phys.*, vol.76, no.6, pp. 3858-3868 , Sept. 1994.
- [13] M. Nahum., S. Verghese, P. L. Richards, and K.Char, "Thermal boundary resistance for YBa<sub>2</sub>Cu<sub>3</sub>O<sub>7-x</sub> films," *Appl. Phys. Lett.*, vol. 59, no. 16, pp. 2034-2036, Oct. 1991.
- [14] L. Liu, J. L. Hesler, H. Xu, A.W. Lichtenberger, and R. M. Weikle, "A broadband quasi-optical terahertz detector utilizing a zero bias Schottky diode," *IEEE Microwave Wireless Comp. Lett.*, vol. 20, no.9, pp. 504-506, Sept. 2010.



**Arvid Hammar** was born in Uddevalla, Sweden in 1986. He received the B.Sc. degree in 2008 from the department of Earth and Space Sciences at Chalmers University of Technology, Gothenburg, Sweden.

The thesis included measurements of the characteristic 21 cm line from H1 gas in the Milky Way and an evaluation of a minor radio telescope system at Onsala Space Observatory. In 2009 he was working at the Institute of High Energy Physics and

Astrophysics at University of Florida where he was involved in various programming tasks for the CMS detector at CERN, mainly error analysis and particle trajectory simulations. Since 2010 he has been working as amanuensis at the Terahertz and Millimetre Wave Laboratory, Chalmers University of Technology, where he also currently is working towards the M.Sc. degree. The diploma work is about the development of high Tc hot electron bolometer based on thin YBCO films.



**Sergey Cherednichenko**, was born in Mariupol, Ukraine in 1970. He received the Diploma with Honours in Physics in 1993 from Taganrog State Pedagogical Institute, and Ph.D. in physics in 1999 from Moscow State Pedagogical University.

He is working at the Department of Microtechnology and Nanoscience at Chalmers University of Technology (Gothenburg, Sweden). From 2000-2006 he was involved in development of terahertz band superconducting mixers for the Herschel Space Observatory; and from 2008 till

2009 in the water vapour radiometer for ALMA. From 2007 he is Associate Professor at the department of Microtechnology and Nanoscience of Chalmers University of Technology. His research interests include terahertz heterodyne receivers and mixers, photon detectors; THz antennas and optics; thin superconducting films and their application for THz and photonics; and material properties at THz frequencies.



**Stella Bevilacqua**, was born in Pizza Armerina, Italy in 1981. She received B.Sc. degree in Electronic Engineering from the University of Catania, Italy, in 2006.

During a four months period, she has done her thesis work in the Smart-Card group of the MPG division of Catania STMicroelectronics. In April 2010, she received M.Sc. degree in Microelectronic Engineering from the University of Catania. She was a diploma worker at Chalmers University of Technology

in the Department of Microtechnology and Nanoscience, where she was working towards her master thesis: 'Fabrication and Characterization of Graphene field-effect transistors (GFETs)', for a six months period. Currently,

she is a PhD student the department of Terahertz Millimeter Wave Laboratory of the Chalmers University of Technology, working on MgB2 Hot Electron Bolometers.



**Vladimir Drakinskiy** was born in Kurganinsk, Russia, in 1977. He received the Diploma degree in Physics and Informatics (with honors) from the Armavir State Pedagogical Institute, Armavir, Russia, in

2000.

From 2000 to 2003, he was with the Physics Department, Moscow State Pedagogical Univ., Russia, as a post-graduate student, junior research assistant. Since 2003 he has been with the Department of Microtechnology and Nanoscience of Chalmers University of Technology (Gothenburg, Sweden). In 2003-2005 he was responsible for mixer chips fabrication for the Herschel Space Observatory in 2003-2005. From 2008 he is Research Engineer at the department Microtechnology and Nanoscience of Chalmers University of Technology. His research interests include micro- and nanofabrication techniques, detectors for submillimetre and terahertz ranges and superconducting thin films.



**Jan Stake** (S'95-M'00-SM'06) was born in Uddevalla, Sweden in 1971. He received the degrees of M.Sc. in electrical engineering and Ph.D. in microwave electronics from Chalmers University of Technology, Göteborg, Sweden in 1994 and 1999, respectively.

In 1997 he was a research assistant at the University of Virginia, Charlottesville, USA. From 1999 to 2001, he was a Research Fellow in the millimetre wave group at the Rutherford Appleton Laboratory, UK, working on HBV diode multiplier circuits for submillimeter-wave signal generation. He then joined Saab Combitech Systems AB as a Senior System Consultant, where he worked as an RF/microwave engineer until 2003. From 2000 to 2006, he held different academic positions at Chalmers and was also Head of the Nanofabrication Laboratory at MC2 between 2003 and 2006. During the summer 2007, he was a visiting professor in the Submillimeter Wave Advanced Technology (SWAT) group at Caltech/JPL, Pasadena, USA. He is currently Professor and Head of the Terahertz and Millimetre Wave Laboratory at the department of Microtechnology and Nanoscience (MC2), Chalmers, Göteborg, Sweden. His research involves sources and detectors for terahertz frequencies, high frequency semiconductor devices, graphene electronics, terahertz techniques and applications. He is also co-founder of Wasa Millimeter Wave AB.

## TERAHERTZ DIRECT DETECTION IN $\text{YBa}_2\text{Cu}_3\text{O}_7$ BOLOMETERS FOR APPLICATIONS AT CRYOGENIC AND ROOM TEMPERATURES

### Introduction

We report on the direct detection response of hot electron bolometers (HEB) based on thin films of  $\text{YBa}_2\text{Cu}_3\text{O}_7$ . These bolometers were tested at frequencies 0.1-1.63 THz and for a range of temperatures around 77 K and at 300 K. High optical responsivity, 100 to 500 V/W depending on both temperature and frequency, is combined with a fast response time, 300 ps. An optical noise equivalent power (NEP) of 20  $\text{pW}/\text{Hz}^{1/2}$  (readout limited) was measured at 77 K and for room temperature the NEP was about 450  $\text{pW}/\text{Hz}^{1/2}$ .

### RF Measurements

- Sources: Gunn oscillators (100 GHz), backward wave oscillators (350-550 GHz) and FIR laser (0.69 and 1.63 THz).
- Responsivity, response time and noise measured around 77 K and at 300 K.
- Devices current biased to temperatures just above the critical current when measuring at cryogenic temperatures.
- The incoming power is measured outside the cryostat window. Losses in the cryostat window and circular-to-linear polarization mismatch losses in the antenna/RF-signal are accounted for. At room temperature the absorbed power is taken as the power reference.

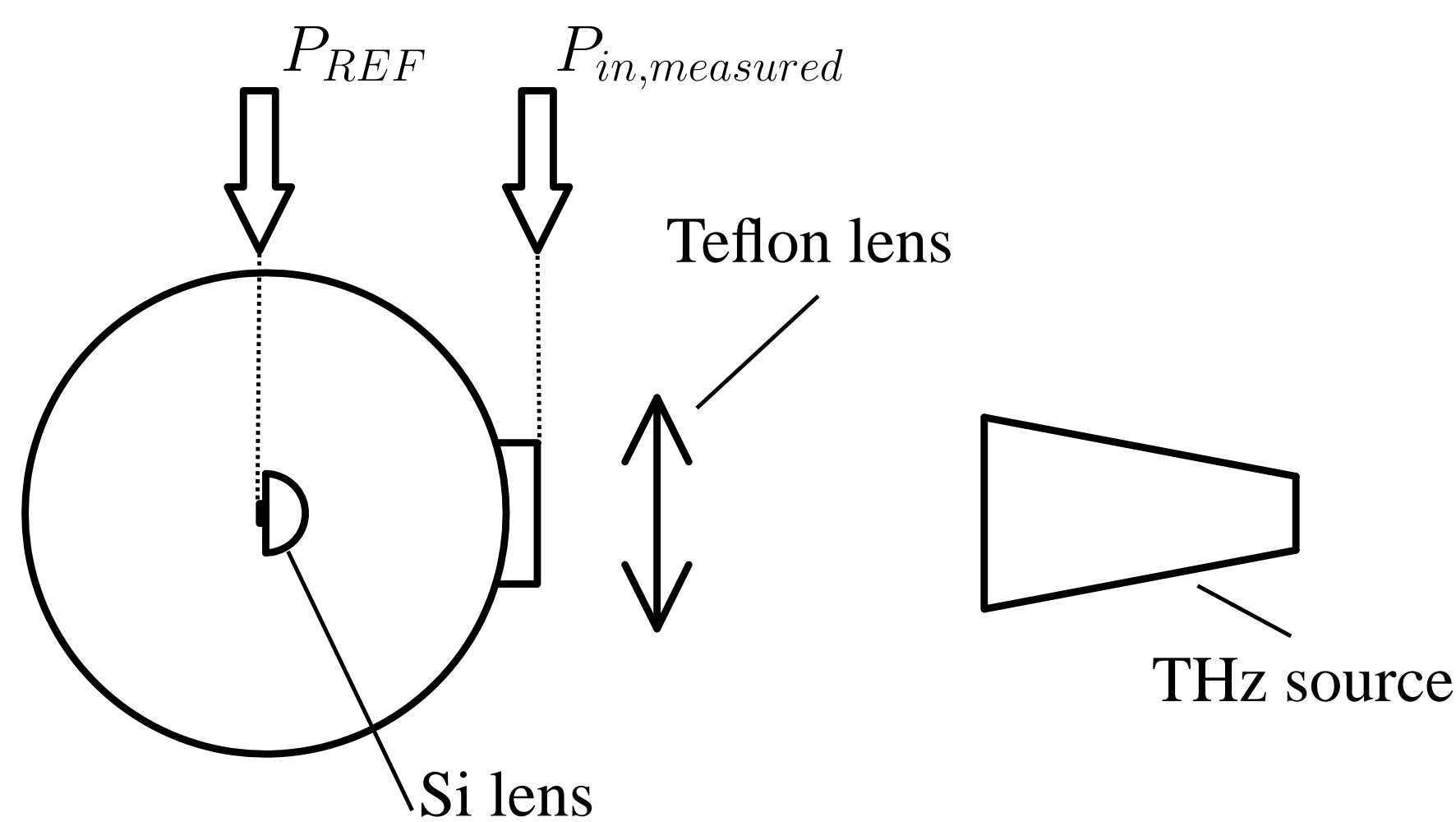
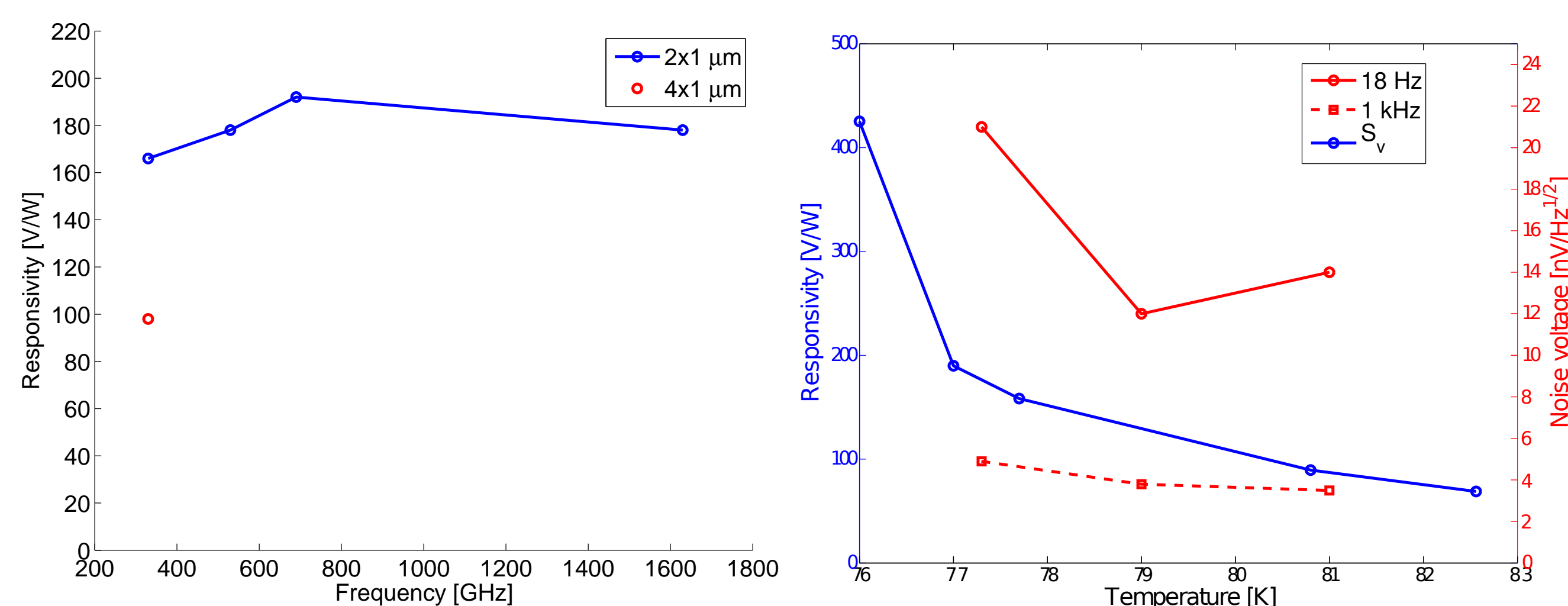


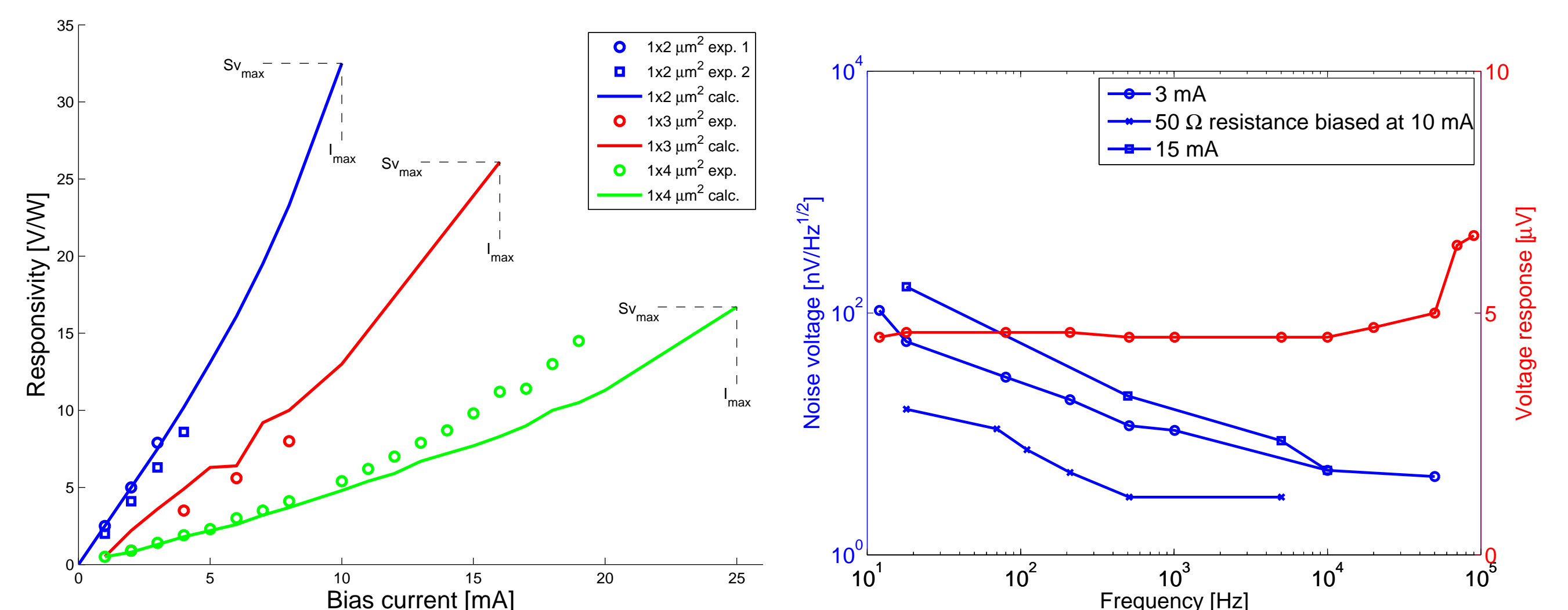
Figure showing the measurement setup with the bolometer mounted on the backside of a Si lens. A chopper was used (not shown in the picture) in front of the cryostat when measuring responsivity.

The signal transmission through the cryostat window was 0.7 and the polarization loss in the antenna was 0.5. Hence,  $P_{REF} = P_{in,measured} \cdot 0.7 \cdot 0.5$ . The rms voltage response was measured with a lock-in amplifier and is used to calculate the responsivity:  $S_V = \frac{\Delta U_{lock-in} \cdot 2.3}{P_{REF}}$ . Theoretically, the responsivity can be calculated as  $S_v = \frac{i\alpha R}{G - i^2\alpha R}$ , where  $\alpha = \frac{1}{R} \frac{\partial R}{\partial T}$ .  $\alpha$  is heavily depending on  $i$  for cryogenic temperatures. At room temperatures,  $\alpha$  is constant.

### CRYOGENIC TEMPERATURES



### ROOM TEMPERATURE

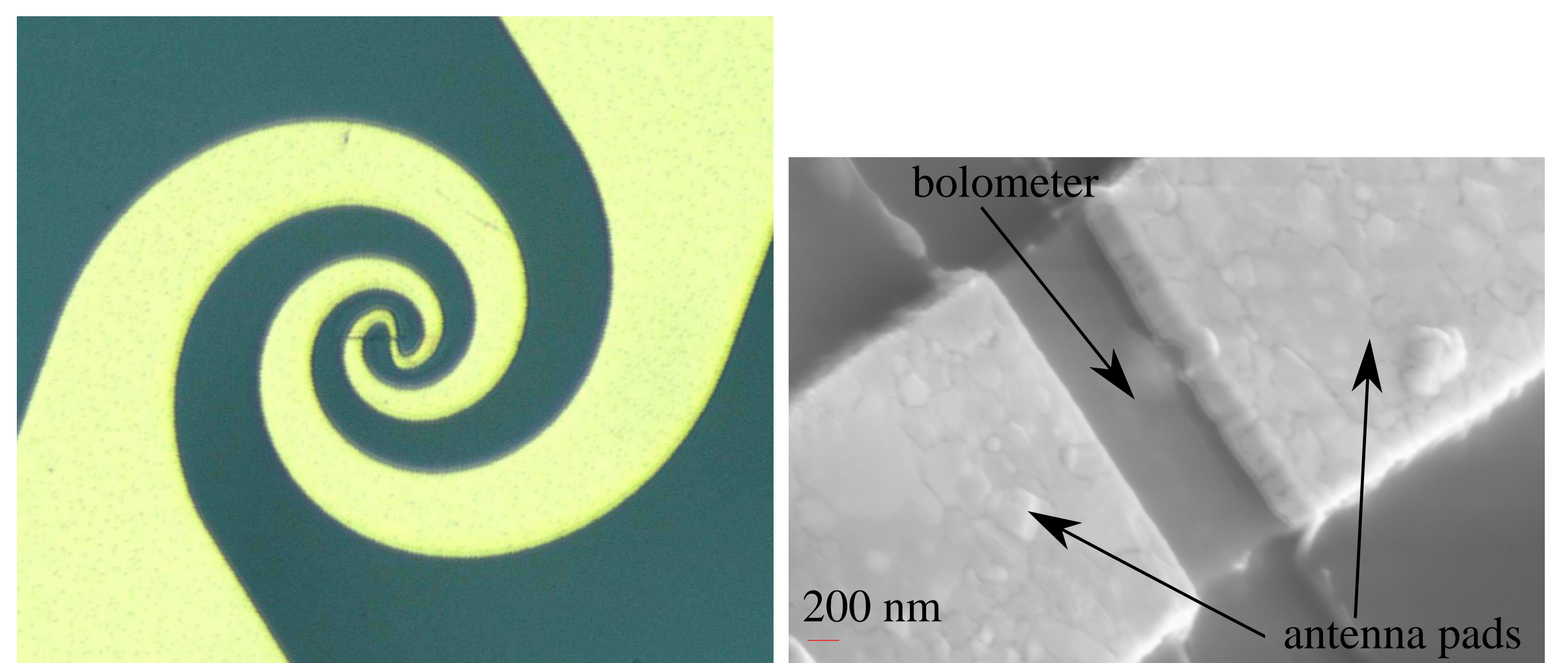


The maximum bias current  $i_{max}$  is given by the criterion  $i_{max}^2 \alpha R = 0.3G$ . The thermal conductance  $G$  is given by the ratio of the bolometer area and the bolometer/substrate thermal resistance:  $G = A/R_{bd}$ .

### Devices

A logarithmic spiral antenna on a silicon lens was used, providing a broad frequency coverage (well above 1 THz).

- Bolometer sizes:  $1.5 \times 1.5$ ,  $1 \times 2$ ,  $1 \times 3$  and  $1 \times 4 \mu\text{m}^2$
- $\text{YBa}_2\text{Cu}_3\text{O}_7$  film thickness: 50 nm
- Critical temperature:  $\sim 86$  K



Pictures showing an optical photograph of a spiral antenna integrated with a  $1 \times 2 \mu\text{m}^2$  bolometer and a SEM photograph showing the bolometer bridge itself.

### Main results

- Optical responsivity of 100 to 500 V/W at cryogenic temperatures, depending on temperature, RF signal frequency and bolometer dimensions. The responsivity can be increased further by using bolometers  $< 1 \mu\text{m}^2$ .
- Responsivity of 15 V/W measured at room temperature. With smaller devices this number should increase substantially; since  $G \propto A$ .
- NEP of 20  $\text{pW}/\text{Hz}^{1/2}$  (readout limited) at cryogenic temperatures for modulation frequencies ranging from 0.5 to 100 kHz.
- NEP at room temperature was measured to be 450  $\text{pW}/\text{Hz}^{1/2}$ .

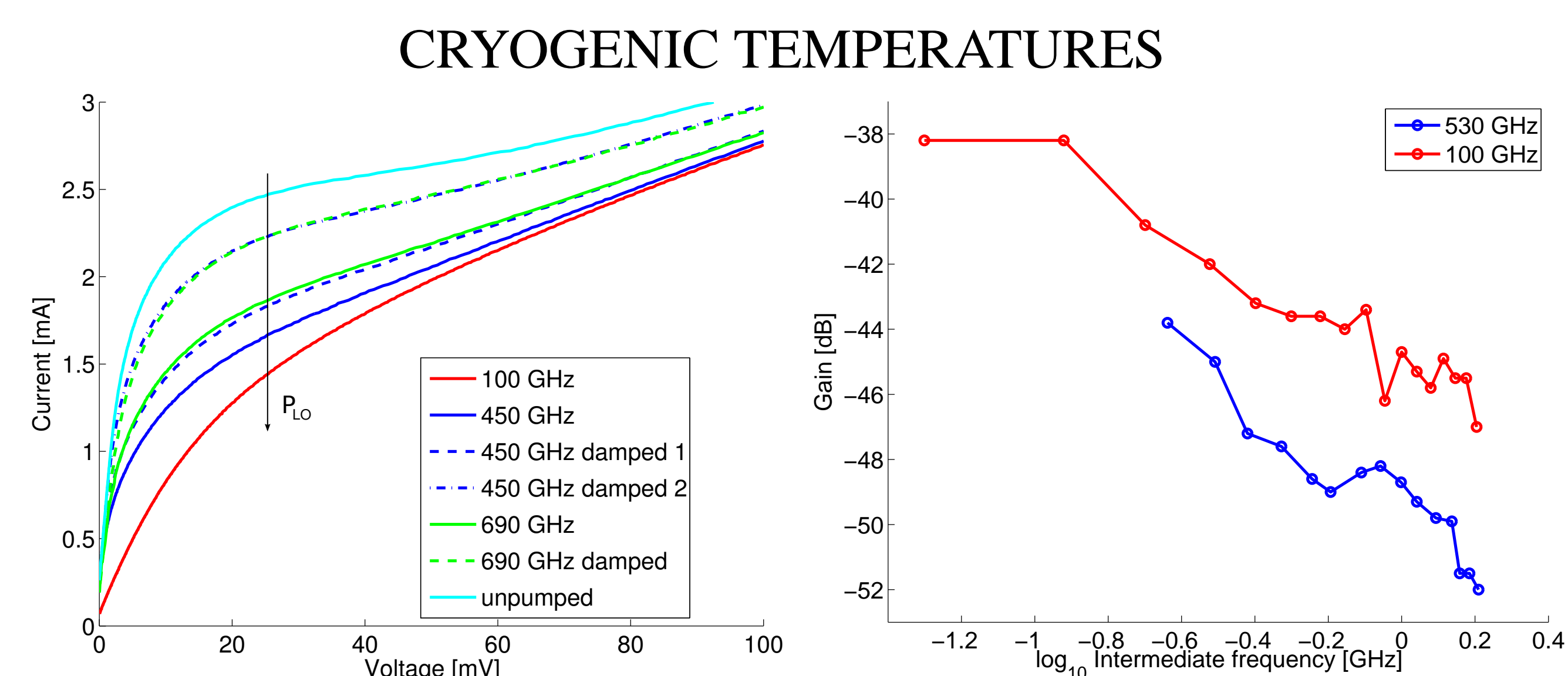
## TERAHERTZ MIXING IN $\text{YBa}_2\text{Cu}_3\text{O}_7$ BOLOMETERS FOR APPLICATIONS AT CRYOGENIC AND ROOM TEMPERATURES

### Introduction

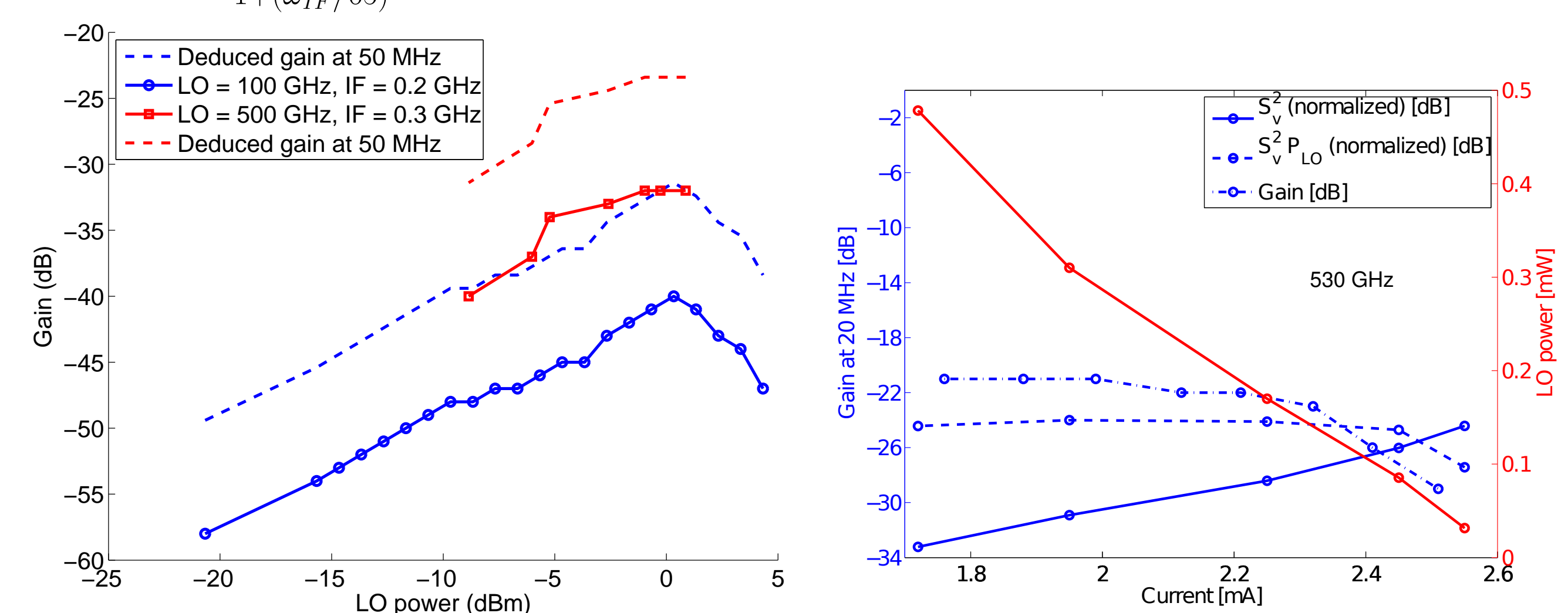
We report on an experimental investigation of high-Tc superconducting bolometric mixers based on thin films of  $\text{YBa}_2\text{Cu}_3\text{O}_7$ . These mixers were tested at LO frequencies of 100 and 530 GHz and for both 77 K and 300 K. For a device with nominal dimensions  $2 \mu\text{m} \times 2 \mu\text{m} \times 50 \text{ nm}$ , a conversion gain of -24 dB was obtained. The output noise was 150 K. The obtained results suggest that the mixers can find various applications in the THz regime. At room temperature, the highest measured mixer gain was -28dB.

### Measurements

- Sources: Gunn oscillators (100 GHz), backward wave oscillators (530 GHz).
- Gain bandwidth measured at both 77 K and 300 K.

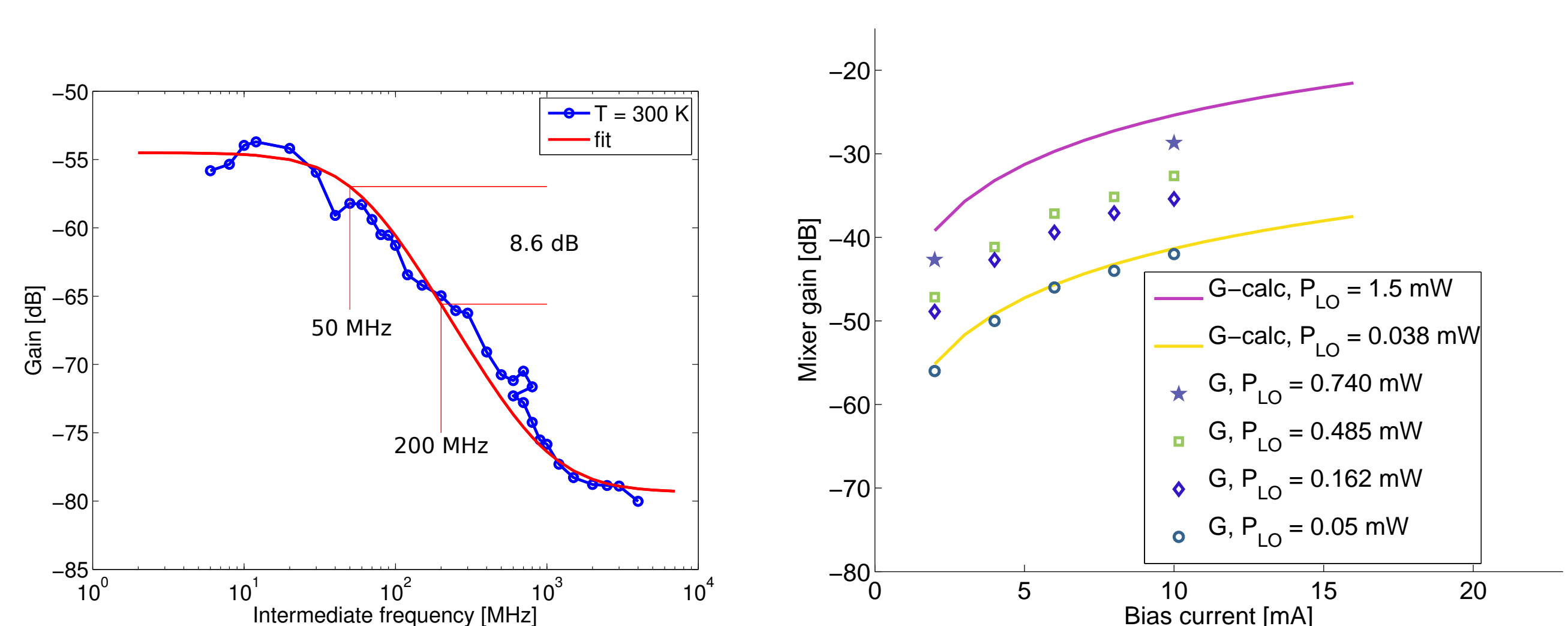


The fit of the conversion gain  $G_0$  at room temperature is given by  $G_0(\omega_{IF}) = \frac{G(0)}{1+(\omega_{IF}/65)^2}$ , where  $\omega_{IF}$  denotes the intermediate frequency [MHz].



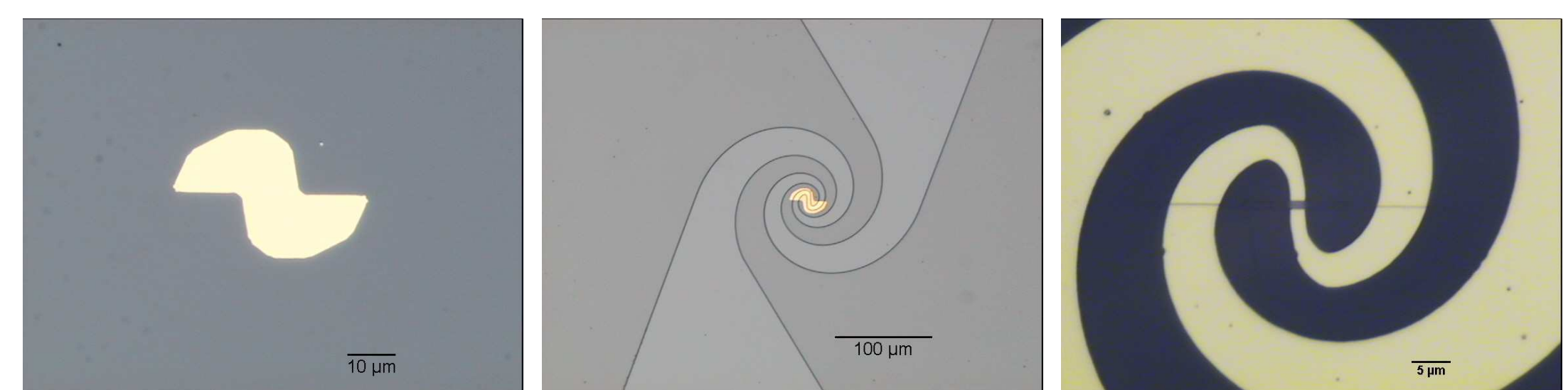
LO power requirements will be lower for smaller devices and better optical coupling. The conversion gain is given by  $G_0 = \frac{2i^2 C_0^2 P_{LO} R_L}{(R_L + R_0)^2} \left(1 - i^2 C_0 \frac{R_L - R_0}{R_L + R_0}\right)^{-2}$ , where  $C_0 = \frac{1}{G} \frac{\partial R}{\partial T}$  ( $S_v = iC_0$ ),  $R_L$  the IF load impedance and  $R_0$  the bolometer dc resistance. The effect of  $i$  and  $P_{LO}$  is similar. Therefore, the lack of the  $P_{LO}$  can be compensated with a higher current.

### ROOM TEMPERATURE



### Device fabrication

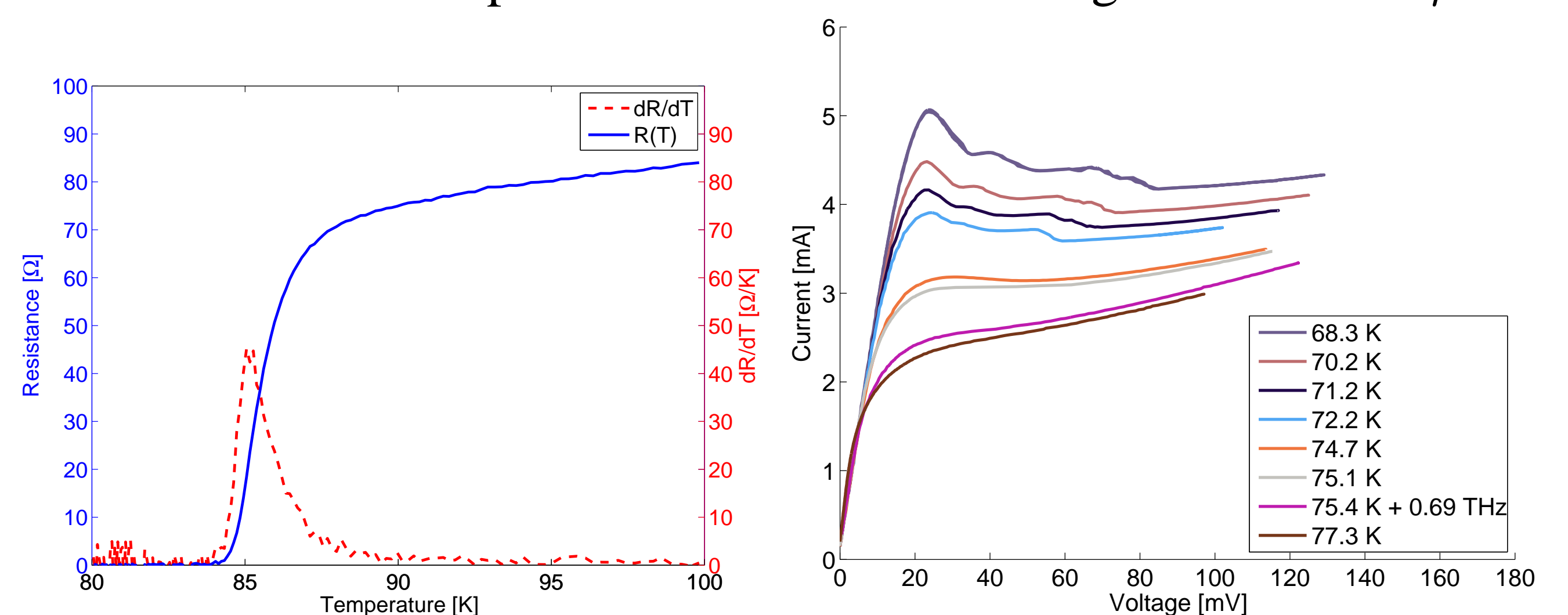
- Laser ablation used to deposit  $\text{YBa}_2\text{Cu}_3\text{O}_7$  films on  $\text{Al}_2\text{O}_3$  with  $\text{CeO}_2$  buffer layer.
- Bolometers patterned using carbon masks and ion milling.
- Spiral antennas defined using UV photolithography.



Optical photographs showing three steps in the fabrication process. The left picture shows a small piece of  $\text{YBa}_2\text{Cu}_3\text{O}_7$ , covered with a protective layer of gold, that forms the bolometer. In the middle the spiral antenna is depicted just after the photolithography step prior to the gold deposition. The right picture shows a finished bolometer integrated with with a spiral antenna.

### DC Characteristics

Resistance versus temperature was measured using a current of  $1 \mu\text{A}$ .



Picture showing the experimental setup for mixing experiments at 100 GHz.

### Main results

- -24 dB conversion gain at 77 K and 530 GHz LO signal.
- -28 dB conversion gain at 300 K.
- Response time of about 2 ns at room temperature and 300 ps at cryogenic temperatures.
- Conversion gain will increase and LO power requirements will scale down for smaller devices.

# Wideband THz detectors based on YBCO thin films at 77K and at room temperature.

S. Cherednichenko, A. Hammar, S. Bevilacqua, V. Drakinskiy, J. Stake.  
Terahertz and Millimetre Wave Laboratory, Chalmers University of Technology,  
SE-412 96 Göteborg, Sweden

**Abstract**-We present results of experimental investigation of THz direct detectors based on ultrathin YBCO films. The detectors are integrated with a spiral planar antenna. In the frequency band of 0.1-1.6THz the optical responsivity is from 170V/W for 77K. It increases to 400 V/W for operation temperature about 76K. The responsivity was constant up to 100kHz. Using mixing technique, the measured time constant is  $\sim 0.5$ -2ns. Currently, at 77K, the NEP is  $\sim 20$ pW/Hz<sup>0.5</sup>. At room temperature, the NEP is about 250pW/Hz<sup>0.5</sup>. For the same devices as coherent detector, the mixer gain was -21dB at 77K (and -28dB) at room temperature for an LO power of 0.4mW. With the present devices a mixer gain of up to -23dB is possible at 300K for an LO power of 1.5mW. Using smaller devices, similar gain can be achieved for a much smaller LO power.

## I. INTRODUCTION

Low  $-T_c$  superconducting bolometers are extensively used both as direct detectors and mixers, where they show performance superior to other types of devices (for mixers at frequencies above 1THz) [1]. On contrast, semiconductor detectors require no cooling and hence are more convenient to use (no limits on the instrument operation time, smaller mass). The state of the art performance for room temperature direct detectors is 0.24 pW/Hz<sup>0.5</sup> at 95GHz for InAs/AlSb/GaSb backward diodes [2] and for zero biased Schottky diodes at 600-900GHz a NEP of about 5 to 20 pW/Hz<sup>0.5</sup> was reported [3]. Despite of extended research on bolometric photo detectors based on thin high- $T_c$  superconducting YBCO films, there is a little information on their performance in the subMM range. Currently, very compact and lightweight cryocoolers to 77K are available, what facilitates the use of this type of detectors. Our goal was to fabricate and measure the responsivity and the noise of antenna integrated YBCO bolometers through the whole subMM range. Such bolometer were tested both for incoherent and coherent detection. Because of a rather large Temperature Coefficient of Resistance (TCR) of YBCO films in the normal state (i.e. at a temperature above 90K) such bolometers, as we discovered, provide also high sensitivity even in the normal state, well up the room temperature. Bolometers voltage responsivity and down conversion gain was measured at the room temperature at 100GHz and 500GHz.

The bolometers were fabricated of 50nm YBCO films made by pulsed laser deposition on r-cut Al<sub>2</sub>O<sub>3</sub> substrates with a thin CeO<sub>2</sub> buffer layer. The bolometer length was about 1 $\mu$ m and the width varied from 1.5 to 4  $\mu$ m. The bolometer was situated at the center of a logarithmic spiral antenna, which covers (based on our earlier findings) a frequency range from 300GHz

to 2.5THz. The detector/antenna chip was mounted on a 12mm elliptical silicon lens (Figure 1). The critical temperature of the bolometers was about 86K and the cooling was arranged in a LN optical cryostat. A heater was used to bring the device to temperatures above 77K and LN vapor pumping was used to reduce the temperature. The bolometer was dc current biased to the resistive state (exceeding the critical current of 2-7mA, depending on the device).

Above 100K the  $dR/dT$  is approximately 0.2-0.4  $\Omega/K$ , for different device sizes. But the TCR is the same for all devices, which at room temperature is approximately 0.008 K<sup>-1</sup>.

The voltage response from the bolometer was directly measured by a lock-in amplifier (at room temperature), with an input noise of 4-5 nV/Hz<sup>0.5</sup>. For the mixer tests, the IF signal was preamplified with an room temperature LNA with a noise temperature  $\sim 100$ K.

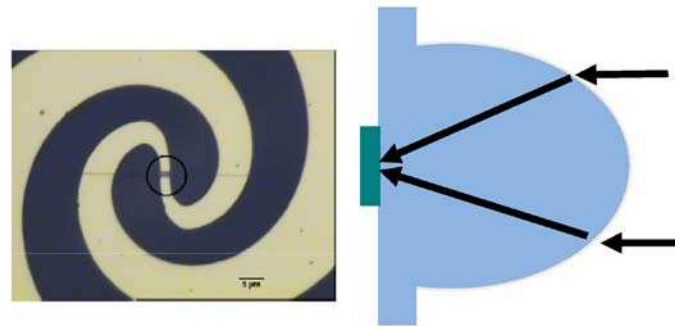


Figure 1. A photograph of a spiral antenna-integrated YBCO microbolometer.. The bolometer is in the circle. (left) The bolometer chip is mounted on an elliptical silicon lens. (right)

The responsivity was measured by the ratio of the output voltage to the input RF power. A W-band Gunn oscillator, a 300-550GHz BWO, and a FIR gas laser were used as the subMM signal sources. The source to the bolometer optical coupling was arranged via a Teflon lens (Figure 2). The power of the signal incident on the cryostat was measured by both the Thomas Keating (optical) and Erickson (waveguide with a horn) power meters. For the responsivity calculations, the incident RF power was calibrated for the cryostat window loss (0.7), and the spiral antenna to the linear polarization coupling loss (0.5). The circular polarization of the antenna was verified at 300GHz by measuring the bolometer response while rotating the bolometer block (at room temperature) around the optical axis. We shall note, that in order to ensure a single spatial

mode of the BWO beam, a WR10-WR3 waveguide transition and a WR3 smooth wall circular horn were connected to the output waveguide (WR10) of the BWO. By doing it, we limited the available RF power, however it makes the power calibration more reliable.

The noise voltage was measured with the same lock-in amplifier once the RF signal was blocked. The output IF noise of the bolometer was measured by comparing the system noise with the bolometer bias on and off. In the superconducting state the bolometer output noise was about 150K.

For the mixer tests at 530GHz two BWOs, one as an LO and the other as a signal source, were coupled via a thin film beam splitter. At the W-band (90GHz) there was more power available from the Gunn oscillator sources. Therefore, two Gunn sources were also used for the mixing tests, or (as in Figure 3), one Gunn oscillator and an active multiplier [4].



Figure 2. Direct detection test at 0.7 and 1.6THz with a FIR laser (left). The detector is in the cryostat on the right.



Figure 3. YBCO mixer test at room temperature. A W-band Gunn oscillator and a W-band active multiplier are coupled using a W-band directional coupler, to be used as a signal and an LO sources

We have found that in the superconducting state the responsivity scales reversely proportional to bolometer area. Such behavior is expected since the bolometer responsivity is

$$S_V = \frac{i \cdot \partial R / \partial T}{G - i^2 \cdot \partial R / \partial T} \quad (1)$$

, where  $G = w \lambda l / R_{bd}$  is the heat conductivity from the bolometer to the substrate, and  $R_{bd}$  is the YBCO/substrate boundary thermal resistance. For the smallest devices,  $1.5 \times 1 \mu\text{m}^2$ , the highest responsivity  $\sim 400 \text{ kV/W}$  is achieved at 76K, while it is about 170 V/W at 77K (see [5] for details). The responsivity

was constant from nearly 100GHz up to 1.6 THz. By applying an amplitude modulated source signal to the active multiplier (90GHz output frequency [4]) we were able to measure the bolometer responsivity up to 100kHz (by the lock-in amplifier) and between 100kHz and 500kHz using a spectrum analyzer. No responsivity drop was observed. Higher responsivity requires higher bolometer electrical resistances, which was still not optimized. The noise was measured at 77K and was readout system limited to  $4\text{-}5 \text{ nV/Hz}^{0.5}$  for frequencies above 500Hz. It results in  $\text{NEP} \sim 20 \text{ pW/Hz}^{0.5}$ .

In Figure 4, we summarize the NEP data for the  $1.5 \times 1 \mu\text{m}^2$  bolometer. Published NEP values for some semiconductor detectors are given also for comparison. Using a lower noise readout the NEP of the present devices can be reduced down to  $2 \text{ pW/Hz}^{0.5}$ . Alternatively, the voltage responsivity of YBCO bolometers can be increased by reducing the bolometer area. In our lab we have an experience of fabricating  $500 \times 100 \text{ nm}$  bolometers, which theoretically shall have about a factor of 30 higher responsivity, hence lower NEP, compared to the devices from Figure 4. We expect that good superconducting properties can be preserved in YBCO bolometers as narrow as 50nm.

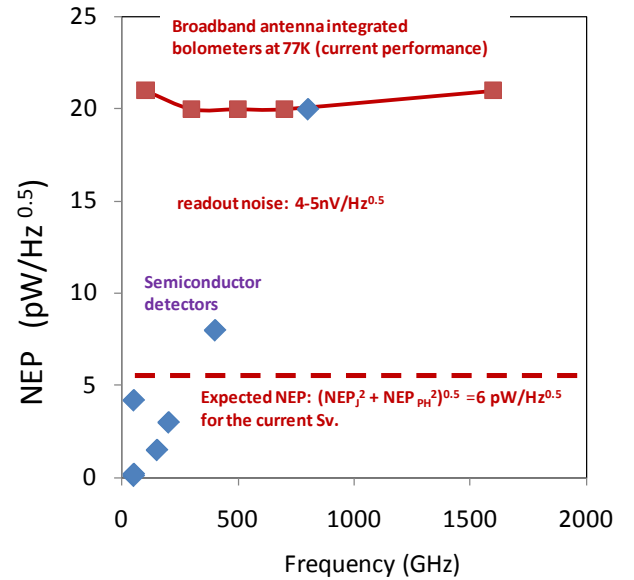


Figure 4. NEP versus signal frequency at 77 K for the  $1.5 \mu\text{m} \times 1.5 \mu\text{m}$  (diamonds) sized bolometers (squares). The dashed line is the bolometer NEP calculated from the Johnson and phonon noise contributions and the currently obtained Sv. Blue diamonds show the current performance of semiconductor detectors (e.g. Schottky diodes [2], [3]).

The conversion gain of the same bolometers was measured at 530GHz and 90GHz. The signal and the LO power was computed using the voltage responsivity, measured in the previous tests and the voltage swing corresponding to the RF (LO) on-off. For a  $3 \mu\text{m} \times 1 \mu\text{m}$  bolometer the maximum measured conversion gain was approximately -21dB for a 0.18mW LO power (530GHz). By reducing the bolometer temperature and simultaneously increasing the LO power, the

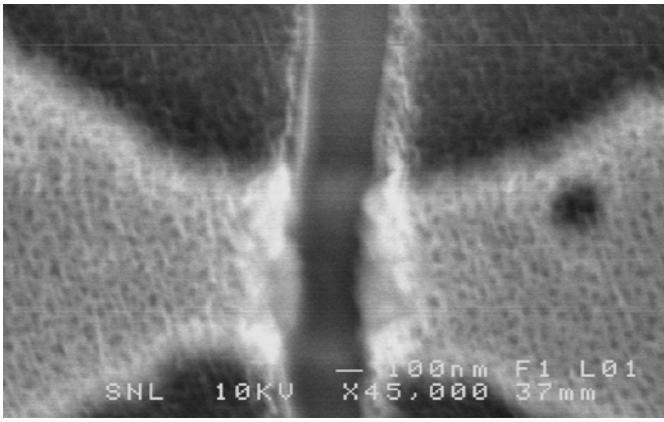


Figure 5. Scanning Electron Microscope image of an 500nm×100nm YBCO bolometer.

mixer gain will increase. If the pumped IV-curve is kept the same (i.e. a reduction of the temperature is compensated by an increase of the LO power), the mixer gain will change linearly with the LO power. Therefore, for a 2mW LO power a mixer gain of -11dB shall be possible to achieve for the discussed device.

It was very interesting to discover that our YBCO microbolometers have quite high sensitivity even in the normal state, in particularly at room temperature. The advantage of the room temperature operation over the superconducting state is the fact that  $\partial R / \partial T$  is temperature independent, and, hence a large bias current can be applied. In the superconducting state,  $\partial R / \partial T$  is determined by the resistive state in the bolometer, caused by the bias current. Therefore, in the superconducting state there is a bias current corresponding to a maximum responsivity. For the currents exceeding this optimum value, the responsivity decreases (see equation 1):

In the normal state, the responsivity is a linear function of the bias current. The limit here is the device breakdown. Our preliminary experimental data show that YBCO bolometers break when the current increases till the second term in the denominator in (1) approaches the first term. For safety reasons, we currently limit the bias current to about  $i_{max} = (0.3 G / \alpha R_I)^{0.5}$ . Experimentally, a responsivity of approximately 15V/W has been achieved at room temperature. The system noise is still readout limited. Therefore, we estimate that at room temperature the NEP is approximately 250pW/Hz<sup>0.5</sup>, for modulation frequencies 500Hz-100kHz.

Results for the mixer gain measurements at room temperature are given in Figure 6. For a bias current of 10mA and a LO power of 0.74mW (90GHz LO frequency), the measured mixer gain is -28dB. A gain of -21dB shall be reached for a bias current of 15mA and an LO power of 1.5mW. For smaller devices the LO power requirements are reduced. Our computations show that for a 500nm x 500nm bolometer a gain of -16dB shall be possible to achieve for a 0.5mW LO power.

In conclusion, at 77K YBCO thin film microbolometers

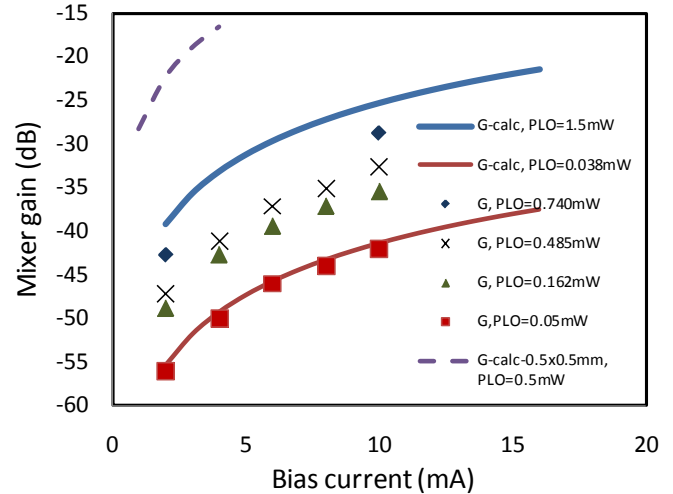


Figure 6. Measured (symbols) and calculated (solid lines) mixer gain for a 3µm×1µm bolometer at room temperature versus bias current. The used LO power is also given. The dashed line is the calculated mixer gain for a 0.5µm×0.5µm bolometer with a 0.5mW LO power.

show avoltage responsivity comparable to Schottky diode detectors for frequencies above 800GHz. The bolometer responsivity is nearly constant across a wide frequency range from 100GHz to 1.6THz, which is set by the antenna bandwidth. With a lower noise readout the bolometer NEP will reduce to about 6pW/Hz<sup>0.5</sup>, which makes it the most sensitive THz detector without LHe cooling. Using smaller bolometers we expect to reduce the NEP by another order of magnitude. The same devices can be used both for incoherent and coherent detection. Intrinsically, there is no frequency limit for such detectors. Simplicity of the presented detectors makes the fabrication of large arrays quite straightforward.

## REFERENCES

- [1] S. Cherednichenko, V. Drakinskiy, T. Berg, P. Khosropanah, and E. Kollberg, *Rev. Sci. Instrum.*, 79, 034501 (2008).
- [2] N. Su, R. Rajavel, P. Deelman, J. N. Schulman, and P. Fay, "Sb-Heterostructure millimeter-wave detectors with reduced capacitance and noise equivalent power" *IEEE Electron Device Lett.*, vol. 23, no. 10, pp. 585–587, Oct. 2002
- [3] L. Liu, J. L. Hesler, H. Xu, *Member*, A.W. Lichtenberger, and R. M. Weikle, "Broadband Quasi-Optical Terahertz Detector Utilizing a Zero Bias Schottky Diode," *IEEE Microwave Wireless Comp. Lett.*, vol. 20, no. 9, pp. 504–506, Sept. 2010
- [4] ALMA VWR LO source, Omnisys Instruments AB, Göteborg, Sweden.
- [5] S. Cherednichenko, A. Hammar, S. Bevilacqua, V. Drakinskiy, J. Stake, "Terahertz direct detection in YBa<sub>2</sub>Cu<sub>3</sub>O<sub>7</sub> microbolometers," submitted to *IEEE Trans. Terahertz Technol.*,